Theoretical description of non-linear process in magnetic materials

Shalu Rani

To cite this version:

Shalu Rani. Theoretical description of non-linear process in magnetic materials. Physics [physics]. Institut Polytechnique de Paris, 2021. English. NNT : 2021IPPAX128 . tel-03662475

HAL Id: tel-03662475
https://theses.hal.science/tel-03662475

Submitted on 9 May 2022

INSTITUT
POLYTECHNIQUE
DE PARIS

NNT : 2021IPPAX128

Thèse de doctorat

Theoretical Description of Non-linear Processes in Magnetic Materials

Thèse de doctorat de l'Institut Polytechnique de Paris
préparée à École Polytechnique

École doctorale n° 626 École Doctorale de l'Institut Polytechnique de Paris
(ED IP Paris)
Spécialité de doctorat : Physique

Thèse présentée et soutenue à Palaiseau, le 16 décembre 2021 par

Shalu Rani

Composition du Jury :

Henri-Jean DROUHIN Professeur École Polytechnique	Président
Elena DEGOLI Professeure associée, University of Modena and Reggio Emilia	Rapporteure
Hans-Christian WEISSKER Chargé de recherche, CNRS	Rapporteur
Fabrice CATOIRE Chargé de recherche, CNRS	Examinateur
Valérie VENIARD Directrice de recherche, CNRS	Directrice de thèse

Résumé

La génération de seconde harmonique (SHG) est un processus au cours duquel deux photons d'énergie sont absorbés par un matériau et un photon d'énergie 2ω est émis. Ce processus est théoriquement décrit par la susceptibilité macroscopique du second ordre $\chi^{(2)}$. Cette spectroscopie est utilisée pour étudier les propriétés optiques des matériaux et elle révèle des informations supplémentaires inaccessibles aux spectroscopies optiques linéaires. En effet, comme les règles de sélection dipolaire interdisent la SHG dans les matériaux centro-symétriques, il est possible d'obtenir une caractérisation structurale et électronique de systèmes complexes, comme les surfaces et les interfaces. De plus, l'absence de symétrie d'inversion du temps, due à un ordre magnétique, fait apparaître de nouvelles contributions dans la génération de seconde harmonique. Dans le cas de matériaux antiferromagnétiques, la symétrie magnétique détermine la polarisation du matériau et la génération de seconde harmonique révèle alors l'arrangement des spins dans le solide. Cette spectroscopie peut ainsi être utilisée pour l'étude de processus ultra-rapides dans les matériaux magnétiques, tels que les phénomènes de démagnétisation en champs forts. Ces dernières années, un formalisme permettant de modéliser les spectres de seconde harmonique pour les semi-conducteurs traditionnels a été développé, mais il existe peu de descriptions théoriques ab initio satisfaisantes pour les processus non-linéaires dans les matériaux magnétiques. Ces approches théoriques doivent être capables de traiter sur le même pied les interactions électron-électron, les effets de champs locaux (reflétant les inhomogénéités microscopiques dans le matériau) et la distribution en spin des électrons.

Le but de ma thèse était de calculer numériquement les réponses optiques, linéaires et du second ordre, pour des matériaux antiferromagnétiques. J'ai calcule ces deux reponses pour un oxyde de chrome (Cr_2O_3) dans le cadre d'un formalisme ab-initio, reposant sur la TDDFT (Théorie de la Fonctionnelle de la Densité Dépendante du Temps). Dans cette approche, la distribution en spin a été prise en compte explicitement et cette extension a été implémentée dans le code 2light développé au laboratoire.

L'interaction électron-électron est décrite mathématiquement par le noyau d'échange et de corrélation fxc. Ce noyau n'est pas connu exactement et nous devons en trouver des approximations. Trouver une bonne approximation pour fxc est extrêmement important car la modélisation et l'interprétation des expériences repose fondamentalement sur ces approximations. En particulier, fxc doit être en mesure de décrire les effets excitoniques (interactions électron-trou) dans la réponse optique. Différentes approximations sont disponibles dans la littérature et j'ai étudié l'influence de ces noyaux approximés sur les propriétés optiques de Cr_2O_3. J'ai également calculé les spectres de seconde harmonique avec ces noy-

aux. Dans le cas des spectres d'absorption, j'ai comparé mes résultats aux spectres calculés à partir de l'équation de Bethe-Salpeter qui prend en compte explicitement les effets excitoniques et j'ai pu ainsi mettre en évidence la présence d'un exciton fortement lié. A partir de l'équation de Bethe-Salpeter et en comparant aux résultats obtenus en TDDFT, j'ai pu définir un noyau d'échange-corrélation dynamique, modélisant l'exciton lié. Ce noyau a ensuite été utilisé pour le calcul de la génération de seconde harmonique. J'ai ainsi pu observer la signature de l'exciton lié dans les processus non-linéaires.

L'oxyde de chrome Cr_2O_3 existe sous trois formes ayant une structure antiferromagnétique. Je me suis finalement intéressée à ces différentes structures possibles, ne différant entre elles que par la distribution des spins. J'ai montré que mes résultats permettaient de discriminer de façon caractéristique entre ces structures. En particulier, les spectres de seconde harmonique sont très caractéristiques car une des structures conserve la centro-symmétrie, malgré son caractère antiferromagnétique.

Acknowledgement

First and foremost, I would like to extend my deepest gratitude to my supervisor, Valérie Veniard, for her unsurpassed support, patience, expertise, and kindness without which this thesis would have not been possible. Through her constant guidance, I have gained a better understanding of the subject. Thanks to her, I have been able to develop my own research skills since she gave me sufficient working autonomy. Thanks to her for helping me adjust to a new culture and for helping me with other things besides research.

Furthermore, I would like to thank the jury members Elena Degoli and Hans-Christian Weissker for reviewing the thesis work; Henri Jean Drouhin, and Fabrice Catoire for evaluating the thesis work. It is an honor and a pleasure to have them all on this jury.

I am grateful for all the help and support I have received from my colleagues - Lucia Reining, Matteo Gatti, Christine Giorgetti, Andrea Cucca and Francesco Sottile. I will be indebted to you all for the knowledge we exchanged and the fruitful discussions we had. I would also like to thank Ayoub Aouina, Georg Michelitsch, Abdallah El Sahili, Alam Osorio, Stefano Mazzei, Jack Wetherell, Vitaly Gorelov, Rajarshi Sinha Roy, Laura Urquiza, Lionel Lacombe, Arnaud Lorin, Ilya Iagupov, Jaakko Koskelo, and Paula Kleij. Due to their friendships, encouragement and lively discussions, work became fun too. I thank you all for creating a warm and welcoming atmosphere. For always being happy to lend a hand when I needed it. I will always miss the parties we had the last three years.

Also, I would like to thank all the institutions that have supported me along the way, including École polytechnique and Laboratoire des Solides Irradiés and European Theoretical Spectroscopy Facility (ETSF) for providing me with this opportunity. In addition, I would like to thank CEA Numerics International PhD program for providing me with funding to work in France, and for hosting me there.

In my humble opinion, this journey would not have been possible without my friends over the years. We spent a lot of time together Yogendra Singh, Pragya Vishwakarma, Surbhi Jagtap, and I am grateful for everyone's constant presence, attention, and fun. Thank you so much. My gratitude goes out to Ankush Bhatia, Shubham Biswas, Sonali Khurana , Arunima Thakral for all the delightful time we spent together, especially during the thesis writing phase. Thanks a lot, Bhrigu Mahajan, Amrut Battuwar, Anand Kumar, Amit Kumar, Abir Ezzedine ,Valeria, Pranjal Nandi, Shipra Sethi for being a part of this journey. Also, I would like to thank Ankit Tomar , Sachin Kaushik , Surishi Vashishth , Rohit Attri, Vinita Ahuja, Sharon Horta, Omeshwari Bisen , Tusharadri Mohapatra , Rahul Yadav, Kunal Kosarkar, Rajendra Singh, Manish Negi, Pushpendra Gupta, Himanshi

Dua and Deepa Sharma, for always being there for me no matter how far away we were. I would also like to express my gratitude towards Lochan Kumar for his support.

Last but not least, I would like to thank my family, whose support and effort are indescribable.

Contents

List of Figures

List of Tables

Chapter 1

Introduction

Second harmonic generation (SHG) is a non-linear process in which two photons, of energy ω are absorbed by a material, and a photon of energy 2ω is emitted. This process is theoretically described by the second-order macroscopic susceptibility $\chi^{(2)}$. This spectroscopy is used to study the optical properties of materials, and it reveals additional information which cannot be accessed with linear optical spectroscopies. Indeed, as the dipolar selection rules prohibit SHG in centrosymmetric materials, it is possible to obtain complex a structural and electronic characterization of complex system. In particular, due to a magnetic order, the absence of time inversion symmetry reveals new contributions in second harmonic generation. For the specific case of antiferromagnetic materials, magnetic symmetry determines the polarization of the material and SHG then reveals the arrangement of spins in the solid. It was shown to be used to study ultrafast processes in magnetic materials, such as demagnetization [1].

The motivation of the project is the results shown by S. Wall et al. article entitled "Resonant optical control of the structural distortions that drive ultrafast demagnetization in Cr_2O_3" [1]. Cr_2O_3 is a centrosymmetric material with the crystallographic point group $\bar{3}$m. Below the Neel temperature (308K), Cr ions order antiferromagnetically (AFM) along the trigonal z-axis and enable the SHG to occur as shown in figure (1.1). Therefore, S. Wall et al. used second-harmonic generation (SHG) to probe the demagnetization process in the AFM Cr_2O_3. In a pump-probe experiment, S. Wall et al. show that the color of the wavelength of the pump can be used to control the demagnetization process of the antiferromagnetic insulator Cr_2O_3. The second harmonic produced by the probe was used to follow in time the change in the magnetic and structural state of the material. Time-resolved SHG signals for three different pump photon energies are measured as shown in figure (**??**). A strong decrease in the SHG signal is measured at a short delay, which depends on the pump photon energy. After 1ps, the change in the signal for all energy becomes very slow, as shown in figure (1.1).

After studying this fast dynamic in detail, they concluded that it is possible to control the demagnetization rate by 25% in AFM Cr_2O_3 by changing the photon energy used to excite the system.

This project aims to provide accurate calculations of the second-order response for antiferromagnetic materials. It is based on time-dependent density functional theory (TDDFT), in a spin-dependent framework, including accurate exchange

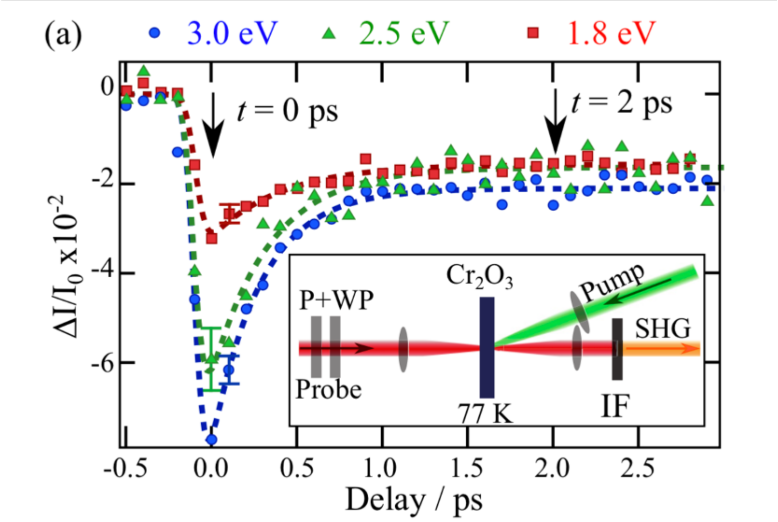

Figure 1.1: SHG signal at three different pump photon energy

correlations kernels.

In the first part of the thesis, the various theoretical approaches have been described and the same have been used to calculate the properties of Cr_2O_3. In the latter part, the results and development are discussed.

It is necessary to first examine the ground state properties of the system before proceeding to the study of the second-order response function.

In chapter (7), the ground state properties using the density functional theory (DFT) are studied.

The bandstructure and direct band gap of Cr_2O_3 in the density functional theory framework is studied. The impact of incorporating spin-polarization at the ground state level on the properties of Cr_2O_3 is investigated. Additionally, the effect of various pseudopotentials on the DFT band gap of Cr_2O_3 is studied. The band gap determined by DFT is not the correct band gap, and therefore, the band gap estimated using the GW method is examined as well. Also the influence of semicore electrons pseudopotential on the GW band gap is addressed. Finally, the estimated band gap of Cr_2O_3 with previously reported theoretical and experimental band gaps are compared. The band gap computed using the GW method incorporating semicore electrons agrees with the previously reported band gap.

In the chapter (8), the linear response of the Cr_2O_3 is calculated using the time-dependent density functional theory and the many body perturbation theory. In this chapter, first, the linear response calculated using different approximations in TDDFT for Cr_2O_3 is discussed. The local field and excitonic effect in the TDDFT on Cr_2O_3 linear spectra is discussed. The local field effect is incorporated in TDDFT through RPA approximation. The impact of incorporating spin-polarization in the linear response function for Cr_2O_3 is investigated. The excitonic effect is incorporated in the TDDFT through the exchange-correlation kernel. Various approximations of the exchange-correlation kernel exist, which is discussed in the chapter (8). The impact of different xc kernels on Cr_2O_3 is studied. An alternative to the TDDFT for calculating absorption spectra is the Bethe

Salpeter Equation (BSE) approach, which is discussed later in this chapter. The BSE spectrum was compared to previously computed spectra using TDDFT. This comparison helps to determine the accuracy of different xc kernels of TDDFT for the Cr_2O_3 spectrum, which is useful for the further calculation of second-order response using TDDFT. Additionally, the BSE spectra show the bound excitonic peak, not seen in the TDDFT spectrum. Additionally, the binding energy of the exciton is very high when calculated using the BSE spectrum, indicating that the exciton is a bound exciton.

In the chapter (9), the Wannier model is studied, that is used to compute the excitonic binding energy of a material. In comparison to the BSE computations, this model is simpler and less time-consuming.

The alternative goal of this thesis is to calculate the second-order response function, which describes the second harmonic generation, and it is discussed in the chapter (10). The second-order response function equation, which includes spin-polarization, has been discussed in detail in the chapter (10) for the first time. Further, the second-order spectra for Cr_2O_3 in the TDDFT framework are analyzed. As for the linear response, the local field and excitonic effect, in the second-order response, in TDDFT framework, is discussed. We also discussed similar effect for the second-order response function.

First, the influence of local fields on second-order spectra is examined. Later, the excitonic influence on the spectra through the exchange-correlation kernel is explored. The accuracy of the spectra computed using the TDDFT method relies on the xc kernel's accuracy.

Since the first order xc kernel is the same in both the linear and second-order cases, the BSE result for the linear spectra can be used to get the first order xc kernel, which is significant in second-order spectra. The results obtained with this kernel is compared to the spectra obtained with a previously computed kernel.

Further, all these properties for the different AFM structures of the Cr_2O_3 is discussed in the chapter (11). Starting from ground state theory to the second-order, all the properties for the different spin structures of Cr_2O_3 are compared.

It has been described that changing the spin structure has a remarkable effect on the properties of materials.

Later on, it has been discussed in detail in the chapter (12) that the effect of using different pseudopotentials have different impacts on all three structures of AFM Cr_2O_3.

Finally, the conclusion of the thesis work and future perspective is discussed in the chapter (13).

Part I

Background

Chapter 2

Linear and Non-linear optical properties of solids

In this chapter, we will first define the phenomena, and the coefficients that are used to quantify them. Solid-state materials exhibit a large range of optical properties which can be subdivided into a small number of fundamental phenomena. In figure (2.1), we show the basic set of phenomena: reflection, propagation, and transmission.

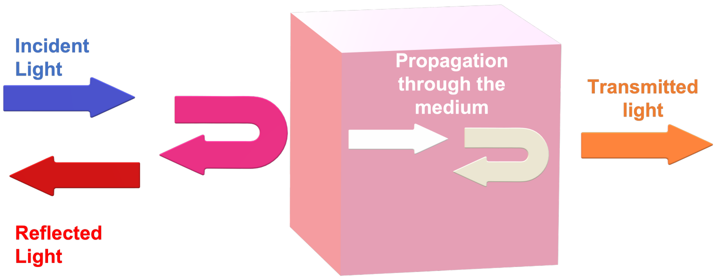

Figure 2.1: Reflection, propagation, and transmission of a light beam incident on an optical medium

The figure (2.1) shows a light beam incident on an optical medium. Some light is reflected from the front surface, while the rest enters the medium and propagates through it. If any of this light reaches the back surface, it can be reflected again or transmitted to the other side. Therefore, the amount of light transmitted is related to the reflectivity at the front and back surfaces and the way the light propagates through the medium.

The phenomena that can occur while light propagates through an optical medium is illustrated schematically in figure (2.2).

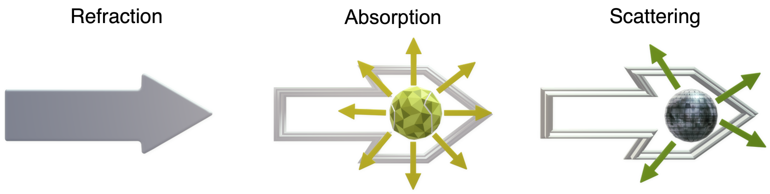

Figure 2.2: Phenomena that can occur as a light beam propagates through an optical medium

Refraction results in a decrease in the wave's velocity, while absorption results in attenuation. Scattering causes the light to be redirected. Absorption, amongst other phenomena is a topic of interest in this thesis.

When the light propagating through the medium has a low intensity, the only linear phenomena occurs; in contrast, if the beam's intensity is high, the non-linear phenomena occurs.

This chapter provides an overview of the linear and non-linear properties of solids.

2.1 Linear optical properties

From a macroscopic perspective, optical absorption, reflection, and light scattering are the measurable quantities that determine the linear optical properties of the system.

2.1.1 Absorption

If the frequency of the light is resonant with the transition frequencies of the atoms in the medium, absorption occurs during propagation. This will result in attenuation of the beam as it travels. Only the light that has not been absorbed by the medium will be transmitted.

Absorption coefficient

The optical phenomena may be characterized using a number of parameters that define the macroscopic properties of the medium.

The absorption of light by an optical medium is quantified by its absorption coefficient α. The fraction of the power absorbed in a unit length of the medium is defined as the α. If the beam is propagating in the z direction, and the intensity (optical power per unit area) at position z is $I(z)$, then the decrease of the intensity in an incremental slice of thickness dz is given by,

$$dI = -\alpha dz \times I(z) \tag{2.1}$$

This can be integrated to obtain Beer's law (assuming $\frac{\partial \alpha}{\partial z} = 0$)

$$I(z) = I_0 e^{-\alpha z} \tag{2.2}$$

where, I_0 is the optical intensity at z = 0. The absorption coefficient of optical materials depends strongly on their frequency, so they may absorb one color but not another.

2.1.2 The complex refractive index and dielectric constant

The complex refractive index is a single quantity that describes the absorption and refraction properties of a medium. This is often denoted as $\tilde{n}$ and is defined through the equation,

$$\tilde{n} = n + \mathrm{i}\kappa \tag{2.3}$$

The real part of $\tilde{n}$, namely n, is the refractive index and the imaginary part of $\tilde{n}$, namely κ, is called the extinction coefficient. As we have shown in the appendix (A), the absorption coefficient α of the medium is related to κ by,

$$\alpha = \frac{2\omega\kappa}{c} \tag{2.4}$$

The complex refractive index ($\tilde{n}$) is related to the complex dielectric constant(ϵ) as,

$$\tilde{n} = \sqrt{\epsilon} = n + \iota k \tag{2.5}$$

Where the real and the imaginary part of $\tilde{n}$ are the refraction index n and the extinction coefficient k are related to the real part ϵ_1 and the imaginary part ϵ_2 of the complex dielectric constant as (detail derivation is shown in the appendix (A).

$$\epsilon_1 = n^2 - \kappa^2 \tag{2.6}$$

$$\epsilon_2 = 2n\kappa \tag{2.7}$$

so that,

$$n = \frac{1}{\sqrt{2}}\Big(\epsilon_1 + \big(\epsilon_1^2 + \epsilon_2^2\big)^{1/2}\Big)^{1/2} \tag{2.8}$$

$$\kappa = \frac{1}{\sqrt{2}}\Big(-\epsilon_1 + \big(\epsilon_1^2 + \epsilon_2^2\big)^{1/2}\Big)^{1/2} \tag{2.9}$$

It demonstrates the link between the real and imaginary parts of ϵ and $\tilde{n}$. Note that if the medium is only weakly absorbing, then it can be assumed that κ is very small, so that equations (2.6) and (2.7) simplify to,

$$\begin{aligned} n &= \sqrt{\epsilon_1} \\ \kappa &= \tfrac{\epsilon_2}{2n}. \end{aligned} \tag{2.10}$$

and hence, the absorption coefficient(α) can be written as,

$$\alpha = \frac{2\omega\kappa}{c} = \frac{\omega\epsilon_2}{nc} \tag{2.11}$$

which is related to the imaginary part of the dielectric constant.

It can be seen from these equations that the refractive index depends mainly on the real component of the dielectric constant and that the absorption depends primarily on the imaginary component. As a result, if the medium has a very high absorption coefficient, this generalization becomes invalid.

2.2 Nonlinear optical properties

In linear optics, the refractive index, absorption coefficient, and reflectivity are considered to be independent of the optical power. This approximation holds true only for low power level. Using a high-power laser, it is possible to explore a new domain of behavior known as nonlinear optics.

Nonlinear optics is a new field of study that has gained prominence as laser applications have become more popular. The polarization P, is a nonlinear function of E. In the linear case, however, P takes a simple linearized form [2],

$$\mathrm{P}(\mathbf{r},t)=\int_{-\infty}^{\infty}\chi^{(1)}(\mathbf{r}-\mathbf{r}',t-t')\cdot E(\mathbf{r}',t')d\mathbf{r}'dt' \tag{2.12}$$

where $\chi^{(1)}$ is the linear susceptibility. The Fourier transformation of (2.12) yields the familiar relation,

$$\mathrm{P}(\mathbf{k},\omega)=\chi^{(1)}(\mathbf{k},\omega)\cdot E(\mathbf{k},\omega) \tag{2.13}$$

with,

$$\chi^{(1)}(\mathbf{k},\omega)=\int_{-\infty}^{\infty}\chi^{(1)}(\mathbf{r},t)\exp(-i\mathbf{k}\cdot\mathbf{r}+i\omega t)d\mathbf{r}dt \tag{2.14}$$

The linear dielectric constant $\varepsilon(\mathbf{k},\omega)$ is related to $\chi^{(1)}(\mathbf{k},\omega)$ by,

$$\varepsilon(\mathbf{k},\omega)=1+4\pi\chi^{(1)}(\mathbf{k},\omega) \tag{2.15}$$

In the nonlinear case, when E is sufficiently weak, the polarization P, as a function of E can be expanded into a power series of E [2] as,

$$\mathrm{P}(\mathbf{r},t)=\mathrm{P}^{(1)}(\mathbf{r},t)+\mathrm{P}^{(2)}(\mathbf{r},t)+\mathrm{P}^{(3)}(\mathbf{r},t)+\cdots \tag{2.16}$$

As in the linear case, the Fourier transform of 2.16 gives

$$\mathrm{P}(\mathbf{k},\omega)=\mathrm{P}^{(1)}(\mathbf{k},\omega)+\mathrm{P}^{(2)}(\mathbf{k},\omega)+\mathrm{P}^{(3)}(\mathbf{k},\omega)+\cdots \tag{2.17}$$

with

$$\mathrm{P}^{(1)}(\mathbf{k},\omega)=\chi^{(1)}(\mathbf{k},\omega)\cdot E(\mathbf{k},\omega) \tag{2.18}$$

$$\mathrm{P}^{(2)}(\mathbf{k},\omega)=\chi^{(2)}(\mathbf{k}=\mathbf{k}_i+\mathbf{k}_j,\omega=\omega_i+\omega_j)\cdot E(\mathbf{k}_i,\omega_i)E(\mathbf{k}_j,\omega_j) \tag{2.19}$$

$$\mathrm{P}^{(3)}(\mathbf{k},\omega)=\chi^{(3)}(\mathbf{k}=\mathbf{k}_i+\mathbf{k}_j+\mathbf{k}_l,\omega=\omega_i+\omega_j+\omega_l)\cdot E(\mathbf{k}_i,\omega_i)E(\mathbf{k}_j,\omega_j)E(\mathbf{k}_l,\omega_l) \tag{2.20}$$

2.2.1 Nonlinear optical susceptibility tensor

The nonlinear susceptibilities of various orders result in a variety of nonlinear phenomena. The majority of these phenomena can be attributed to either the $\chi^{(2)}$ or $\chi^{(3)}$ terms in the polarization and are referred to as second-order or third-order nonlinear effects, respectively.

Due to the well-defined axes of crystalline materials, it is vital to consider that the medium's nonlinear response may be direction dependent.

For example, two optical fields in different directions could be applied and then a nonlinear polarization along a third direction can be generated. The components of the second-order nonlinear polarization $\mathrm{P}^{(2)}$ can be written in the following form,

$$\mathrm{P}_i^{(2)} = \sum_{j,k} \chi_{ijk}^{(2)} E_j E_k \tag{2.21}$$

The quantity $\chi_{ijk}^{(2)}$ that appears in equation (2.21) is the second-order nonlinear susceptibility tensor, and the subscripts i, j, and k correspond to the coordinate axis x, y, and z. Whenever feasible, it is typically more practical to define these axes such that they coincide with the crystal's principal axes. Equation (2.21) shows that there are 27 susceptibilities.

All these components are not independent, and the number of non-zero and independent components depend on the degree of symmetry present in the crystal.

2.2.2 Second-order nonlinear effect

The nonlinear second-order polarization described in equation (2.19) contains a range of nonlinear second order effects.

These are classified into two categories based on their frequency, *a*), one in which both the input frequencies are equal ($\omega_i = \omega_j = \omega$) and *b*), the other in which two input frequencies are not equal ($\omega_i = \omega_1, \omega_j = \omega_2$).

The effects that occur when two input frequencies are not identical, and they are as follows:

1. **Sum-frequency generation(SFG)** Sum-frequency generation (SFG) governed by the nonlinear susceptibilities $\chi_{SFG}^{(2)} = \chi^{(2)}(\omega_{SF}; \omega_1, \omega_2)$ where $\omega_{SF} = \omega_1 + \omega_2$. The Feynman diagram to represent the SFG is shown in the figure (2.3a).

2. **Difference-frequency generation(DFG)** Difference-frequency generation (DFG) governed by the nonlinear susceptibilities $\chi_{DFG}^{(2)} = \chi^{(2)}(\omega_{DF}; \omega_1, \omega_2)$ where $\omega_{DF} = \omega_1 - \omega_2$. The Feynman diagram to represent the DFG is shown in the figure (2.3b).

The effects that occur when two input frequencies are identical, and they are as follows:

1. **Second harmonic generation** is a particular case of frequency doubling when the two input frequencies are equal and sum up. The associated nonlinear susceptibility is $\chi_{SHG}^{(2)} = \chi^{(2)}(2\omega; \omega, \omega)$.

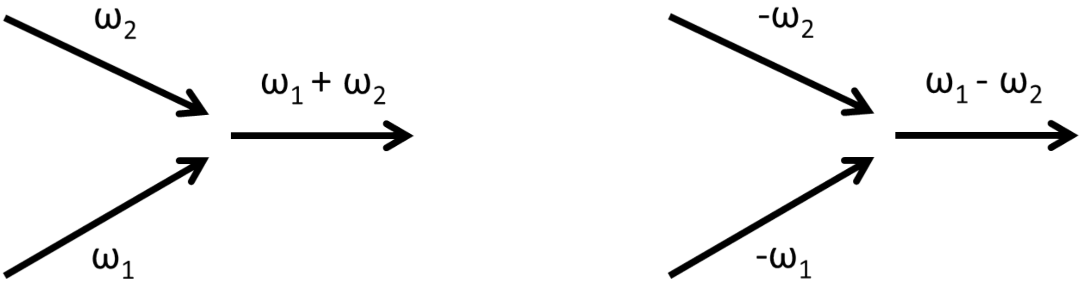

(a) Sum frequency generation (SFG)

(b) Difference frequency generation (DFG)

Figure 2.3: Feynman diagram representing SFG and DFG

2. **Optical rectification** is a particular case of difference-frequency generation when the two input frequencies are identical. The result is a static field corresponding to $\omega = 0$.

2.2.3 Second harmonic generation

Amongst all the nonlinear phenomena existing in nature, a significant role is played by the second-order process *i.e.* second harmonic generation (SHG). When a light of frequency ω is incident on the nonlinear optical medium, then it could emit light at frequency 2ω, schematically represented in figure (2.4).

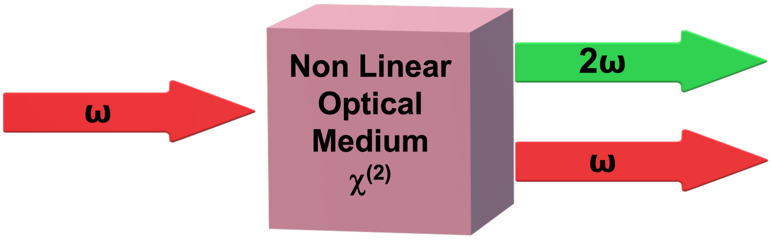

Figure 2.4: Second harmonic generation

In SHG, two photons of frequency ω are absorbed by the material, and due to energy conservation, a photon of frequency 2ω is emitted. This process was first evidenced by P. A. Franken et al. at the University of Michigan, Ann Arbor, in 1961 [3].

The invention of the laser, which produced the requisite monochromatic light at a high intensity made the experiment possible. SHG is possible only in a medium without inversion symmetry.

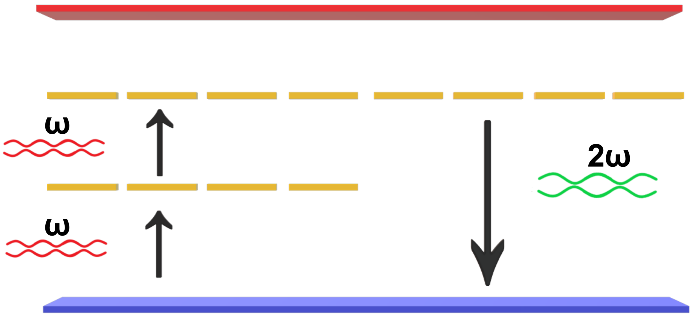

Figure 2.5: Energy level diagram of SHG

Application of SHG

SHG has a wide range of applications in various scientific fields, including physics, chemistry, and biology. Several of them are listed below.

- The generation of new frequencies using fixed-wavelength lasers is one of the most significant applications of the SHG.
- Due to its high sensitivity to the symmetries of the system, it is extremely useful for studying surfaces [4,5], superlattices [6,7] and interfaces [8,9].
- Nowadays, this technique is also used for characterizing systems such as interfaces of nanocrystals [10] or as a probe for molecular chirality in polymers [11,12] and nanotubes [13].
- Furthermore, SHG is also interesting for developing optoelectronic devices. Many experimental efforts are made toward the design, fabrication, and search for new nonlinear optical materials, and SHG techniques play a central role in these studies [14].

2.3 Summary

In this chapter, the linear and nonlinear macroscopic properties were discussed. Also, the second harmonic generation and its applications within the nonlinear properties were discussed.The second harmonic generation and its applications within the nonlinear properties were discussed.

Chapter 3

Density Functional Theory

3.1 Many body approach

To determine theoretically the characteristics of solids, it is essential to solve the many body Schrödinger equation. The ground-state properties can be calculated by solving the time-independent Schrodinger equation, which will be discussed in this section.

Atomic units are employed here and throughout this thesis (unless otherwise specified): the length unit is the Bohr radius $a_0(= 0.5292)$ units, the charge unit is the charge of the electron, e, and the mass unit is the mass of the electron, m_e.

The Schrödinger equation can be written as,

$$\hat{H}\Psi = E\Psi \tag{3.1}$$

where, E is the electronic energy, $\Psi = \Psi(\mathbf{x}_1, \mathbf{x}_2, \ldots, \mathbf{x}_n)$ is the wave function, The coordinates $\mathbf{x}_i$ of electron i contain space coordinates r_i and spin coordinates s_i and $\hat{H}$ is the Hamiltonian operator, which can be written as,

$$\hat{H} = \hat{T} + \hat{V}_{ne} + \hat{V}_{ee} \tag{3.2}$$

where,

$$\hat{T} = \sum_{i=1}^{N}\left(-\frac{1}{2}\nabla_i^2\right) \tag{3.3}$$

is the kinetic energy operator,

$$\hat{V}_{ne} = \sum_{i=1}^{N} V_{ext}(r_i) \tag{3.4}$$

is the electron-nucleus attraction energy operator, in which,

$$V_{ext}(r_i) = -\sum_{\alpha}\frac{Z_\alpha}{r_{i\alpha}} \tag{3.5}$$

is the external potential acting on electron i due to the potential of nuclei of charges Z_α

$$\hat{V}_{ee} = \sum_{i<j}^{N} \frac{1}{r_{ij}} \tag{3.6}$$

is the electron-electron repulsion energy operator.

We may write (3.2) as,

$$\hat{H} = \sum_{i=1}^{N} \left(-\frac{1}{2} \nabla_i^2 \right) + \sum_{i=1}^{N} V_{ext}(r_i) + \sum_{i<j}^{N} \frac{1}{r_{ij}} \tag{3.7}$$

It is known that the electron-electron interaction mediated by the Coulomb potential (3.6) is important for the properties of a solid or a molecule. However, including the electron-electron interaction into the many body problem in a systematic and correct way is a difficult task. The issue was addressed using the Hartree Fock (HF) method [15]. Accounting for the electron-electron interaction using the HF method is computationally challenging. The formulation of many body problem in terms of densities and density matrices opens the way for a new approach of electron systems. As a consequence, determining the density becomes a critical task. The next section (3.2) illustrates the concept of density functional theory (DFT). In DFT, the density of an interacting system of electrons is used to characterize the system rather than the many body wave function of the system.

3.2 Density functional theory

Density functional theory (DFT) represents arguably the most popular and successful method for calculating properties of solid-state materials relevant to technology from first principles. The birth of density functional theory is the work of Hohenberg and Kohn [16] which will be discussed in this section (3.2.1). Within the Kohn-Sham (KS) framework discussed in the section (3.2.3)), the many body problem of interacting electrons is replaced by a system of non-interacting fermions moving in an effective mean-field potential (with the condition that the non-interacting system reproduces the electron density of the interacting one) and it became practically possible to solve the many body problem.

3.2.1 Hohenberg and Kohn theorems

The Hohenberg-Kohn (HK) theorems [16] are the starting point for any discussion of DFT. Rather than refining an approximate theory like the Thomas-Fermi-Dirac one, Hohenberg and Kohn followed the objective of formally defining the DFT as an accurate theory of many body systems, at least for the ground state description.

First H-K theorem H-K first theorem states that any observable is a unique functional of the ground state density n(r) [16].

There is a one-to-one correspondence between the external potential V_{ext} in the Hamiltonian, the (nondegenerate) ground state $|\Psi_0\rangle$ resulting from solution of the Schrödinger equation and the associated ground state density n_0, can be represented as,

$$V_{\text{ext}}(\boldsymbol{r}) \Longleftrightarrow |\Psi_0\rangle \Longleftrightarrow n_0(\boldsymbol{r}) = \langle\Psi_0|\hat{n}(\boldsymbol{r})|\Psi_0\rangle \tag{3.8}$$

Second H-K theorem The second theorem establishes a variational principle;

For any positive definite trial density n, such that $\int n(\mathbf{r})d\mathbf{r} = N$ we have $E[n] \geq E_0$, where E_0 denotes the ground state density.

From the first theorem we know that the trial density determines a unique trial Hamiltonian H and thus wave-function Ψ: E$[n]$=$\langle\Psi|H|\Psi\rangle \geq E_0$ follows immediately from the variational theorem of the Schrödinger equation. This theorem restricts density functional theory to studies of the ground state.

The Hohenberg-Kohn shows that the density can be used to calculate the ground state energy of the system, but practical applications were still unknown. The Kohn Sham theory, which will be described in the section (3.2.3), enabled the realistic solution of the many body problem via the application of two H-K theorems.

3.2.2 Energy functional

From the H-K theorems, it is known that the total energy E of the ground state is a universal functional of the corresponding density.

From equation (3.2) we can write the energy as a functional of density as,

$$E[n] = T[n] + \int drn(r)V_{ext}(r) + E_{ee}[n] \tag{3.9}$$

where, $E[n]$ is the total energy of an interacting system. On the other hand, the kinetic energy $T[n]$ and the electron-electron interaction term $E_{ee}[n]$ are unknown for an interacting system. The kinetic energy($T^s[n]$) and electron-electron interaction ($E^s_{ee}[n]$) term for the non-interacting system is known.

The total energy of an interacting system can be reformulated in terms of a non-interacting system as:

$$E[n] = T[n] + \int drn(r)V_{ext}(r) + E_{ee}[n] + T^s[n] - T^s[n] + E^s_{ee}[n] - E^s_{ee}[n] \tag{3.10}$$

In the Hartree theory, the energy functional for the non-interacting system can be written as,

$$E^H[n] = T^s[n] + \int d\mathbf{r}n(\mathbf{r})V_{ext}(\mathbf{r}) + E^s_{ee}[n] \tag{3.11}$$

where,

$$E^s_{ee}[n] = \frac{1}{2}\int d\mathbf{r}d\mathbf{r}'\frac{n(\mathbf{r})n(\mathbf{r}')}{|\mathbf{r}-\mathbf{r}'|} \tag{3.12}$$

and hence the energy of the interacting system can be written as,

$$E[n] = E^H[n] + E_{xc}[n] \tag{3.13}$$

where the unknown term E_{xc} is the exchange-correlation (xc) energy which is written,

$$E_{xc}[n] = T[n] - T^s[n] + E_{ee}[n] - E^s_{ee}[n] \tag{3.14}$$

and has to be approximated to be a useful expression.

3.2.3 Kohn-Sham approach

The Kohn-Sham approach states that for each system of interacting electrons, an auxiliary system of non-interacting electrons exists which has the same electronic density. The wavefunction of a system of N independent particles can be written as a Slater determinant of N single-particle orbitals. These orbitals are the solution of a Schrödinger-like equation, containing a kinetic term and a potential term V_{eff}:

$$\left[-\frac{1}{2}\nabla^2 + V_{\text{eff}}(\mathbf{r})\right]\phi_i(\mathbf{r}) = E_i\phi_i(\mathbf{r}) \tag{3.15}$$

where,

$$V_{\text{eff}}(\mathbf{r}) = V_{ext}(\mathbf{r}) + V^H([n],\mathbf{r}) + V_{xc}([n],\mathbf{r}) \tag{3.16}$$

with,

$$V^H([n],\mathbf{r}) = \int d\mathbf{r}'\frac{n(\mathbf{r}')}{|\mathbf{r}-\mathbf{r}'|}, \qquad V_{xc}([n],\mathbf{r}) = \frac{\delta E_{xc}[n]}{\delta n(\mathbf{r})} \tag{3.17}$$

In this case, the electron density is simply the sum of the square modulus of the first N states occupied by the first N electrons.

$$n(\mathbf{r}) = \sum_i^N |\phi_i(\mathbf{r})|^2 \tag{3.18}$$

The energy of the system of independent particle is described by the effective potential V_{eff} so that,

$$E^s[n] = T^s[n] + \int d\mathbf{r} n(\mathbf{r})V_{\text{eff}}(\mathbf{r}) \tag{3.19}$$

using the expression of equation (3.16), we get the energy of the non-interacting system as,

$$E^s[n] = T^s[n] + \int d\mathbf{r} n(\mathbf{r})V_{ext}(\mathbf{r}) + \frac{1}{2}\int d\mathbf{r}d\mathbf{r}'\frac{n(\mathbf{r})n(\mathbf{r}')}{|\mathbf{r}-\mathbf{r}'|} + E_{xc}[n] \tag{3.20}$$

which is the same as equation (3.13) the energy of the interacting system. Hence the Kohn-Sham approach substitutes the problem of interacting electrons with an auxiliary independent-particle problem, in which all many body effects beyond the Hartree term is incorporated in an explicit exchange-correlation functional.

However, the main difficulty before solving these equations is to find an explicit form of the exchange-correlation potential. Then, the equations are solved self-consistently, and the ground state density $n(\mathbf{r})$ of the interacting system is constructed by the solutions of the non-interacting system.

3.2.4 Approximation for the exchange-correlation potential

The exchange and correlation term can be written separately in the E_{xc} as,

$$E_{\mathbf{xc}}[n] = E_{\mathbf{x}}[n] + E_c[n] \tag{3.21}$$

Local density approximation

There are many approximations for the exchange-correlation potential. The simplest approximation is the local density approximation (LDA) [17], in which the potential is a local functional of the density and is based on the homogeneous electron gas.

The energy density for a homogeneous electron gas can be written as a sum of a kinetic energy density and an exchange-correlation energy density as,

$$E^{\text{hom}} = E^{\text{hom}}_{\text{kin}} + E^{\text{hom}}_{\text{xc}} \tag{3.22}$$

where, the kinetic energy is given as,

$$E^{\text{hom}}_{\text{kin}} = \frac{(3\pi^2 n)^{5/3}}{10\pi^2} \tag{3.23}$$

and the exchange terms is given as,

$$E^{\text{LDA}}_x [n] = \int d^3 r n(\boldsymbol{r}) \epsilon^{\text{HES}}_x (n(\boldsymbol{r})) \tag{3.24}$$

where, ϵ_{x} is known as a function of the density n, which is constant and is given as,

$$\epsilon^{\text{HES}}_{\text{x}} = \frac{(3\pi^2 n)^{4/3}}{4\pi^3} \tag{3.25}$$

No exact analytical formula is known for the correlation energy density, but approximate formulas based on Quantum Monte Carlo (QMC) data [18–20] are provided.

In LDA, the exchange-correlation energy of the real system at one point $\mathbf{r}$, with density $\bar{n} = n(\mathbf{r})$, is approximated by the exchange-correlation energy of the homogeneous electron gas with the same density at that point.

Local spin density approximation

In the local spin density approximation (LSDA) [21], the exchange part can be written as,

$$E^{\text{LSDA}}_x [n_\uparrow, n_\downarrow] = \int d^3 r n(\boldsymbol{r}) \epsilon^{\text{HES}}_x (n_\uparrow(\boldsymbol{r}), n_\downarrow(\boldsymbol{r})) \tag{3.26}$$

$$\begin{aligned} \epsilon^{\text{HES}}_x (n_\uparrow(\boldsymbol{r}), n_\downarrow(\boldsymbol{r})) = \quad & \epsilon^{\text{HES}}_x (n(\boldsymbol{r})) \tfrac{[1+\zeta(\boldsymbol{r})]^{4/3} + [1-\zeta(\boldsymbol{r})]^{4/3}}{2} \\ & = -\tfrac{3\left(3\pi^2 n(\boldsymbol{r})\right)^{1/3}}{4\pi} \tfrac{[1+\zeta(\boldsymbol{r})]^{4/3} + [1-\zeta(\boldsymbol{r})]^{4/3}}{2} \end{aligned} \tag{3.27}$$

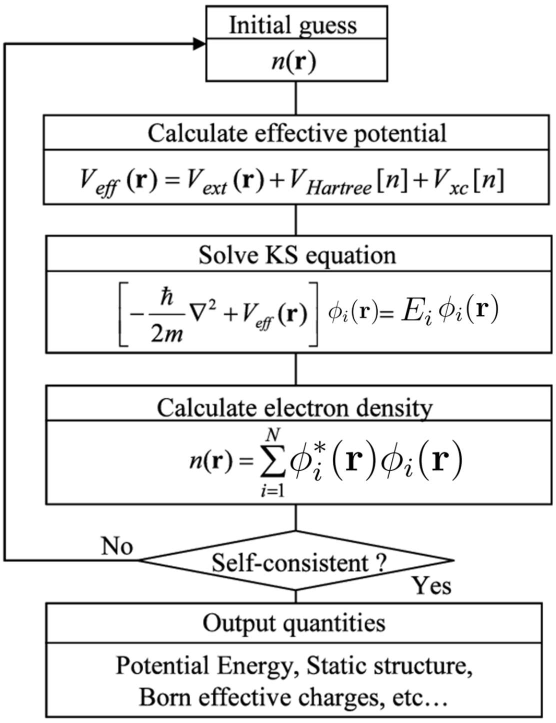

Figure 3.1: Flow chart to describe KS approach

where,

$$\zeta(\boldsymbol{r}) = \frac{n_\uparrow(\boldsymbol{r}) - n_\downarrow(\boldsymbol{r})}{n_\uparrow(\boldsymbol{r}) + n_\downarrow(\boldsymbol{r})} \quad n = n_\downarrow + n_\uparrow \tag{3.28}$$

is the induced spin-polarization. The correlation part is given as,

$$E_c^{\text{LDA}}[n_\uparrow, n_\downarrow] = \int d^3r n(\boldsymbol{r})\epsilon_c^{\text{HES}}(n(\boldsymbol{r}), \zeta(\boldsymbol{r})) \tag{3.29}$$

Exact $\epsilon_c^{\text{HES}}(n, \zeta)$ is not known analytically, but there are plenty of approximate results from the theory, and numerically exact results from QMC [18].

3.2.5 Practical use of DFT

Here, the use of DFT to determine the ground-state electronic properties of a system is showed, as schematized in the figure (3.1). To determine the effective potential V_{eff}, the procedure begins by considering an arbitrary density value. Following that, the KS equations are solved and a new density is built with the solution of the KS equations. If the resulting density corresponds with the initially considered arbitrary density, it will be taken as the system's density by using convergence criterion. The procedure is repeated if the new density is not identical to the estimated density. The effective potential is now determined using the new density, and the Kohn-Sham equations are solved once again. This step is repeated until the self-consistent density is obtained. This self-consistent density will be considered the true ground state density of the system and will be used to determine the properties of the system.

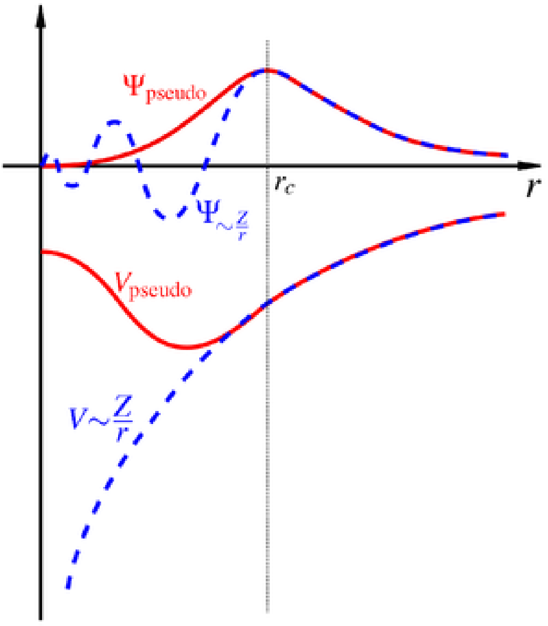

Figure 3.2: Description of pseudopotential approximation

3.3 Pseudopotential approximation

The pseudopotential approximation has been used in the DFT calculations. This approximation is described in detail here.

Electrons in condensed matter are classified into two types: core electrons and valence electrons. The electrons with closed shells that are close to the nucleus are referred to as core electrons. Valence electrons are located beyond the core area and are responsible for the system's physical properties.

We observed that core electron orbitals are highly localized, and the numerical evaluation of these orbitals is challenging.

In order to account for this, the pseudopotential approximation has been proposed. In this approximation, the core electrons and the strong nuclear potential are removed and replaced by a smoother and weaker pseudopotential. This pseudopotential acts on a set of pseudo wavefunctions rather than the true valence wavefunctions. In fact, the pseudopotential can be optimized so that, in practice, it is even weaker than the frozen core potential.

The schematic diagram in figure (3.2) shows these quantities. Due to the strong ionic potential, the valence wavefunctions oscillate rapidly in the region inhabited by the core electrons. These oscillations ensure that the core and valence electrons remain orthogonal. The pseudopotential is constructed in such a way that there are no radial nodes in the pseudo wavefunction in the core area and that the pseudo wavefunctions and pseudopotentials are identical to the all-electron wavefunctions and potentials outside a region defined by a radius cut-off. This requirement must be examined carefully, since the pseudopotential may introduce additional non-physical states (referred to as ghost states) into the calculation.

3.4 Summary

In this chapter, we discussed the many body problem. The density functional approach is a way to solve the many body problems discussed in this chapter. An approximation to the exchange-correlation kernel, the key quantity in the DFT, has been discussed. Furthermore, the practical uses of DFT on real systems the use of pseudopotential approximation in DFT has been discussed. However, DFT is limited to calculate only the ground-state properties of a system. In order to calculate the excited state properties of a system, time-dependent density functional theory (TDDFT) is used and will be discussed in the next chapter.

Chapter 4

Time-dependent density functional theory

Excited state calculations are not possible using static ground-state DFT. Interpreting KS eigenvalues as electron addition or removal energies or KS eigenvalue differences as optical excitation energies often results in significant disparities between theory and experiment. Time-dependent many-body Schrödinger equation, described in section (4.1), is used to obtain the solution to the excited states properties. As a consequence, a time-dependent DFT, also known as a TDDFT extension of static DFT (which will be discussed in the section (4.2)), and has been proposed as a potential substitute [22,23], to solve the time-dependent many-body problems. Thereafter, using this theory, the calculation of the linear and second-order response functions is described in detail in the following sections (4.2.3) and (4.2.5) respectively. For the linear response, two cases are presented corresponding to non-magnetic and magnetic materials. For the second-order, only response functions for non-magnetic materials will be described in this chapter.

4.1 Time-dependent many-body problem

The Time-dependent many-body problem can be expressed using the Schrödinger equation as,

$$\hat{H}(t)\Psi(t) = \mathrm{i}\frac{\partial\Psi(t)}{\partial t}, \tag{4.1}$$

where,

$$\hat{H}(t) = \hat{T} + \hat{V}_{\mathrm{ee}} + \hat{V}_{ext}(t) \tag{4.2}$$

where, $\hat{T}$ is the kinetic energy which is expressed by the equation (3.3) and the $\hat{V}_{\mathrm{ee}}$ is the electron-electron repulsion, which can be expressed by the equation (3.4).

The "external potential($\hat{V}_{\mathrm{ext}}(t)$)" represents the potential that the electrons experience due to the nuclear attraction and to any time-dependent field applied to the system (e.g. laser).

$$\hat{V}_{\mathrm{ext}}(t) = \sum_{i=1}^{N} V_{\mathrm{ext}}(\boldsymbol{r}_i, t) \tag{4.3}$$

For a large number of electrons the equation (4.1) is very difficult to solve. As time-dependent external potentials adds an additional layer of complexity to the equations. Similar to how DFT offered a method for solving the time-independent many-body issue, TDDFT offers a method for solving the time-dependent many-body problem as discussed in the next section.

4.2 Time-dependent density functional theory

Over the years, Time-Dependent Density Functional Theory (TDDFT) has become one of the well-established first-principles' approaches to describe the time-dependent phenomena for a large variety of systems, both in the linear-response regime and beyond. Similar to the Hohenberg-Kohn and Kohn-Sham approach, Runge and Gross have proposed an approach to solve the time-dependent many-body problem. It is based on the following theorem.

4.2.1 Runge-Gross Theorem

For every single-particle potential $V_{ext}(\mathbf{r}, t)$ which can be expanded into a Taylor series with respect to the time coordinates around $t = t_0$, a map $V_{ext}(\mathbf{r}, t) \rightarrow n(\overrightarrow{\mathbf{r}}, t)$ is defined by solving the time-dependent Schrödinger equation with a fixed initial state $\Psi(t_0) = \Psi_0$ and calculating the corresponding densities $n(r, t)$. This map can be inverted up to an additive merely time-dependent function in the potential.

Using this theorem it is possible to practically solve the time-dependent problem and to get the time-dependent density.

4.2.2 Time-dependent Kohn Sham scheme

The density of the interacting system can be obtained from,

$$n(\mathbf{r}, t) = \sum_{j=1}^{N} |\phi_j(\mathbf{r}, t)|^2 \tag{4.4}$$

where, the orbitals $\phi_j(\mathbf{r}, t)$ satisfy the time-dependent KS equation which can be written as one particle equation like in static case.

$$i\frac{\partial}{\partial t}\phi_j(\mathbf{r}, t) = \left(-\frac{\nabla^2}{2} + V_{\text{eff}}[n](\mathbf{r}, t)\right)\phi_j(\mathbf{r}, t) \tag{4.5}$$

By analogy with the static case the single-particle potential $V_{\text{eff}}[n]$ is written as,

$$V_{\text{eff}}[n](\mathbf{r}, t) = V_{ext}(\mathbf{r}, t) + \int d^3r' \frac{n(\mathbf{r}', t)}{|\mathbf{r} - \mathbf{r}'|} + V_{\mathbf{xc}}[n](\mathbf{r}, t) \tag{4.6}$$

In this approach also, the main difficulty is to get a good approximation for the accurate exchange correlation potential.

4.2.3 Linear response

When a system is submitted to a time-dependent external perturbation, the electronic density is changing in time. For sufficiently weak perturbation, the relation between the change of the density and the perturbation can be evaluated in the framework of perturbation theory. In the following we briefly present the derivation of the linear response, in the case of non-magnetic material. This will allow us to define the important quantities and the approximations routinely used in numerical calculations.

Due to the change of the external potential, $V_{ext}^{(1)}$, the density is written, to first-order as ,

$$n(\mathbf{r},t) = n^{(0)}(\mathbf{r},t) + n^{(1)}(\mathbf{r},t) \tag{4.7}$$

and the Hartree and exchange-correlation potentials become,

$$V^H(n,\mathbf{r},t) = \int d\mathbf{r}' \frac{n^{(0)}(\mathbf{r}',t) + n^{(1)}(\mathbf{r}',t)}{|\mathbf{r}-\mathbf{r}'|} \tag{4.8}$$

$$V_{xc}(n,\mathbf{r},t) = V_{xc}(n^{(0)},\mathbf{r},t) + \int d\mathbf{r}'dt' \frac{\delta V_{xc}(\mathbf{r},t)}{\delta n(\mathbf{r}',t')} n^{(1)}(\mathbf{r}',t')$$

Defining the exchange-correlation kernel f_{xc} by,

$$f_{xc}(\mathbf{r},t,\mathbf{r}',t') = \frac{\delta V_{xc}(\mathbf{r},t)}{\delta n(\mathbf{r}',t')} \tag{4.9}$$

$$f_{vxc}(\mathbf{r},t,\mathbf{r}',t') = \frac{\delta(t-t')}{|\mathbf{r}-\mathbf{r}'|} + f_{xc}(n,\mathbf{r},t,\mathbf{r}',t') \tag{4.10}$$

the linear change in the effective potential is,

$$V_{\text{eff}}^{(1)}(\mathbf{r},t) = V_{ext}^{(1)}(\mathbf{r},t) + \int d\mathbf{r}'dt' f_{uxc}(\mathbf{r},t,\mathbf{r}',t') n^{(1)}(\mathbf{r}',t') \tag{4.11}$$

The response function $\chi_0^{(1)}$ is defined through the relation between the effective potential V_{eff} and the first-order induced density,

$$n^{(1)}(\mathbf{r},t) = \int d\mathbf{r}'dt' \chi_0^{(1)}(\mathbf{r},t,\mathbf{r}',t') V_{\text{eff}}^{(1)}(\mathbf{r}',t') \tag{4.12}$$

In frequency space, we get,

$$n^{(1)}(\mathbf{r},\omega) = \int d\mathbf{r}' \chi_0^{(1)}(\mathbf{r},\mathbf{r}',\omega) V_{\text{eff}}^{(1)}(\mathbf{r}',\omega) \tag{4.13}$$

Equation (4.11) becomes,

$$V_{\text{eff}}^{(1)}(\mathbf{r},\omega) = V_{ext}^{(1)}(\mathbf{r},\omega) + \int d\mathbf{r}' f_{vxc}(\mathbf{r},\mathbf{r}',\omega) n^{(1)}(\mathbf{r}',\omega) \tag{4.14}$$

Taking equations (4.13) and (4.14) together, we get,

$$\begin{aligned} n^{(1)}(\mathbf{r},\omega) = &\int d\mathbf{r}' \chi_0^{(1)}(\mathbf{r},\mathbf{r}',\omega) V_{ext}^{(1)}(\mathbf{r}',\omega) + \\ &+ \int d\mathbf{r}'d\mathbf{r}'' \chi_0^{(1)}(\mathbf{r},\mathbf{r}',\omega) f_{vxc}(\mathbf{r}',\mathbf{r}'',\omega) n^{(1)}(\mathbf{r}'',\omega) \end{aligned} \tag{4.15}$$

The induced density $n^{(1)}$ is also related to the external potential (V_{ext}), as,

$$n^{(1)}(\mathbf{r},\omega) = \int d\mathbf{r}' \chi^{(1)}(\mathbf{r},\mathbf{r}',\omega) V_{ext}^{(1)}(\mathbf{r}',\omega) \tag{4.16}$$

where $\chi^{(1)}(r,r',\omega)$ is a response function called full polarizability.
The relation between $\chi^{(1)}$ and $\chi_0^{(1)}$ is,

$$\chi^{(1)}(\mathbf{r},\mathbf{r}',\omega) = \chi_0^{(1)}(\mathbf{r},\mathbf{r}',\omega) + \int d\mathbf{r}'' d\mathbf{r}''' \chi_0^{(1)}(\mathbf{r},\mathbf{r}'',\omega) f_{vxc}(\mathbf{r}'',\mathbf{r}''',\omega) \chi^{(1)}(\mathbf{r}''',\mathbf{r}',\omega) \tag{4.17}$$

which can also be expressed in momentum space as

$$\begin{aligned} \chi^{(1)}(\mathbf{q}+\mathbf{G},\mathbf{q}+\mathbf{G}',\omega) &= \chi_0^{(1)}(\mathbf{q}+\mathbf{G},\mathbf{q}+\mathbf{G}',\omega) + \\ &\sum_{G_1 G_2} \chi_0^{(1)}(\mathbf{q}+\mathbf{G},\mathbf{q}+\mathbf{G}_1,\omega)\, f_{vxc}(\mathbf{q}+\mathbf{G}_1,\mathbf{q}+\mathbf{G}_2,\omega)\, \chi^{(1)}(\mathbf{q}+\mathbf{G}_2,\mathbf{q}+\mathbf{G}',\omega) \end{aligned} \tag{4.18}$$

For simplicity, this Dyson equation, in position space or in momentum space, can be formally written as,

$$\chi^{(1)} = \chi_0^{(1)} + \chi_0^{(1)} f_{vxc} \chi^{(1)} \tag{4.19}$$

The response function $\chi_0^{(1)}$, called **Independent Particle Response Function** is,

$$\chi_0^{(1)}(\mathbf{r},\mathbf{r}',\omega) = \sum_{ij} (f_i - f_j) \frac{\phi_i^*(\mathbf{r})\phi_j(\mathbf{r})\phi_j^*(\mathbf{r}')\phi_i(\mathbf{r}')}{E_i - E_j + \omega + i\eta} \tag{4.20}$$

where ϕ_i and E_i denote the Kohn-Sham(KS) eigenfunctions and eigenvalues and η is a small positive quantity acting as a broadening ($\eta \to 0^+$).

In reciprocal space, using Bloch functions, we can write,

$$\begin{aligned} \chi_0^{(1)}(\mathbf{q}+\mathbf{G},\mathbf{q}+\mathbf{G}',\omega) &= \frac{2}{V} \sum_{nn'\mathbf{k}} \frac{(f_{n,\mathbf{k}} - f_{n',\mathbf{k}+\mathbf{q}})}{E_{n,\mathbf{k}} - E_{n',\mathbf{k}+\mathbf{q}} + \omega + i\eta} \\ &< \phi_{n,\mathbf{k}} | e^{-i(\mathbf{q}+\mathbf{G})\mathbf{r}} | \phi_{n',\mathbf{k}+\mathbf{q}} >< \phi_{n',\mathbf{k}+\mathbf{q}} | e^{-i(\mathbf{q}+\mathbf{G}')\mathbf{r}'} | \phi_{n,\mathbf{k}} > \end{aligned} \tag{4.21}$$

where the factor 2 comes from the summation over spins.

Exchange correlation kernel

In the linear response regime, as shown in equations (4.17) and (4.18), the main element is the so-called exchange-correlation kernel f_{xc}. Equation (4.9) defines this quantity as the functional derivative of the xc potential with respect to the density. Its functional form is unknown and has to be approximated. Finding a good approximation for f_{xc} is challenging, as it has to incorporate the excitonic interaction, which is important for an accurate description of the absorption processes.

Several approximations for the exchange-correlation kernel are already available and implemented in numerical codes. The simplest ones are described below.

Independent Particle Approximation

Among all, the simplest approximation is the Independent Particle Approximation, where only $\chi_0^{(1)}$, defined by (4.21), is used with $G = G' = 0$, and

$$\epsilon_M(\mathbf{q},\omega) = 1 - v_0\chi_0^{(1)}(\mathbf{q},\mathbf{q},\omega) \tag{4.22}$$

where, ϵ_M is the macroscopic dielectric function and v is the coulomb potential.

Random Phase Approximation (RPA)

In RPA, we set $f_{xc} = 0$, and the Dyson equation becomes

$$\chi^{(1)} = \chi_0^{(1)} + \chi_0^{(1)} v \chi^{(1)} \tag{4.23}$$

Using equation 4.22 and 4.23, the inverse dielectric function is defined as,

$$\epsilon^{-1} = 1 + v\chi^{(1)} \tag{4.24}$$

Other approximations for the xc kernels are available, and the description of these kernels will be provided in the last part of the thesis.

4.2.4 Linear response including spin-polarization in TDDFT

In magnetic material, the spin components of the density has to be taken into account explicitly in the derivation of the Dyson equation. The total density is the sum of the two components $n^{\uparrow}$ and $n^{\downarrow}$ which can be different ($n^{\uparrow}(\mathbf{r}) \neq n^{\downarrow}(\mathbf{r})$) and the exchange correlation potential is defined by,

$$V_{xc}^{\alpha} = \frac{\partial E_{xc}}{\partial n^{\alpha}} \tag{4.25}$$

In the following, for simplicity, only the spin-dependence will be written explicitly.

Due to the perturbation, the exchange correlation kernel becomes to first-order

$$V_{xc}^{\alpha} = V_{xc}^{(0)\alpha} + \sum_{\beta} \frac{\delta V_{xc}^{\alpha}}{\delta n^{\beta}} n^{(1)\beta} \tag{4.26}$$

and the spin-dependent kernel $f_{xc}^{\alpha\beta}$ is defined as,

$$f_{xc}^{\alpha\beta} = \frac{\delta V_{xc}^{\alpha}}{\delta n^{\beta}} \tag{4.27}$$

By using the same procedure as the one explained for the spin-independent case in the previous subsection, we obtain,

$$\chi^{(1)\alpha\beta} = \chi_0^{(1)^{\alpha\beta}} + \sum_{\gamma\delta} \chi_0^{(1)^{\alpha\gamma}} f_{uxc}^{\gamma\delta} \chi^{(1)\delta\beta} \tag{4.28}$$

where, spin-dependent response functions are defined as

$$\chi^{(1)\alpha\beta} = \frac{\delta n^{(1)\alpha}}{\delta V_{ext}^{\beta}} \qquad \chi_0^{(1)\alpha\beta} = \frac{\delta n^{(1)\alpha}}{\delta V^{\beta}} \tag{4.29}$$

As we are interested in optical processes we will only consider V_{ext} not acting on the spin. The non-interacting response function χ_0 being diagonal in spin, we get two sets of decoupled equations

$$\begin{pmatrix} \chi^{\uparrow\uparrow} \\ \chi^{\downarrow\uparrow} \end{pmatrix} = \begin{pmatrix} \chi_0^{\uparrow} \\ 0 \end{pmatrix} + M \begin{pmatrix} \chi^{\uparrow\uparrow} \\ \chi^{\downarrow\uparrow} \end{pmatrix}$$

$$\begin{pmatrix} \chi^{\uparrow\downarrow} \\ \chi^{\downarrow\downarrow} \end{pmatrix} = \begin{pmatrix} 0 \\ \chi_0^{\downarrow} \end{pmatrix} + M \begin{pmatrix} \chi^{\uparrow\downarrow} \\ \chi^{\downarrow\downarrow} \end{pmatrix}$$

with,

$$M = \begin{pmatrix} \chi_0^{\uparrow} f_{uxc}^{\uparrow\uparrow} & \chi_0^{\uparrow} f_{uxc}^{\uparrow\downarrow} \\ \chi_0^{\downarrow} f_{uxc}^{\downarrow\uparrow} & \chi_0^{\downarrow} f_{uxc}^{\downarrow\downarrow} \end{pmatrix}$$

Summing the 2 matrix equations, the resulting equation is

$$\begin{pmatrix} \chi^{\uparrow\uparrow} + \chi^{\uparrow\downarrow} \\ \chi^{\downarrow\uparrow} + \chi^{\downarrow\downarrow} \end{pmatrix} = \begin{pmatrix} \chi_0^{\uparrow} \\ \chi_0^{\downarrow} \end{pmatrix} + M \begin{pmatrix} \chi^{\uparrow\uparrow} + \chi^{\uparrow\downarrow} \\ \chi^{\downarrow\uparrow} + \chi^{\downarrow\downarrow} \end{pmatrix}$$

This matrix equation can be written as a Dyson equation for the two new response functions $\chi^{\uparrow} = \chi^{\uparrow\uparrow} + \chi^{\uparrow\downarrow}$ and $\chi^{\downarrow} = \chi^{\downarrow\uparrow} + \chi^{\downarrow\downarrow}$,

$$\begin{pmatrix} \chi^{\uparrow} \\ \chi^{\downarrow} \end{pmatrix} = \begin{pmatrix} \chi_0^{\uparrow} \\ \chi_0^{\downarrow} \end{pmatrix} + M \begin{pmatrix} \chi^{\uparrow} \\ \chi^{\downarrow} \end{pmatrix}$$

Considering that the external potential does not depend on the spin, the total density $n^{(1)} = \sum_\alpha n^{(1)\alpha}$ is given by

$$n^{(1)} = \sum_{\alpha\beta} \chi^{\alpha\beta} V_{ext}^{(1)} \tag{4.30}$$

and the total response function is defined as,

$$\chi = \sum_{\alpha} \sum_{\beta} \chi^{\alpha\beta} = \sum_{\alpha} \chi^{\alpha} \tag{4.31}$$

Defining the spin-dependent dielectric function $(\epsilon^{-1})^{\alpha\beta}$ by,

$$V^{\alpha} = \sum_{\beta} (\epsilon^{-1})^{\alpha\beta} V_{ext}^{\beta} \tag{4.32}$$

which gives,

$$(\epsilon^{-1})^{\alpha\beta} = \delta_{\alpha\beta} + v \sum_{\gamma} \chi^{\gamma\beta} \tag{4.33}$$

For spin-independent external potentials, ($V_{ext}^{\uparrow} = V_{ext}^{\downarrow} = V_{ext}$) the spin-averaged quantity is defined by summing over β

$$(\epsilon^{-1})^{\alpha} = \sum_{\beta} (\epsilon^{-1})^{\alpha\beta} = 1 + v \sum_{\beta} \sum_{\gamma} \chi^{\gamma\beta} = 1 + v\chi \tag{4.34}$$

which does not depend on the spin. The macroscopic dielectric function is then obtained from ϵ^{-1} as in the spin-independent case. Note that such a derivation of the macroscopic dielectric function has already been given in the framework of many-body perturbation theory in reference [24].

4.2.5 Second-order response function

Independent Particle Approximation (IPA)

The reference [25] describes an ab initio theory of second-order optical processes in solids that accounts for both microscopic quantum mechanical (many-body) effects and their macroscopic counterparts.

The microscopic second-order response $\chi_0^{(2)}$ in the framework of perturbation theory is

$$\begin{aligned}\chi_0^{(2)}(\mathbf{r},\mathbf{r}',\mathbf{r}'',\omega',\omega'') = \sum_{ijk} \frac{\phi_i^*(\mathbf{r})\phi_j(\mathbf{r})}{(E_i - E_j + \omega' + \omega'' + 2i\eta)} \\ \Bigg[(f_i - f_k)\frac{\phi_j^*(\mathbf{r}')\phi_k(\mathbf{r}')\phi_k^*(\mathbf{r}'')\phi_i(\mathbf{r}'')}{(E_i - E_k + \omega'' + i\eta)} + (f_i - f_k)\frac{\phi_k^*(\mathbf{r}')\phi_i(\mathbf{r}')\phi_j^*(\mathbf{r}'')\phi_k(\mathbf{r}'')}{(E_i - E_k + \omega' + i\eta)} \\ +(f_j - f_k)\frac{\phi_k^*(\mathbf{r}')\phi_i(\mathbf{r}')\phi_j^*(\mathbf{r}'')\phi_k(\mathbf{r}'')}{(E_k - E_j + \omega'' + i\eta)} + (f_j - f_k)\frac{\phi_j^*(\mathbf{r}')\phi_k(\mathbf{r}')\phi_k^*(\mathbf{r}'')\phi_i(\mathbf{r}'')}{(E_k - E_j + \omega' + i\eta)}\Bigg]\end{aligned} \tag{4.35}$$

where $\eta \to 0^+$ and $\chi_0^{(2)}$ in the momentum space is written below,

$$\begin{aligned}\chi_0^{(2)}(\mathbf{q}_1 + \mathbf{q}_2 + \mathbf{G}, \mathbf{q}_1 + \mathbf{G}', \mathbf{q}_2 + \mathbf{G}'', \omega, \omega) = \frac{2}{V} \sum_{n,n',n'',\mathbf{k}} \frac{< \phi_{n,\mathbf{k}}|e^{-i(\mathbf{q}_1+\mathbf{q}_2+\mathbf{G})\mathbf{r}}|\phi_{n',\mathbf{k}+\mathbf{q}_1+\mathbf{q}_2} >}{(E_{n,\mathbf{k}} - E_{n',\mathbf{k}+\mathbf{q}_1+\mathbf{q}_2} + 2\omega + 2i\eta)} \\ \Bigg[(f_{n,\mathbf{k}} - f_{n'',\mathbf{k}+\mathbf{q}_2})\frac{< \phi_{n',\mathbf{k}+\mathbf{q}_1+\mathbf{q}_2}|e^{i(\mathbf{q}_1+\mathbf{G}')\mathbf{r}'}|\phi_{n'',\mathbf{k}+\mathbf{q}_2} >< \phi_{n'',\mathbf{k}+\mathbf{q}_2}|e^{i(\mathbf{q}_2+\mathbf{G}'')\mathbf{r}''}|\phi_{n,\mathbf{k}} >}{(E_{n,\mathbf{k}} - E_{n'',\mathbf{k}+\mathbf{q}_2} + \omega + i\eta)} \\ +(f_{n,\mathbf{k}} - f_{n'',\mathbf{k}+\mathbf{q}_1})\frac{< \phi_{n'',\mathbf{k}+\mathbf{q}_1}|e^{i(\mathbf{q}_1+\mathbf{G}')\mathbf{r}'}|\phi_{n,\mathbf{k}} >< \phi_{n',\mathbf{k}+\mathbf{q}_1+\mathbf{q}_2}|e^{i(\mathbf{q}_2+\mathbf{G}'')\mathbf{r}''}|\phi_{n'',\mathbf{k}+\mathbf{q}_1} >}{(E_{n,\mathbf{k}} - E_{n'',\mathbf{k}+\mathbf{q}_1} + \omega + i\eta)} \\ +(f_{n',\mathbf{k}+\mathbf{q}_1+\mathbf{q}_2} - f_{n'',\mathbf{k}+\mathbf{q}_1})\frac{< \phi_{n'',\mathbf{k}+\mathbf{q}_1}|e^{i(\mathbf{q}_1+\mathbf{G}')\mathbf{r}'}|\phi_{n,\mathbf{k}} >< \phi_{n',\mathbf{k}+\mathbf{q}_1+\mathbf{q}_2}|e^{i(\mathbf{q}_2+\mathbf{G}'')\mathbf{r}''}|\phi_{n'',\mathbf{k}+\mathbf{q}_1} >}{(E_{n'',\mathbf{k}+\mathbf{q}_1} - E_{n',\mathbf{k}+\mathbf{q}_1+\mathbf{q}_2} + \omega + i\eta)} \\ +(f_{n',\mathbf{k}+\mathbf{q}_1+\mathbf{q}_2} - f_{n'',\mathbf{k}+\mathbf{q}_2}) + \frac{< \phi_{n',\mathbf{k}+\mathbf{q}_1+\mathbf{q}_2}|e^{i(\mathbf{q}_1+\mathbf{G}')\mathbf{r}'}|\phi_{n'',\mathbf{k}+\mathbf{q}_2} >< \phi_{n'',\mathbf{k}+\mathbf{q}_2}|e^{i(\mathbf{q}_2+\mathbf{G}'')\mathbf{r}''}|\phi_{n,\mathbf{k}} >}{(E_{n'',\mathbf{k}+\mathbf{q}_2} - E_{n',\mathbf{k}+\mathbf{q}_1+\mathbf{q}_2} + \omega + i\eta)}\Bigg]\end{aligned} \tag{4.36}$$

Dyson equation of second-order response function

As detailed for the linear response function, the crystal local field effects as well as exchange-correlation effects are accounted for by solving a Dyson-like equation that relates the KS response function to the full full polarizability. Such a Dyson equation can also be derived for second-order response functions and we briefly outline the derivation for the spin-independent case, as shown in Ref [25].

In this case a second-order exchange correlation kernel g_{xc} appears

$$g_{xc}(\mathbf{r},t,\mathbf{r}',t',\mathbf{r}'',t'') \quad = \quad \frac{\delta^2 V_{xc}(\mathbf{r},t)}{\delta n(\mathbf{r}',t')\delta n(\mathbf{r}'',t'')} \tag{4.37}$$

and the change in the density and in the effective potential can be written in frequency space,

$$\begin{aligned}n^{(2)}(\mathbf{r},\omega) = &\int d\mathbf{r}'\chi_0^{(1)}(\mathbf{r},\mathbf{r}',\omega)V_{\text{eff}}^{(2)}(\mathbf{r}',\omega)\\ &+\frac{1}{2}\int d\mathbf{r}'d\mathbf{r}''d\omega'\chi_0^{(2)}(\mathbf{r},\mathbf{r}',\mathbf{r}'',\omega',\omega-\omega')V_{\text{eff}}^{(1)}(\mathbf{r}',\omega')V_{\text{eff}}^{(1)}(\mathbf{r}'',\omega-\omega')\end{aligned} \tag{4.38}$$

$$\begin{aligned}V_{\text{eff}}^{(2)}(\mathbf{r},\omega) = &\int d\mathbf{r}'f_{uxc}(\mathbf{r},\mathbf{r}',\omega)n^{(2)}(\mathbf{r}',\omega)\\ &+\frac{1}{2}\int d\mathbf{r}'d\mathbf{r}''d\omega'g_{xc}(\mathbf{r},\mathbf{r}',\mathbf{r}'',\omega',\omega-\omega')n^{(1)}(\mathbf{r}',\omega')n^{(1)}(\mathbf{r}'',\omega-\omega')\end{aligned} \tag{4.39}$$

Taking equation (4.38) and equation (4.39) together, we have

$$\begin{aligned}n^{(2)}(\mathbf{r},\omega) = &\int d\mathbf{r}'d\mathbf{r}''\chi_0^{(1)}(\mathbf{r},\mathbf{r}',\omega)f_{uxc}(\mathbf{r}',\mathbf{r}'',\omega)n^{(2)}(\mathbf{r}'',\omega)\\ &+\frac{1}{2}\int d\mathbf{r}'d\mathbf{r}''d\mathbf{r}'''d\omega'\chi_0^{(1)}(\mathbf{r},\mathbf{r}',\omega)g_{xc}(\mathbf{r}',\mathbf{r}'',\mathbf{r}''',\omega',\omega-\omega')n^{(1)}(\mathbf{r}'',\omega')\\ &n^{(1)}(\mathbf{r}''',\omega-\omega')+\frac{1}{2}\int d\mathbf{r}'d\mathbf{r}''d\omega'\chi_0^{(2)}(\mathbf{r},\mathbf{r}',\mathbf{r}'',\omega',\omega-\omega')\\ &\left[V_{ext}^{(1)}(\mathbf{r}',\omega')+\int d\mathbf{r}'''f_{uxc}(\mathbf{r}',\mathbf{r}''',\omega')n^{(1)}(\mathbf{r}''',\omega')\right]\\ &\left[V_{ext}^{(1)}(\mathbf{r}'',\omega-\omega')+\int d\mathbf{r}''''f_{uxc}(\mathbf{r}'',\mathbf{r}'''',\omega-\omega')n^{(1)}(\mathbf{r}'''',\omega-\omega')\right]\end{aligned} \tag{4.40}$$

With equation (4.16) and the definition of the second-order polarizability

$$n^{(2)}(\mathbf{r},\omega) = \frac{1}{2}\int d\mathbf{r}'d\mathbf{r}''d\omega'\chi^{(2)}(\mathbf{r},\mathbf{r}',\mathbf{r}'',\omega',\omega-\omega')V_{ext}^{(1)}(\mathbf{r}',\omega')V_{ext}^{(1)}(\mathbf{r}'',\omega-\omega') \tag{4.41}$$

we get the relation between $\chi^{(2)}$, $\chi_0^{(2)}$ and $\chi^{(1)}$

$$\begin{aligned}\chi^{(2)}(\mathbf{r},\mathbf{r}',\mathbf{r}'',\omega_1,\omega_2) = &\chi_0^{(2)}(\mathbf{r},\mathbf{r}',\mathbf{r}'',\omega_1,\omega_2)\\ &+\int d\mathbf{x}\,d\mathbf{x}'\,\chi_0^{(1)}(\mathbf{r},\mathbf{x},\omega_1+\omega_2)f_{uxc}(\mathbf{x},\mathbf{x}',\omega_1+\omega_2)\chi^{(2)}(\mathbf{x}',\mathbf{r}',\mathbf{r}'',\omega_1,\omega_2)\\ &+\int d\mathbf{x}\,d\mathbf{x}'\,d\mathbf{x}''\,\chi_0^{(1)}(\mathbf{r},\mathbf{x},\omega_1+\omega_2)g_{xc}(\mathbf{x},\mathbf{x}',\mathbf{x}'',\omega_1,\omega_2)\chi^{(1)}(\mathbf{x}',\mathbf{r}',\omega_1)\chi^{(1)}(\mathbf{x}'',\mathbf{r}'',\omega_2)\\ &+\int d\mathbf{x}\,d\mathbf{x}'\,\chi_0^{(2)}(\mathbf{r},\mathbf{x},\mathbf{r}'',\omega_1,\omega_2)f_{uxc}(\mathbf{x},\mathbf{x}',\omega_1)\chi^{(1)}(\mathbf{x}',\mathbf{r}',\omega_1)\\ &+\int d\mathbf{x}\,d\mathbf{x}'\,\chi_0^{(2)}(\mathbf{r},\mathbf{r}',\mathbf{x},\omega_1,\omega_2)f_{uxc}(\mathbf{x},\mathbf{x}',\omega_2)\chi^{(1)}(\mathbf{x}',\mathbf{r}'',\omega_2)\\ &+\int d\mathbf{x}\,d\mathbf{x}'\,\mathbf{x}''\,\mathbf{x}'''\,\chi_0^{(2)}(\mathbf{r},\mathbf{x},\mathbf{x}',\omega_1,\omega_2)f_{uxc}(\mathbf{x},\mathbf{x}'',\omega_1)f_{uxc}(\mathbf{x}',\mathbf{x}''',\omega_2)\chi^{(1)}(\mathbf{x}'',\mathbf{r}',\omega_1)\\ &\chi^{(1)}(\mathbf{x}''',\mathbf{r}'',\omega_2)\end{aligned} \tag{4.42}$$

This relation leads to a Dyson-like equation for the response functions, formally written as,

$$\begin{aligned}
&\Big[1-\chi_0^{(1)}(\omega_1+\omega_2)f_{uxc}(\omega_1+\omega_2)\Big]\chi^{(2)}(\omega_1,\omega_2) \\
&=\chi_0^{(2)}(\omega_1,\omega_2)\left[1+f_{uxc}(\omega_2)\chi^{(1)}(\omega_2)\right]\left[1+f_{uxc}(\omega_1)\chi^{(1)}(\omega_1)\right] \\
&\quad+\chi_0^{(1)}(\omega_1+\omega_2)g_{xc}(\omega_1,\omega_2)\chi^{(1)}\omega_1)\chi^{(1)}(\omega_2)
\end{aligned} \tag{4.43}$$

The second-order Dyson equation (4.43) and the calculation of the response function $\chi_0^{(2)}$ have been implemented in the code *2light* as described in ref ([26]). The spin-dependent derivation of Eq. (4.43) is one of the main point of this work and will be presented in Chapter 10.

4.3 Summary

In this chapter we have presented the main points of the time-dependent DFT. We have also shown how the Kohn-Sham equations can be solved in the framework of perturbation theory, using response functions. It appears that the accuracy of the TDDFT calculation depends on the xc kernels as they contain all the ingredients for the description of the excitonic interactions.

Chapter 5

GW approximation

Spectroscopic measurements are a tool of material characterization. Any spectroscopic method introduces perturbation into the system under study, propelling it into an excited state. Experimentally, the difficulty is to interpret the system's response correctly. However, from a theoretical standpoint, the difficulty is identifying (or creating) an appropriate, accurate, and, most importantly, computationally tractable method for describing the system's response. Many body Perturbation Theory (MBPT) offers a rigorous and systematic framework for describing a system's spectral characteristics by connecting essential quantities such as the Green's function, self-energy, and dielectric function described in this chapter. The poles of the Green's function for a single particle, the primary object in MBPT, are described in the section (5.1).

In electronic structure theory, the GW approximation(defined in section (5.4)) has become a widely used technique for predicting electronic excitation in chemical compounds and materials. The GW approximation can overcome many of the most notorious shortcomings of conventional density functionals, including the self-interaction error, the lack of long-range polarization effects, and the Kohn-Sham band-gap issue. The GW technique is well recognized for its ability to accurately predict the band gaps of solids, which will be addressed in this chapter.

5.1 Many Body Perturbation Theory Green's function method

The electronic Hamiltonian is composed of two components: the single-particle Hamiltonian $\hat{h}_0$, which is dependent on the coordinates of individual electrons, and the Coulomb interaction that couples two electrons coordinates together. In the electronic systems, the interaction between electrons is responsible for various phenomena such as finite lifetime and plasmonic excitations represented by additional energies in the spectra, which cannot be seen in the KS DFT independent particle approximation.

However, our efforts to solve an electronic system are hindered by the Coulomb interaction energy that occurs between electrons coordinates. In MBPT, the Coulomb interaction is introduced as an external perturbation to a non-interacting system. Green's function is used as the basic quantity to determine the electronic properties of materials in this theory.

Time ordered Green's function [27] is defined as follows,

$$
\begin{aligned}
G(1,2) &= -i\langle N|\mathcal{T}\left[\psi(1)\psi^{\dagger}(2)\right]|N\rangle \\
&= \begin{cases} -i\langle N|\psi(1)\psi^{\dagger}(2)|N\rangle t_1 > t_2 \\ \;\; i\langle N|\psi^{\dagger}(2)\psi(1)|N\rangle t_1 < t_2 \end{cases}
\end{aligned}
\tag{5.1}
$$

Where ψ and $\psi^{\dagger}$ are the field operators, $\mathcal{T}$ is the time order operator and, $|N>$ is the N electrons many body state. Here, we use the compact notation $1 = (r_1, \sigma_1, t_1)$ for a space, spin, time argument.
G is described as a propagator that describes the probability of an amplitude changing when a particle propagates from one place to another.

In frequency space, G is written as the follows,

$$
\begin{aligned}
G(x,x')(\omega) = \sum_s \Bigg[& \frac{\langle N\hat{\psi}^{\dagger}(x')\,|N-1\rangle_s\,\langle N-1|_s\,\hat{\psi}(x)N\rangle}{\omega-(E_0^N-E_s^{N-1})-i\eta} \\
& + \frac{\langle N|\hat{\psi}(x)\,|N+1\rangle_s\,\langle N+1|_s\hat{\psi}^{\dagger}(x')|N|\rangle}{\omega-(E_s^{N+1}-E_0^N)+i\eta} \Bigg]
\end{aligned}
\tag{5.2}
$$

Where $\sum_s$ is the total number of potential states. Its poles indicate the difference in energies between the N and $N \pm 1$ electron systems, which is equal to the energies obtained from photoemission and inverse photoemission experiments used to construct the band structure of materials. Thus, the one-body Green's function can be used to obtain band structure and, consequently, gap energies for materials.

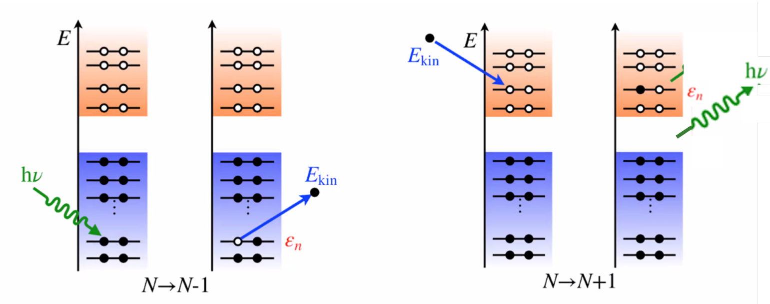

Figure 5.1: Photoemission and inverse-photoemission experiments

5.2 Equation of motion for the one-body Green's function

In condensed matter electronic structure theory, we avoid calculating the many body wave function; instead, we use the equation of motion to get the one-body Green's function. Then, in order to formulate the equation of motion, we begin by propagating in time the time-ordered Green's function stated in the equation (5.1).

$$\frac{\partial}{\partial t}G(1,2) = \frac{\partial}{\partial t}\Big[-i\langle N|\mathcal{T}\big[\psi(1)\psi^\dagger(2)\big]|N\rangle \Big] \tag{5.3}$$

Using Heisenberg equation of motion for the field operator,

$$i\frac{\partial \psi}{\partial t} = [\psi, H] \tag{5.4}$$

The equation of motion of the Green function has been derived [27], which contains the two particle Green's function due to the two body coulomb interaction operator, according to an infinite sequence of higher-order Green's function. Thus, the difficulty is how to avoid this coupled equation, which cannot be solved mathematically. This is where the MBPT concept is discussed, based on the approximation of where we apply a time-dependent external perturbation $v_{ext}(t)$. to the system.

The total Hamiltonian without external perturbation consists of,

$$\begin{aligned}\hat{H} = -\frac{1}{2}\int d\mathbf{r}\psi^\dagger(\mathbf{r})\nabla^2\psi(\mathbf{r}) + \int d\mathbf{r}\psi^\dagger(\mathbf{r})V_{ext}(\mathbf{r})\psi(\mathbf{r}) + \\ \frac{1}{2}\int d\mathbf{r}d\mathbf{r}'\psi^\dagger(\mathbf{r})\psi^\dagger(\mathbf{r}')v(\mathbf{r},\mathbf{r}')\psi(\mathbf{r}')\psi(\mathbf{r})\end{aligned} \tag{5.5}$$

and the interaction Hamiltonian is,

$$\hat{H}'(t) = \int drdr'\hat{\psi}^\dagger(r)v_{ext}(r,r',t)\hat{\psi}(r') \tag{5.6}$$

So the total Hamiltonian becomes,

$$\hat{H}_{Total} = \hat{H} + \hat{H}'(t) \tag{5.7}$$

The Green's function has the following definition in such system (system with external perturbation),

$$G(x,t;x',t') = -i\frac{\langle N|\hat{T}[\hat{S}\hat{\psi}(x,t)\hat{\psi}^\dagger(x',t')]|N\rangle}{\langle N|\hat{T}[\hat{S}]|N\rangle} \tag{5.8}$$

where $\hat{S}$ is the operator that transforms the system from its ground state to an excited state.

$$\hat{S} = e^{\left(-i\int_{-\infty}^{+\infty} dt\hat{H}_I'(t)\right)} \tag{5.9}$$

The variation of the one-body Green's function, with respect to the external perturbation, yields to the very useful relation,

$$\frac{\delta G}{\delta v_{ext}} = GG - G_2 \tag{5.10}$$

where G_2 is the two particle Green's function. We can now compute the two-body green's function in terms of the one-body green's function using equation (5.10), which solves the previously described issue of coupled equation.

This will lead us to the well-known equation of motion, which includes the self-energy associated with exchange-correlation, given by,

$$\left[i\frac{\partial}{\partial t_1} - H_0(1)\right]G(1,2) - \int d3\Sigma(1,3)G(3,2) = \delta(1,2) \tag{5.11}$$

where

$$H_0(1) = -\frac{1}{2}\nabla_1^2 + V_{ext}(1) + V_H(1) \tag{5.12}$$

and Σ is referred to as the exchange-correlation self-energy, which plays the key role here and whose mathematical formulation is well known and given by,

$$\Sigma(1,2) = -i\int d(34)V(1^+,3)G(1,4)\frac{\delta G^{-1}(4,2)}{\delta v_{ext}(3)} \tag{5.13}$$

where $1^+ = (r_1, \sigma_1, t_1 + \delta)$ where δ is positive infinitesimal.

Σ_{xc} contains all the many body quantum effect of the electronic system that influences the propagation of an electron in the system.

The condition $\Sigma_{xc} = 0$ defines a similar equation to for the non-interacting (it still contains the Hartree potential(V_H)) Green function G^0

$$\left[i\frac{\partial}{\partial t_1} - H_0(1)\right]G^0(1,2) = \delta(1,2) \tag{5.14}$$

From equation (5.11) and (5.14) we have

$$G(1,2) = G^0(1,2) + \int d(34)G^0(1,3)\Sigma_{xc}(3,4)G(4,2) \tag{5.15}$$

which represents the Dyson [28,29] equation for the Green function.

5.3 Hedin's equations

In electronic systems, screening is essential when two charges interact via the dressed Coulomb interaction W, commonly referred to as a screened Coulomb interaction, which means that the interaction between two charges is modified by the rearrangement of the other charges, generally to the detriment of the interaction (often but not always). As a result, Hedin attempted [30,31] to construct the equations(given below) in such a manner that W is clearly stated.

$$\Sigma_{xc}(1,2) = i\int d(34)G(1,3)\Gamma(3,2,4)W\big(4,1^+\big) \tag{5.16}$$

$$G(1,2) = G^0(1,2) + \int d(34)G^0(1,3)\Sigma_{xc}(3,4)G(4,2) \tag{5.17}$$

$$\Gamma(1,2,3) = \delta(1,2)\delta(1,3) + \int d(4567)\frac{\delta\Sigma_{xc}(1,2)}{\delta G(4,5)}G(4,6)G(7,5)\Gamma(6,7,3) \tag{5.18}$$

$$W(1,2) = v(1,2) + \int d(34)v(1,3)P(3,4)W(4,2) \tag{5.19}$$

$$P(1,2) = -i \int d(34) G(1,3) G\left(4,1^{+}\right) \Gamma(3,4,2) \tag{5.20}$$

Fig. 5.2 illustrates the Hedin's pentagon. It is a set of five coupled integral equations, which should in principle be solved iteratively. However, in practice, it is not feasible, and it relies on the so-called GW approximation.

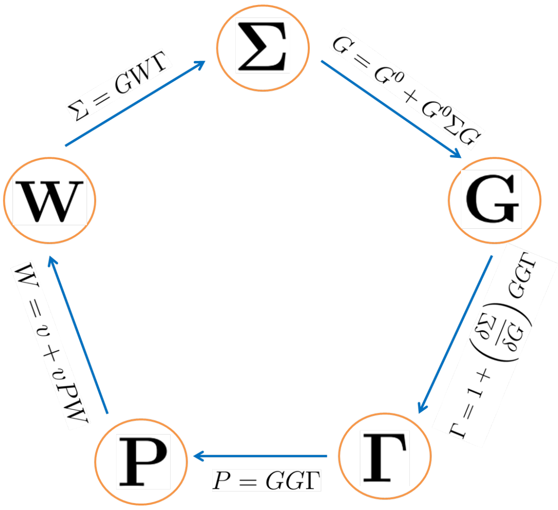

Figure 5.2: Hedin's Pentagon

5.4 GW approximation

As previously stated, Hedin's Pentagon is the method for calculating self-energy. In practice, the self-energy may be calculated using the GW approximation (GWA) [32]. The method for calculating self-energy is detailed below,

1. Assuming that $\Sigma_{xc} = 0$, the green function will be $G = G_0$, i.e the independent particle Green's function.

2. In this approximation the vertex function Γ set to a delta function, which can be represented as,

   $$\Gamma^{GWA}(1,2,3) = \delta(1,2)\delta(1,3) \tag{5.21}$$

   As a result, $\Gamma = 1$ is taken as a starting point.

3. This approximated vertex yields to the Random Phase Approximation (RPA) for P, which is defined by the figure (5.3b). where,

   $$P^0(1,2) = -iG^0(1,2)G^0\left(2,1^{+}\right) \tag{5.22}$$

   is called as RPA polarizability.

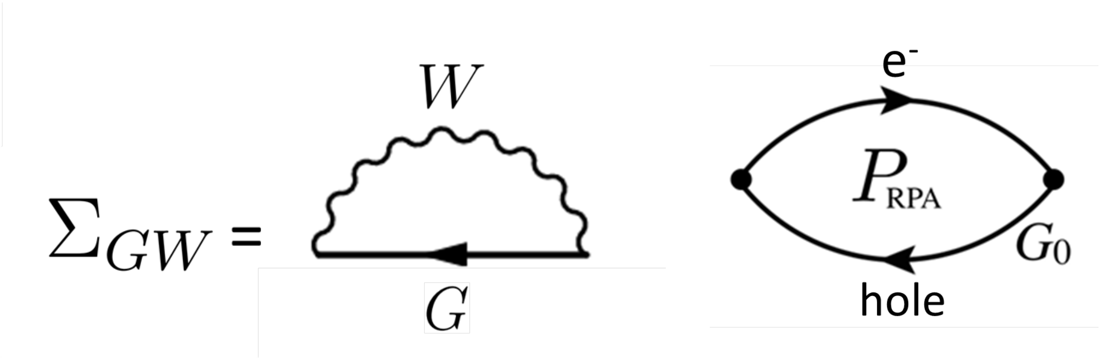

(a) GW approximation for the exchange-correlation self-energy (b) Random Phase Approximation for P

Figure 5.3: GW approximation

4. Using P^0, we can calculate screening W^0 which is,

$$W^0(1,2) = v(1,2) + \int d(34)v\left(1^+,3\right)P^0(3,4)W^0(4,2) \tag{5.23}$$

5. Then further we calculate the self-energy $\Sigma_{xc}^{GW} = G^0W^0$,which is represented by the figure (5.3a can be used to calculate the quasiparticle energies.

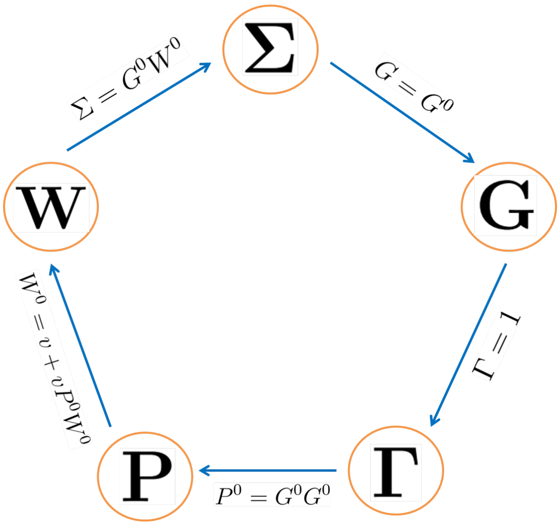

Figure 5.4: G^0W^0 approximation

The GW approximation for self-energy is very efficient because it captures a screening correlation. Thus, GW works effectively for many materials where screening is critical, and electrons are weakly to moderately correlated but fail to represent highly correlated systems. The GWA described in figure (5.4) is widely used in condensed matter physics [27] and became a standard calculation of quasiparticle band structure and band gap for materials.

5.5 Band gap within GW approximation

From the GW approximation for the self-energy we can calculate the Green's function using equation (5.17). The poles of Green's function represent the quasiparticle energies and the plasmonic excitation. Using the quasiparticle energies, we can calculate the band gap. In the next section, we will see how to calculate the quasiparticle energies using Green's function.

5.5.1 Quasiparticle energies from Green's function

The quasiparticle enery is the energy of a non-interacting particles modified by the effect of the other particles in the system, contained in the self-energy and especially in the real part of Σ_{xc}. A formalism based on the Green's function can be used to calculate the quasiparticle energies. The inverse of the Green's function can be written as,

$$G^{-1} = (G^0)^{-1} - \Sigma \tag{5.24}$$

where $\Sigma = \Sigma_H + \Sigma_{xc}$. Σ_H is the Hartree self-energy and Σ_{xc} is the exchange-correlation self-energy and G^0 is defined by non-interacting equation,

$$G = \frac{1}{(G^0)^{-1} - \Sigma} \tag{5.25}$$

Using $(G^0)^{-1} = \omega - E - i\eta$ (the removal part for instance), we can write the Green's function as,

$$G = \frac{1}{\omega - E - i\eta - \Sigma} \tag{5.26}$$

where Σ is the complex quantity and we can write it as $\Sigma = Re(\Sigma) + iIm(\Sigma)$ and hence the above equation becomes,

$$G = \frac{1}{\omega - E - i\eta - (Re(\Sigma) + iIm(\Sigma))} \tag{5.27}$$

where G can be also simplified as,

$$G = \frac{(\omega - E - Re(\Sigma)) - i\eta(\eta + Im(\Sigma))}{(\omega - E - Re(\Sigma))^2 + (\eta + Im(\Sigma))^2} \tag{5.28}$$

It shows that the imaginary part of the Green's function,known as the spectral function, has poles at the quasiparticle energies and can be written as,

$$A = (\frac{1}{\pi})\frac{(\eta + Im(\Sigma))}{(\omega - E - Re(\Sigma))^2 + (\eta + Im(\Sigma))^2} \tag{5.29}$$

The spectral function is used to compute the quasiparticle energies. The spectral function has a pole at $\omega = E - Re(\Sigma)$. This gives us the quasiparticle energies. If we use $E = E_a^{KS}$, the KS energies, then we can write the quasiparticle energies $E_a = E_a^{KS} + Re(\Sigma_{xc}) - v_a^{xc}$. Where v_a^{xc} is the KS exchange-correlation potential [27].

5.6 Quasiparticle energies using Kohn-Sham equations

The GW approximation given above is useful for obtaining accurate values of excitation energies and quasiparticle band gaps in solids.

G_0W_0 calculations are usually performed on top of KS-DFT or HF calculations. A flowchart for a typical G_0W_0 calculation starting from a KS-DFT Hamiltonian is shown in figure (5.5) and illustrated as below,

1. Figure starts with the KS energies $\left\{E_a^{\mathrm{KS}}\right\}$, KS orbitals $\left\{\phi_a^{\mathrm{KS}}\right\}$ and the exchange-correlation potential V_{xc} from a DFT calculation. The exchange part of the self-energy Σ_a^x is directly computed from the DFT orbitals.
2. For the correlation term Σ_a^c, the frequency integral over G_0 (or G^0)and W_0 (or W^0) must be computed. If the integral is evaluated numerically, W_0 is computed for a set of frequencies $\{\omega\}$. The procedure to obtain W_0 is as follows: First, the irreducible polarizability (χ_0) is computed with the KS energies and orbitals. Then the dielectric function (ε) is calculated using (χ_0). Using the ε and the bare Coulomb interaction v, we finally obtain the correlation part of the screened Coulomb interaction, represented by W_0^c in the flow chart.
3. Now, an iterative procedure is required. More precisely, the correlation term of the self-energy depends on E_a and must be updated at each step. Note that only G_0 is a function of the QP energies, while W_0^c depends solely on the frequencies of the integration grid. Therefore, W_0^c can be precomputed before entering the QP cycle, as shown in the picture (5.5)
4. The correlation self-energy Σ_a^c is a complex quantity. However, the imaginary part of Σ_a^c is generally small for frequencies around the QP energies,

5.7 Scissor operator approximation

The band gap problem in DFT is well-known and has been attributed as the primary reason for often insufficient agreement between experimental and LDA-derived dielectric tensor functions. A very accurate solution is the computation of the GW bandgap for all bands and all k-points. However, due to the numerical complexity of the GW calculation, this is a difficult task. A simple approximation has been proposed, the scissor operator approximation, by Levine, Allan(133) and Gonze and Lee [81], and gives very satisfactory results for solving this issue.

It is based on the following observation for semiconductors: after a GW calculation, the valence bands are not strongly modified, while the low conduction bands are shifted upwards, keeping the same shape. The scissor approximation assumes that using only shifted values for the energy of the conduction bands in the construction of the KS response function is enough to account for the GW corrections in many situations. This constant value Δ is called the scissor value and is added to the conduction band energies E_g^{LDA}.

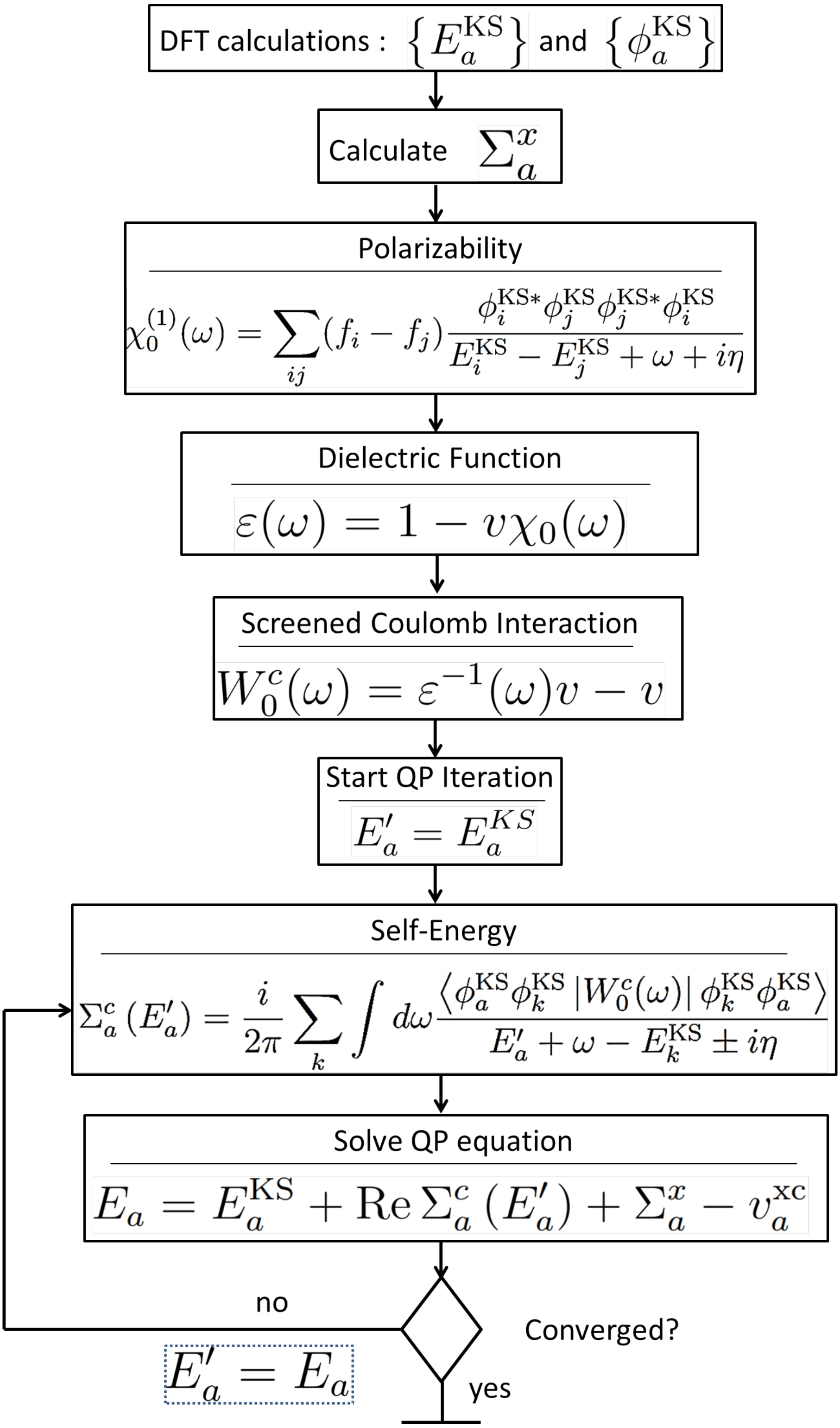

Figure 5.5: Flow chart of G^0W^0 calculation starting from the KS-DFT calculation

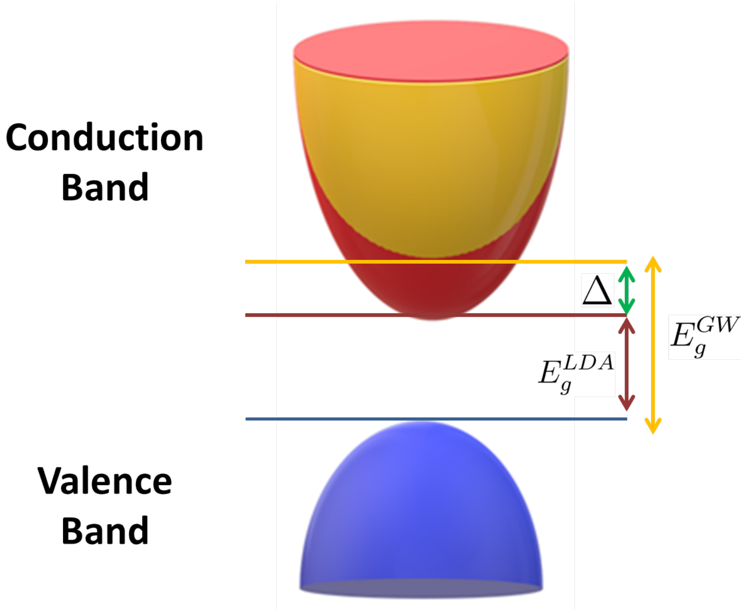

Figure 5.6: Scissor operator approximation

This approximation is straightforward to implement. The scissor operator approximation is described by image (5.6). It requires only the calculation of the GW corrections for the band gap. The value of the scissor is then usually obtained as the difference between the GW band gap and the LDA band gap. It can also be taken as the difference between the experimental band gap, if available, and the LDA band gap.

5.8 Summary

In this chapter, we discussed Green's function in the context of MBPT. Equation of motion of the one-body Green's function, which leads to the Dyson equation for Green's function, has been discussed. Additionally, the set of self-consistent coupled equations was addressed. There has been discussion about the GW approximation to self-energy. It was described how to calculate the band gap using the GW approximation. It has been explained how to determine the quasiparticle energy beginning from the KS. Additionally, the scissor approximation was explained.

Chapter 6

Bethe Salpeter Equation

Bethe Salpeter Equation (BSE) is another method for calculating the absorption spectra. BSE comes within the context of the Many Body Perturbation Theory. When the system is excited by an external perturbation, such as light, bound excitons, or electron-hole pairs, are detected. Certain material properties, such as bound excitons, are not described by the TDDFT owing to the lack of a good approximation for the exchange-correlation kernel.

The BSE is effective in capturing these kinds of characteristics. In this chapter, we will briefly describe the BSE.

6.1 Bethe Salpeter Equation for the response function

Whenever we think about light absorption, we are particularly interested in neutral excitations, which do not alter the overall charge of the system. When light is incident on the material, an electron moves from the valence band to the conduction band and leaves a hole behind. In the presence of interaction, a hole and an electron (an exciton pair) interact with the rest of the system and each other. Their propagation is given by the two particles Green's function. Therefore, it is crucial for the absorption to study the two particles Green's function.

Formally, the two particle correlation function (L) can be written in terms of Green's function as [27, 33],

$$L(1,2,3,4) = -i\frac{\delta G(1,3)}{\delta V_{ext}(4,2)} = -i\int d(5)\frac{\delta G(1,5)}{\delta V_{ext}(4,2)}\delta(5,3) \tag{6.1}$$

The Green's function and its inverse is defined by:

$$\int d(6) G^{-1}(5,6)G(6,3) = \delta(5,3) \tag{6.2}$$

using equation (6.2) in equation (6.1), L can be written as,

$$L(1,2,3,4) = i\int d(56)\frac{\delta G(1,5)}{\delta V_{ext}(4,2)}G^{-1}(5,6)G(6,3) \tag{6.3}$$

and,

$$\int d(56)\frac{\delta G(1,5)}{\delta V_{ext}(4,2)}G^{-1}(5,6)G(6,3)=\int d(56)G(1,5)G(6,3)\frac{\delta G^{-1}(5,6)}{\delta V_{ext}(4,2)} \tag{6.4}$$

and hence,

$$L(1,2,3,4)=i\int d(56)G(1,5)G(6,3)\frac{\delta G^{-1}(5,6)}{\delta V_{ext}(4,2)} \tag{6.5}$$

Where,

$$G^{-1}(5,6)=(i\frac{\partial}{\partial t}+\nabla^2/2)\delta(5,6)-V_{ext}(5,6)+V_H(5)\delta(5,6)-\Sigma_{xc}(5,6) \tag{6.6}$$

Using equation (6.6) in equation (6.1),

$$L(1,2,3,4)=i\int d(56)G(1,5)G(6,3)\Big[-\frac{\delta V_{ext}(5,6)}{\delta V_{ext}(4,2)}-\frac{\delta V_H(5)}{\delta V_{ext}(4,2)}\delta(5,6) -\frac{\delta\Sigma_{xc}(5,6)}{\delta V_{ext}(4,2)}\Big] \tag{6.7}$$

$$L(1,2,3,4)=L_0(1,2,3,4)-i\int d(56)G(1,5)G(6,3)\Big[\frac{\delta V_H(5)}{\delta V_{ext}(4,2)}\delta(5,6)+ \frac{\delta\Sigma_{xc}(5,6)}{\delta V_{ext}(4,2)}\Big] \tag{6.8}$$

$$L(1,2,3,4)=L_0(1,2,3,4)-i\int d(5678)G(1,5)G(6,3)\Big[\frac{\delta V_H(5)}{\delta G(7,8)}\frac{\delta G(7,8)}{\delta V_{ext}(4,2)}\delta(5,6) +\frac{\delta\Sigma_{xc}(5,6)}{\delta G(7,8)}\frac{\delta G(7,8)}{\delta V_{ext}(4,2)}\Big] \tag{6.9}$$

This leads to the Dyson like equation [32] for the polarizability L,

$$L(1,2,3,4)=L_0(1,2,3,4)+\int d(5678)L_0(1,6,3,5)K(5,7,6,8)L(8,2,7,4) \tag{6.10}$$

The equation (6.10) is known as the Bethe Salpeter Equation for the response function.

where the kernels K can be defined as,

$$K(5,6,7,8)=\delta(5,6)\delta(7,8)v(5,7)+i\Xi(5,6,7,8) \tag{6.11}$$

with the kernel $\Xi(5,6,7,8)$ representing an effective two-particle interaction defined as,

$$\Xi(5,6,7,8)=\frac{\delta\Sigma(6,5)}{\delta G(7,8)} \tag{6.12}$$

As mentioned in (6.11), the kernel K is comprised of two terms: the first component is the Coulomb interaction v, also known as an electron-hole exchange, and the second term Ξ which is defined by equation (6.12) is the variation of the self-energy due to the Green function variation.

The independent-electron-hole polarizability,

$$L^0(1,2,3,4) = iG(1,3)G(4,2) \tag{6.13}$$

L^0 describes the propagation of a hole and an electron separately and also the two-particle correlation function in the absence of interaction between the two particles.

The four point density correlation functional L can be written using the two particle Green's function,

$$L(1,2,3,4) = L^0(1,2,3,4) - G(1,2,3,4) \tag{6.14}$$

where the two particle green function can be defined as,

$$G(1,2,3,4) = (-i)^2\langle N|T\left[\psi(1)\psi(3)\psi^\dagger(4)\psi^\dagger(2)\right]|N\rangle \tag{6.15}$$

6.1.1 RPA approximation

In this approximation, we consider that Ξ=0. The only term remaining is the electron-hole exchange term computed using the Coulomb interaction. Note that without Ξ, BSE reduces to the Time-dependent Hartree-Fock approximation.

6.1.2 GW approximation

To solve the equation 6.10 we must know Ξ. To calculate the Ξ we should know the self-energy (Σ). The self-energy may be defined using the GW Approximation as $\Sigma = iG(1,2)W(2,1)$. This directly leads to,

$$K(1,2,3,4) = \delta(1,2)\delta(3,4)\bar{v}(1,3) - \delta(1,3)\delta(2,4)W(1,2) \tag{6.16}$$

Where in the derivation of the self-energy, we have omitted the term $iG(1,2)\frac{\delta W(1,2)}{\delta G(3,4)}$, i.e. the variation of the screening due to the excitation.

6.1.3 Macroscopic dielectric function

The absorption coefficients of a material can be obtained from χ, the density-density response function. The χ can be written in terms of L as,

$$\chi(\mathbf{r}_1,\mathbf{r}_2;t_1-t_2) = -iL(\mathbf{r}_1,t_1,\mathbf{r}_1,t_1,\mathbf{r}_2,t_2,\mathbf{r}_2,t_2) \tag{6.17}$$

and hence the macroscopic dielectric function [34] can be written in terms of L as,

$$\varepsilon_M(\omega) = 1 - \lim_{\mathbf{q}\to 0} v(\mathbf{q}) \int d\mathbf{r}d\mathbf{r}' e^{i\mathbf{q}\cdot(\mathbf{r}-\mathbf{r}')} L(\mathbf{r},\mathbf{r},\mathbf{r}',\mathbf{r}',\omega) \tag{6.18}$$

The imaginary part of the dielectric function as defined by 6.18 gives the absorption spectrum.

6.1.4 Two particle Hamiltonian

As a further approximation, the quasiparticle approximation is often used for G (5.4) in L_0, and the frequency dependency of W in the kernel of the BSE is omitted. In equilibrium, L is then dependent on a single time difference or frequency after Fourier transformation. Rather than calculating the BSE for each frequency, the resultant equation may be rewritten as an eigenvalue problem with an effective electron-hole Hamiltonian H_{exc}, where v_c and W represent effective electron-hole interactions [35–38], respectively. The Hamiltonian is usually expressed in the basis of pair of orbitals as,

$$H_{exc}(n_1, n_2, n_3, n_4) = [E^{QP}_{n_2} - E^{QP}_{n_1}]\delta_{n_1 n_3}\delta_{n_2 n_4} - W^{n_1 n_3}_{n_2 n_4} + \bar{v}^{n_1 n_2}_{n_3 n_4} \tag{6.19}$$

and

$$\begin{aligned} \bar{v}^{n_1 n_2}_{n_3 n_4} = \langle n_1 n_2 | v_c | n_3 n_4 \rangle = 2 \textstyle\int d\mathbf{r} d\mathbf{r}' \phi^*_{n_2}(\mathbf{r})\phi_{n_1}(\mathbf{r}) v_c(\mathbf{r}, \mathbf{r}') \\ \phi_{n_4}(\mathbf{r}')\phi^*_{n_3}(\mathbf{r}') \end{aligned} \tag{6.20}$$

$$\begin{aligned} W^{n_1 n_3}_{n_2 n_4} = \langle n_1 n_2 | W | n_3 n_4 \rangle = \textstyle\int d\mathbf{r} d\mathbf{r}' \phi^*_{n_2}(\mathbf{r})\phi_{n_4}(\mathbf{r}) W(\mathbf{r}, \mathbf{r}') \\ \phi_{n_1}(\mathbf{r}')\phi^*_{n_3}(\mathbf{r}') \end{aligned} \tag{6.21}$$

Where n denotes the bands, and the ϕ's are the KS wave-functions. Here, we have omitted the index k, associated with each vertical transition vk → ck. As a result, the basis is composed of resonant (valence band to conduction band) and antiresonant transitions (Conduction band to Valence band), and H_{exc} takes the form of a block matrix.

$$H_{\text{exc}} = \begin{pmatrix} R & K^{R,A} \\ K^{A,R} & A \end{pmatrix} \tag{6.22}$$

With the resonant matrix R, the anti-resonant A, and the coupling elements K. The diagonal blocks A and R are hermitian, and the coupling blocks K are symmetric. We can write the polarizability using the above equation as,

$$L_{(n_1 n_2)(n_3 n_4)} = \left[H^{2p} - I\omega\right]^{-1}_{(n_1 n_2)(n_3 n_4)} (f_{n_3} - f_{n_4}) \tag{6.23}$$

At each frequency, the issue of inverting a matrix has been projected onto the challenge of diagonalizing that matrix once and for all. As,

$$H_{exc}(n_1, n_2, n_3, n_4) A_\lambda(n_3, n_4) = E^{exc}_\lambda A_\lambda(n_1, n_2) \tag{6.24}$$

We can calculate the spectral function($\{A_\lambda\}$) and energy ($\{E_\lambda\}$) from the diagonalization.

The $\{A_\lambda\}$ and $\{E_\lambda\}$, are used to build the polarizability function in the transition framework as shown below,

$$L_{(n_1 n_2)(n_3 n_4)} = \sum_{\lambda, \lambda'} \frac{A^{(n_1 n_2)}_\lambda S^{-1}_{\lambda\lambda'} A^{*(n_3 n_4)}_{\lambda'}}{E^{exc}_\lambda - \omega} \tag{6.25}$$

where S is the overlap matrix. using equation in equation 6.18 gives,

$$\varepsilon_M(\omega) = 1 - \lim_{\mathbf{q}\to 0} v_0(\mathbf{q}) \sum_{\lambda\lambda'} \Bigg[\sum_{(n_1 n_2)} \left\langle n_1 \middle| e^{-i\mathbf{q}\cdot\mathbf{r}} \middle| n_2 \right\rangle \frac{A_\lambda^{(n_1 n_2)}}{E_\lambda^{exc} - \omega - i\eta} \times \\ \times \mathrm{S}^{-1}_{\lambda\lambda'} \sum_{(n_3 n_4)} \left\langle n_4 \middle| e^{i\mathbf{q}\cdot\mathbf{r}'} \middle| n_3 \right\rangle A_\lambda^{*(n_3 n_4)} (f_{n_4} - f_{n_3}) \Bigg] \tag{6.26}$$

Within the Tamm-Dancoff approximation (TDA) [39, 40], the coupling terms are omitted. Assuming that we are only concerned with the resonant component of the excitonic Hamiltonian(H_{exc}^{reso}), i.e., the portion that contains only positive frequency transitions, it can be written as,

$$R = H_{exc}^{reso}(ck, vk, c^{'}k^{'}, v^{'}k^{'}) = [E_c^{QP}(k) - E_v^{QP}(k)]\delta_{cc'}\delta_{vv'}\delta_{kk'} - W^{kk'}_{\substack{cc'\\vv'}} + 2\bar{v}^{kk'}_{\substack{cv\\c'v'}} \tag{6.27}$$

where the energy $[E_c^{QP}(k) - E_v^{QP}(k)]$ is the difference between an unoccupied and an occupied quasiparticle state, calculated in the GWA (described in the section (5.4)).

In this case, the eigenstates A_λ are mutually orthogonal if H_{exc}^{reso} is Hermitian; the dielectric function can simply be written as,

$$\varepsilon_M(\omega) = 1 - \lim_{\mathbf{q}\to 0} v_0(\mathbf{q}) \sum_{\lambda} \frac{\left| \sum_{(n_1 n_2)} \langle n_1 | e^{-i\mathbf{q}\cdot\mathbf{r}} | n_2 \rangle A_\lambda^{(n_1 n_2)} \right|^2}{E_\lambda^{exc} - \omega - i\eta} \tag{6.28}$$

6.2 BSE calculations starting from the DFT

The general procedure to account for many body effects in optical spectra consists of three steps (as shown in figure (6.1)) [32]

- Preparation of a starting electronic, i.e. DFT, in which neutral pair excitation occurs in an electronic structure that comprises xc but does not contain the excitation aspect structure.

- An improvement due to quasiparticle effects, i.e. GWA, in which the excitation of a pair of neutral quasiparticles occurs in an electronic structure that includes the excitation aspect.

- The inclusion of electron-hole attraction and exchange, i.e. BSE, it includes not only the quasiparticle nature of the individual electron and hole, but also their screened and unscreened Coulomb correlations.

Their combination produces novel quasiparticles known as excitons.

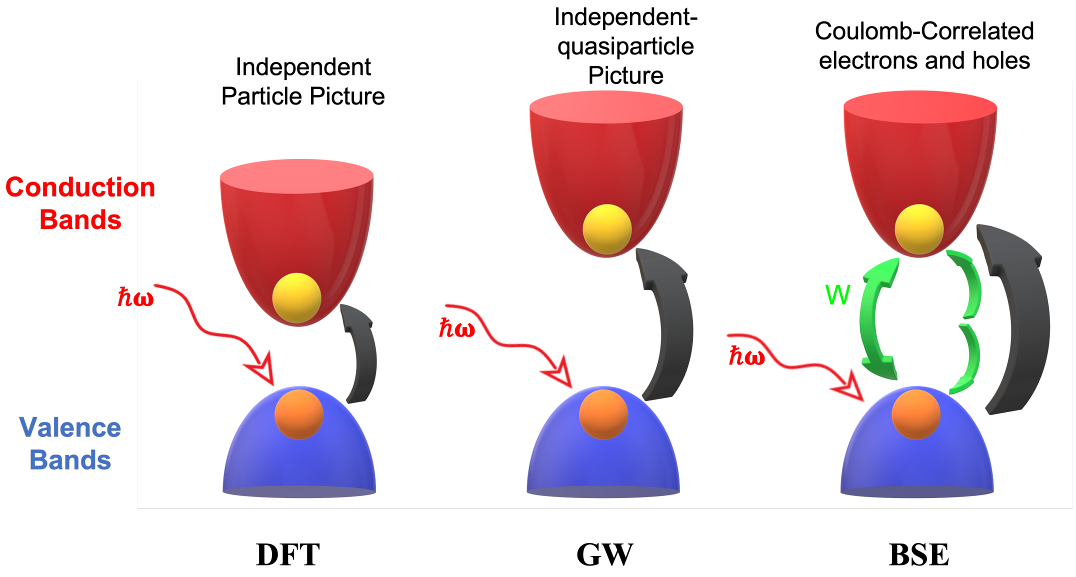

Figure 6.1: BSE starting from DFT

6.3 Summary

This chapter discussed the two particle response function, which can be calculated using two particle Green's function. Further, the two particles Hamiltonian has been discussed. Then the eigenvalues and eigenfunction of these two particles resonant Hamiltonian are used to calculate the macroscopic dielectric function.

Part II

Development and Application

Chapter 7

Electronic properties of Cr_2O_3

First, the ground state calculation for the AFM Cr_2O_3 has been performed. In the ground state calculation, we calculated the band gap and the bandstructure of the AFM Cr_2O_3 using the DFT approach. Further, we studied the GW band gap of the Cr_2O_3 using valence electrons pseudopotential and using semicore electrons pseudopotential.

The effect of the semicore electrons of Cr on the GW band gap has been discussed. Finally, we compared the calculated band gap using GW to the experimental band gap and the previously calculated band gap theoretically.

7.1 Antiferromagentic Cr_2O_3 structure

Cr_2O_3 is the most stable magnetic-dielectric oxide material [41]. Furthermore, bulk Cr_2O_3 is an antiferromagnet at temperatures below the Neel temperature of 308K [42]. Cr_2O_3 is a corundum crystal with a space group of R3c, with O atoms organized in hexagonal close-packed (001) layers and Cr atoms occupying two-thirds of the octahedral spaces between as shown in the figure (7.1).

Cr_2O_3 has three different magnetic structures : AF1$(+-+-)$, AF2$(++--)$, and AF3$(+--+)$. The stable phase is AF1, which has a magnetic structure corresponding to a $(+-+-)$ or $(\uparrow\downarrow\uparrow\downarrow)$ spin sequence on the Cr atoms along the threefold axis, where the symmetry reduces to R3c. It is also possible to have a second antiferromagnetic configuration (AF2) with the $(++--)$ or $(\uparrow\uparrow\downarrow\downarrow)$ spin sequence. The next structure AF3 has a $(+--+)$ or $(\uparrow\downarrow\downarrow\uparrow)$ spin sequence.

In all three instances, the primitive unit cell contains two independent metal atoms denoted by Cr $(\uparrow)$ and Cr$(\downarrow)$ as shown in (7.1).

The most stable structure is the AF1 structure, which we will study in detail in this chapter. In cases where the structural type is not mentioned throughout the manuscript, it is inferred that the AF1 structure is used.

7.2 Ground state properties of Cr_2O_3

The first step towards the calculation of various properties of the Cr_2O_3 using the ab-initio (or first principles) approach is the calculation of ground state properties using DFT.

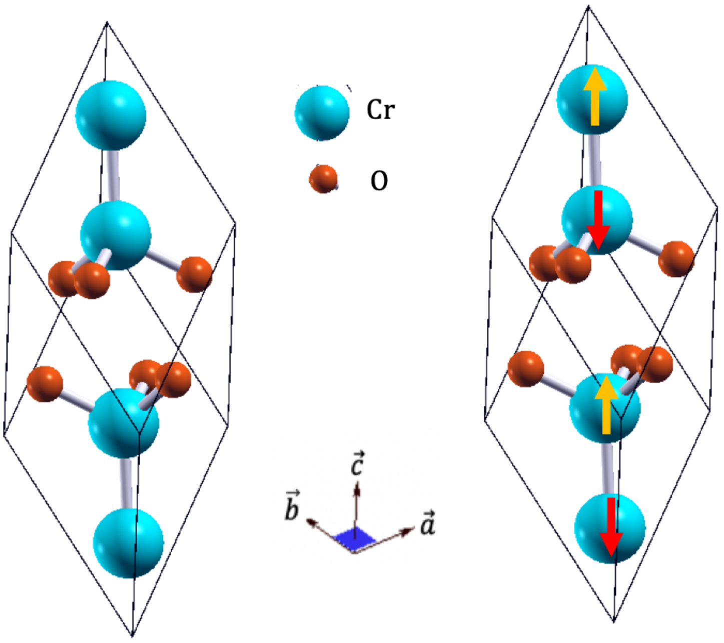

Figure 7.1: Structure of Cr_2O_3

Among the various ground state properties, we will discuss the most crucial properties, which is band gap and bandstructure of the Cr_2O_3. We will also calculate the ground state density and DFT orbitals.

7.2.1 Calculation details

A first principle study of the electronic structure of Cr_2O_3 is carried out within the framework of planewave pseudopotential density functional theory (DFT).

All DFT calculations are performed using the Abinit code [43]. Unless otherwise specified, all calculations are done using the local spin density approximation (LSDA) for the exchange-correlation potential used in DFT. The spin-polarization is included in the calculations through LSDA.

In the calculations, two distinct pseudopotentials have been used. The first one is a valence electrons pseudopotential, which implies that we considered the pseudopotential for Cr with six electrons in the valence, namely $4s^1$, $3d^5$. In this case, the total number of electrons is 60.

The second one is the pseudopotential with semicore electrons, where we considered the pseudopotential for Cr with six valence electrons, namely $4s^1$, $3d^5$, and extra semicore $3s^2$,$3p^6$ electrons acting as valence electrons. In this case, the total number of electrons is 92.

Structure relaxation

The first step in the calculation is structure relaxation. This ensures that the initial crystalline structure is completely relaxed and optimized (within specific approximate tolerance requirements that are monitored), allowing for correct and realistic property calculations to be performed on it throughout the rest of the procedure.

"Structure relaxation" refers to the process of methodically allowing the material's unit cell to experience a series of successive modest structural modifications in terms of its lattice parameters and atomic position. This results in an effective sampling of the material's free energy landscape, which the crystal structure configuration can traverse (except for significant energy barriers), and can thus be fully optimized by the time the calculation is terminated according to the various thresholds criteria outlined below.

- Equilibrium condition on the internal stress tensor. By optimized (or relaxed) crystal structure, it is typically intended that the internal stress tensor components of the material should match the externally applied pressure as precisely as possible, which corresponds to the ambient atmospheric pressure for material at equilibrium conditions.

- Equilibrium condition on the inter-atomic forces. A relaxation calculation guarantees that the interatomic forces inside the crystal structure are similarly reduced to negligible levels.

Together with the previously described pressure criteria, this feature helps the overall structure to remain as stable as possible and minimize the potential energy.

All geometry relaxations are performed using a 4×4×4 k-point mesh to force tolerance of less than 10^{-6} Rydberg/Bohr per unit cell, resulting in highly converged crystal structures.

As a result, the converged value of lattice constant for AF1 Cr_2O_3 is 10.18 Bohr. The converged value of the angle is 55.13°. The reduced coordinate of the atoms which we used in our calculations is given below:

Atom	Reduced coordinates
Cr	0.1525 0.1525 0.1525
Cr	0.3475 0.3475 0.3475
Cr	0.6525 0.6525 0.6525
Cr	0.8475 0.8475 0.8475
O	0.2500 0.5560 0.9440
O	0.5560 0.9440 0.2500
O	0.0560 0.7500 0.4440
O	0.9440 0.2500 0.5560
O	0.7500 0.4440 0.0560
O	0.4440 0.0560 0.7500

Table 7.1: Reduced coordinates of atoms

Converged parameters in ground state calculations

The ground state density is computed using a kinetic energy cutoff of 85Ry, and the electronic orbitals are expanded on a plane-wave basis set using a 6 6 6 *k*-point

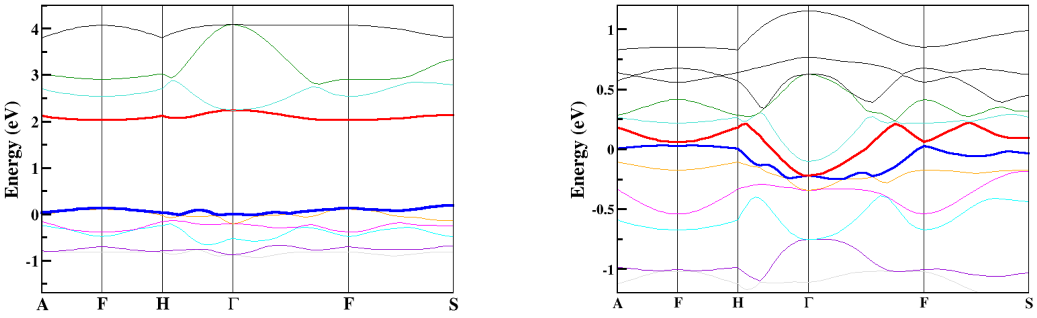

(a) LSDA

(b) LDA

Figure 7.2: Comparison of bandstructure of Cr_2O_3 using LDA and LSDA

grid and a kinetic energy cutoff of 85Ry. The convergence test for the kpoints is shown in the appendix (B.3).

7.2.2 Electronic bandstructure of Cr_2O_3

Bandstructure calculated using valence electrons pseudopotential

We calculated the band-structure of Cr_2O_3 using DFT in the local spin density approximation (LSDA), which is shown in figure (7.2a) and in the local density approximation (LDA) which is shown in figure (7.2b). First, we used the valence electrons pseudopotential.

The blue colour shows the highest valence band (HVB), and the red colour shows the lowest conduction band (LCB) in all the bandstructures given in this thesis.

The path of the bandstructure is from A → F, F → H, H → Γ, Γ → F ,F → S, where the reduced coordinates for these points are given in the table (7.2)

High symmetric points	Reduced coordinates
A	0.2 0.7 0.7
F	0.0 0.5 0.5
H	-0.2 0.3 0.3
Γ	0.0 0.0 0.0
F	0.0 0.5 0.5
S	-0.2 0.2 0.0

Table 7.2: High symmetric point coordinates

The bandstructure predicted using LSDA indicates a semiconductor, while the bandstructure calculated using LDA indicates a metallic structure. It clearly shows that including the spin in the calculation via LSDA is mandatory to get an accurate description of the structure since Cr_2O_3 is known to be a semiconductor. The calculated value of the DFT gap is given in table (7.3). As we will discuss later, the calculated DFT gap underestimates the experimental band gap.

Direct band gap	1.90eV at F Point
Indirect band gap	1.85eV between F and S point

Table 7.3: DFT band gap of Cr_2O_3

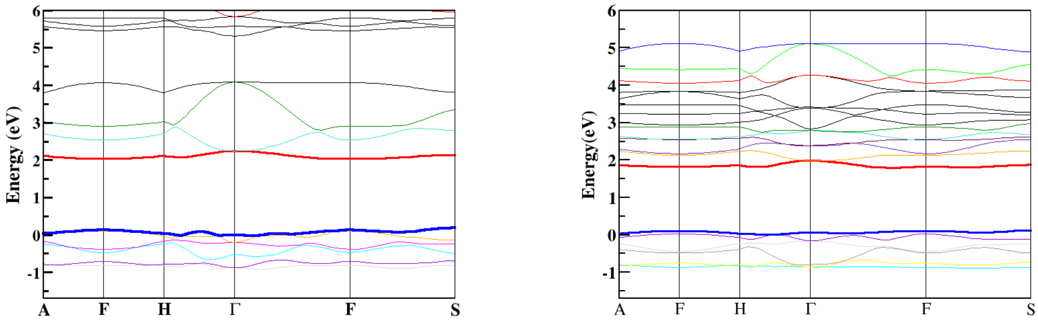

(a) Valence electrons

(b) Semicore electrons

Figure 7.3: Comparison of bandstructure of Cr_2O_3 using two different pseudopotentials

Bandstructure calculated using semicore electrons pseudopotential

Additionally, the bandstructure was computed using the semicore electrons pseudopotential and compared to the pseudopotential with valence electrons as shown in figure (7.3). We see in figure (7.3), although the two bandstructures look quite similar, there is a discernible difference in the bandstructure, namely the shape of the bands at the Γ point. In contrast to the valence electrons bandstructure, the curvature of the bands becomes opposite at the Γ point in the semicore electrons bandstructure.

The DFT band gap using semicore electrons pseudopotential is calculated and compared with the band gap calculated using the valence electrons band gap in the table (7.4).

Semicore electrons band gap	Valence electrons band gap
1.72eV	1.90eV

Table 7.4: DFT band gap of Cr_2O_3 calculated using two pseudopotentials

7.3 GW band gap

DFT calculations in the LDA for the exchange-correlation potential [16,17] can describe the ground state properties, such as the total energy and the bond lengths accurately, for a large array of systems, but are inappropriate for excited-state properties, such as the quasiparticle energies and band gap. The band gaps resulting from KS-DFT calculations are systematically underestimated [44–46].

To obtain a better representation of the electronic structure and an accurate band gap for Cr_2O_3, the inclusion of self-energy corrections to the quasiparticle energies are needed (as discussed in Chapter 5).

The application of the GW method to compute self-energy corrections on top of ab-initio DFT results has become a quite well-established and standard technique, giving energy levels generally in good agreement with experiments for a variety of materials, ranging from narrow-gap semiconductors such as InSb to wide band gap insulators such as LiF, [47–49].

In this section, we examine the quasiparticle bandstructure of Cr_2O_3 using the GW approximation. Note that this is also the basis for introducing the so-called "scissors operator" often invoked to correct the discrepancies by rigidly shifting the DFT empty bands upwards, hence avoiding explicit self-energy calculations for all bands and k-points.

In GW calculations for semiconductors, the calculation of G and W to correct the DFT bandstructure usually starts, for computational purposes, with valence electrons pseudopotentials, omitting the semicore states, which have been frozen in the pseudopotential technique(described in the section (3.3)).

However, as shown in [50], the exchange-correlation contributions to the self-energy of Copper at the 3s and 3p core levels are essential. It is shown that, when Σ is computed neglecting the 3s and 3p atomic core states, the resulting QP corrections on the d bands are clearly non physical: GW corrections move the highest occupied d band above the DFT-LDA fermi level. On the other hand, the situation for s and p states is much more reasonable, with correlation and exchange parts of the self-energy. It was explained that, even though the 3s and 3p states are physically distinct from the 3d states in terms of energy, they have a significant spatial overlap. As a result, the exchange contributions between 3d and 3s, 3p states are expected to be significant for self-energy.

For these reasons, we have examined the influence of 3s and 3p states of Cr in Cr_2O_3 on the GW QP energies by calculating the GW band gap using the two different pseudopotentials already presented, one with valence electrons only and the other with valence and semicore electrons.

7.3.1 GW Band gap calculated using pseudopotential with the valence electrons

We performed the GW calculations using the pseudopotential, which has valence electrons only, i.e. $4s^1$, $3d^5$. The total number of electrons is 60.

Calculations details

We calculated the quasiparticle (QP) energies within many body perturbation theory using the GW method, using the Abinit code. The spin polarization is included in the GW calculations.

The procedure for calculating QP energies using GW approximation starting from DFT eigenvalues and eigenfunctions is explained in section (5.6). Following that, we will compute the screening using the KS eigenfunctions and eigenvalues, and then we will use this screening to determine the self-energy. In the end, we will use this self-energy to calculate the QP energies.

In this section the convergence parameters and the procedure for calculating the screening and the self-energy calculations is discussed.

Convergence parameters

- Screening : The independent-particle susceptibility is determined and it is used to create the inverse dielectric matrix, as described in the section (5.6). The screening is then calculated using inverse dielectric matrix. The parameters that need to be converged in screening are nband, ecutwfn and ecuteps, where nband defines the number of bands and ecuteps determines the cut-off energy of the planewave set used to represent the independent-particle susceptibility, the dielectric matrix. ecutwfn determines the cut-off energy of the planewave set used to represent the KS-orbitals.

- self-energy : The parameters that need to be converged in self-energy calculations are nband, ecutwfn and ecutsigx. The convergence parameter ecutsigx, determines the cut-off energy of the planewave set used to generate the exchange part of the self-energy operator.

Convergence procedure

- We start by converging the self-energy parameter ecutwfn, ecuteps and ecutsigx using a well converged KS electronic structure i.e. containing many bands and a screening determined with "reasonable" values for the parameters nband, ecutwfn and ecuteps. The self-energy parameters are converged one by one.

- Once all of the self-energy parameters were converged, we increase the screening matrix's size and check the convergence of the self-energy parameters once again.

- We repeat this procedure until screening and self-energy are fully converged.

The energy gaps in the GW approximation have a significant dependence on the number of unoccupied bands that is slow to converge in many cases.

Converged parameters The convergence study in the GW calculations is shown in the appendix (D). The converged parameters in the screening and self-energy calculations are given below in tables (7.5) and (7.6) respectively.

ecuteps	17 Ha
ecutwfn	20 Ha
nband	390

Table 7.5: Converged value of parameters in the screening calculation

ecutsigx	28 Ha
ecutwfn	20 Ha
nband	800

Table 7.6: Converged value of parameters in the self-energy calculation

Calculated band gap

DFT direct band gap is **1.90eV** at the F point (0.0 0.5 0.5) and hence GW corrections to the KS eigenvalues are calculated at this point. The calculated **GW** band gap is **3.46eV**.

7.3.2 GW band gap calculated using pseudopotential with the semicore electrons

We performed the GW calculation using pseudopotential, which also has semicore electrons.

Calculations details

The convergence study in the GW calculations is shown in the appendix (D). The value of the converged parameters is different due to the different number of electrons included in the pseudopotential.

Converged parameter The ground state KS-orbitals are calculated using a k-point grid 4 4 4. The converged parameters in the screening and self-energy calculations are given below.

ecuteps	23 Ha
ecutwfn	26 Ha
nband	450

Table 7.7: Converged value of parameters in the screening calculation

ecutsigx	30 Ha
ecutwfn	24 Ha
nband	1000

Table 7.8: Converged value of parameters in the self-energy calculation

Calculated band gap

DFT direct band gap is **1.72eV**. **GW** band gap is **2.68eV**. The value of **scissor** in this case is **0.96**eV.

7.3.3 Effect of semicore electrons on band gap

In the above two sections (7.2) and (7.3), we have shown the results for the band gap using two different pseudopotentials (with and without semicore electrons).

Comparing the band gaps calculated using the two different pseupotentials using two different approximations (LDA and GW) are given in table (7.9). There is a substantial difference between DFT band gaps that include semicore electrons and those that do not. The inclusion of semicore electrons in the calculation modifies the LDA band gap by 0.1-0.2eV and the GW band gap by around 0.8-0.9eV. Previous studies [41] have described that the semicore electrons plays a more important role in the GW calculations than in LDA. We observe a similar pattern for the Cr_2O_3. However, for Cr_2O_3, the difference in the DFT gap is also significant.

We can consider that the GW band gap(= 2.68eV) using semicore electrons at point 0.0 0.5 0.5 is the theoretically most accurate one due to the inclusion of semicore electrons and the corresponding scissor value 0.96eV.

The corrected band gap at F is smaller than in the experiment.

The GW corrected band gap calculated using the semi core electrons pseudopotential is significantly smaller than those obtained with valence electrons pseudopotential. This shows that including 3s and 3p state in the pseudopotential significantly impacts the quasi-particle energy. As discussed previously, it is due to the exchange contribution between the 3s,3p and 3d states.

Band gap	Valence	Semicore
LDA	1.90 eV	1.70 eV
GW	3.46 eV	2.68 eV

Table 7.9: Band gap comparison using two different pseudopotentials

7.3.4 Comparison of band gap with previously reported value

Approach name	Band gap(eV)	Difference with GW Band gap with Semicore electrons (2.68eV)
Exp thin film Cr_2O_3	2.9-3.09 [51]	0.37
Exp nanoparticle Cr_2O_3	3.2 [52]	0.57
Experiment $\alpha-$ Cr_2O_3 nanoparticles	3.080 [53]	0.37

Table 7.10: Comparison of calculated band gap with previously reported experimental band gap of Cr_2O_3

This section compares the band gap value measured or computed in previous studies with the values we have obtained.

Approach name	Band gap(eV)	Difference with GW Band gap with semicore electrons (2.63eV)
Bulk Cr_2O_3 LDA+U	2.8 [54]	0.17
Bulk Cr_2O_3 PBE+U	2.9 [54]	0.27
Bulk PBE+U	2.92 [53]	0.29
Screened exchange (sX) Hybrid functional	3.31 [55]	0.68
B3LYP functional	4.4 [56]	1.77
GW RPA	4.75eV [57]	2.12

Table 7.11: Comparison of calculated band gap with previously reported theoretical band gap of Cr_2O_3

Our calculated values are shown in table (7.9). Table (7.10) shows the previously reported experimental band gaps, and calculated band gaps that have been published are included in the table (7.11). Among all our calculated values shown in table (7.9), we consider that the GW band gap value obtained using semicore electrons is the most accurate one. As a result, we compare the previously published values to this value, i.e. 2.68eV.

We first compare our calculated value for the band gap to the experimental band gap shown in the table (7.10). We see that the difference is around 0.4eV. Comparing with previously published band gaps calculated using ab-initio approaches, in table (7.11), we see that the calculated band gaps spread over a wide range. We see that our value is in good agreement with the value reported in [54] using LDA+U.

Chapter 8

Linear response of Cr_2O_3

We will discuss the linear optical properties of Cr_2O_3 in this chapter. We studied the linear response of Cr_2O_3 in the TDDFT framework. We compared the linear spectra calculated using a different approximation in TDDFT. Also, the linear spectra of Cr_2O_3 has been studied in the BSE framework. At last, we compared the BSE spectra with the spectra calculated using a different approximation in TDDFT.

8.1 Linear response calculated using TDDFT

In this section we present the linear properties of Cr_2O_3 in the framework of TDDFT. We first built the independent-particle response function $\chi^{(0)}$ for the Cr_2O_3 using Kohn-Sham DFT orbitals. To account for the GW quasiparticle energies and the opening of the band gap, we used a scissor value $\Delta = 0.73$ eV, which is the difference between the GW band gap calculated using semicore electron pseudopotential and LDA band gap calculated using valence electron pseudopotential for Cr_2O_3 (described in the figure (8.1)).

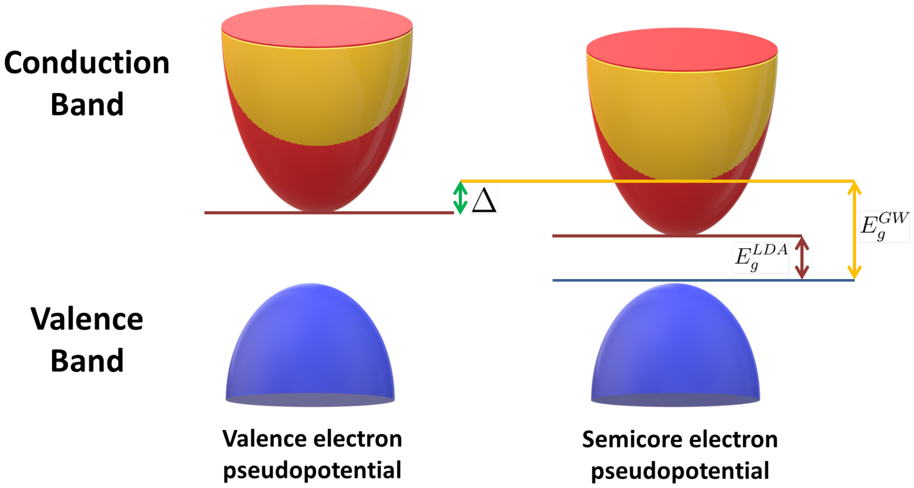

Figure 8.1: Scissor value for Cr_2O_3

We compared the linear spectra obtained with RPA, and we examined the effect of incorporating spin-polarization at the IPA and RPA levels in Cr_2O_3.

Finally, we will characterize the linear spectrum of Cr_2O_3 using TDDFT with several exchange-correlation kernels.

8.1.1 Calculation details

To compute the linear response in the TDDFT framework, the DFT-LDA KS electronic structure of the Cr_2O_3 is first determined by a ground state calculation. The numerical details for the ground state DFT calculation are given in the section (7.2.1).The linear response using TDDFT calculations is carried out in this thesis using the DP code [58].

Details of the convergence parameters, which are employed in the TDDFT calculations, are provided in the following table (8.1)

nband	npwmat	npwwfn
70	113	3000

Table 8.1: TDDFT converged parameters value

Where nband specifies the number of bands that were considered in the independent particle response function $\chi^{(0)}$. Convergence in terms of number of bands is shown in the appendix (B.1). Convergence in terms of number of planewaves is shown in the appendix (B.2). Crystal local-field effects were taken into consideration by solving the Dyson equation (4.18) in momentum space, where npwmat is the number of G-vectors, and the parameter npwwfn defines the number of planewaves used to describe the KS orbitals.

Unless otherwise stated, the value of these parameters remains constant throughout this section (8.1). Also, for Cr_2O_3, $\epsilon_M(xx) = \epsilon_M(yy) \neq \epsilon_M(zz)$. where $\epsilon_M(xx)$, $\epsilon_M(yy)$ and $\epsilon_M(zz)$ denoted the xx, yy and zz component of the dielectric function respectively. If we did not indicate the component for the ϵ_M, it is assumed that it has the zz component throughout the chapter.

8.1.2 Linear response in IPA and RPA

We determined the linear response of Cr_2O_3 using various TDDFT approximations. As indicated in figure (8.2), we estimated the linear response using Independent Particle Approximation (IPA) which is described in section (4.2.3).

The response functions can be evaluated in a straightforward manner using the RPA also, which includes only the Hartree contribution to the linear response kernel.

We plotted the imaginary part of the (ϵ_M), which represent the absorption as described in the chapter (2). We compared the spectra obtained in IPA (no local field effect) and RPA (with local field effect) in figure (8.2). We note that the local field effects decrease the amplitude of the RPA spectrum, but the change is very small.

Because the structure of Cr_2O_3 is anisotropic, it is crucial to look at the linear spectra in different directions. Further, we compared the different components of the linear response of Cr_2O_3 in the RPA approximation in figure (8.3). The first

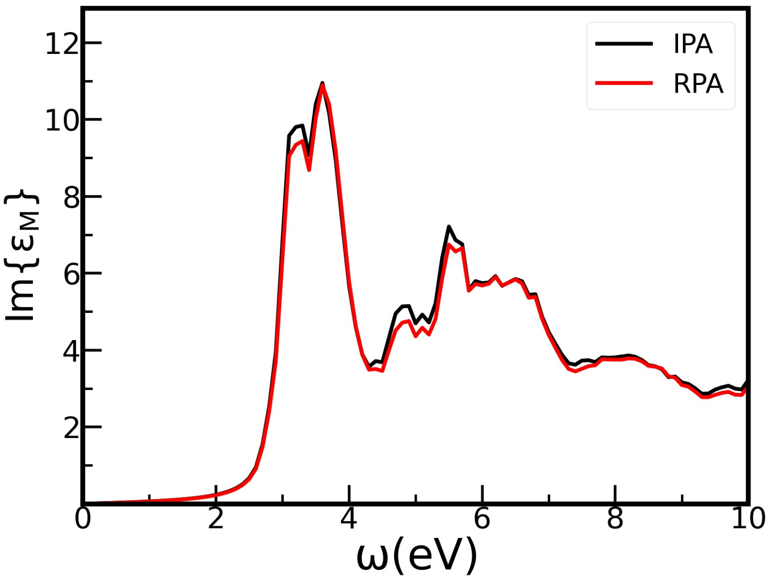

Figure 8.2: Linear response of Cr_2O_3 calculated using IPA and RPA in TDDFT

two components, xx and yy, are identical; however, the third component, zz, is drastically different, as seen in figure (8.3). The first peak in the zz component has a very high intensity as compared to the two other components.

8.1.3 Linear response including spin-polarization

As shown in section (7.2), including the spin-polarization at the DFT level is mandatory for getting the antiferromagnetic structure of Cr_2O_3. In this section, we wish to investigate the effect of spin-polarization in the linear response. We performed linear response calculations, including spin-polarization and without including spin-polarization. Here, we want to specify in detail the effect of including the spin-polarization.

Effect of spin-polarization in IPA

In the IPA, the response function can be written as,

$$\chi_0^{(1)}(\mathbf{q}+\mathbf{G},\mathbf{q}+\mathbf{G}',\omega) = \frac{1}{V}\sum_{nn'\mathbf{k}s}\frac{(f_{n,\mathbf{k}s}-f_{n',\mathbf{k}+\mathbf{q}s})}{E_{n,\mathbf{k},s}-E_{n',\mathbf{k}+\mathbf{q},s}+\omega+i\eta}$$
$$< \phi_{n,\mathbf{k},s}|e^{-i(\mathbf{q}+\mathbf{G})\mathbf{r}}|\phi_{n',\mathbf{k}+\mathbf{q},s} >< \phi_{n',\mathbf{k}+\mathbf{q},s}|e^{-i(\mathbf{q}+\mathbf{G}')\mathbf{r}'}|\phi_{n,\mathbf{k},s} > \tag{8.1}$$

where s denotes the spin. The response function can then be written as,

$$\chi_0^{(1)} = \chi_0^{(1)(\uparrow)} + \chi_0^{(1)(\downarrow)} \tag{8.2}$$

For non-magnetic materials, the two spin components are equal, and the summation over spins leads to an overall factor 2, but for magnetic materials, $\chi_0^{(1)(\uparrow)}$ and $\chi_0^{(1)(\downarrow)}$ can be different. In the IPA one only retains the $G = 0, G' = 0$ reciprocal

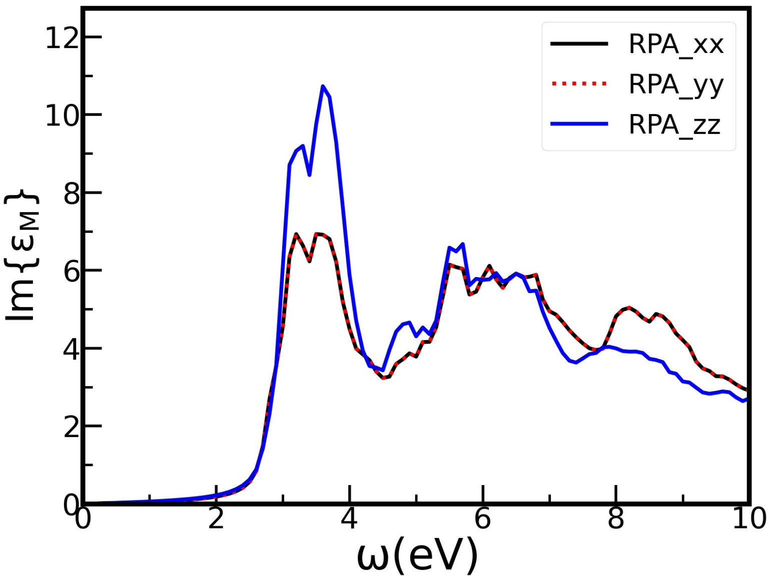

Figure 8.3: Linear response of different component of Cr_2O_3 calculated using RPA

space vectors, and one can show that for antiferromagnetic structures, such as Cr_2O_3, the ↑ and ↓ components satisfy,

$$\chi_0^{(1)(\uparrow)}(\mathbf{q},\mathbf{q},\omega) = \chi_0^{(1)(\downarrow)}(\mathbf{q},\mathbf{q},\omega) \tag{8.3}$$

and using the relation

$$\epsilon_M(\mathbf{q},\omega) = 1 - v(q)\chi_0^{(1)}(\mathbf{q},\mathbf{q},\omega) \tag{8.4}$$

the imaginary part of the dielectric function ϵ_M is,

$$Im\,\epsilon_M(\mathbf{q},\omega) = 2Im\,\epsilon_M^{\uparrow}(\mathbf{q},\omega) = 2Im\,\epsilon_M^{\downarrow}(\mathbf{q},\omega) \tag{8.5}$$

This feature is visible in (8.4) spectrum, where the two graphs are stacked as expected.

Effect of spin-polarization in RPA

On the contrary, in RPA the response function can be written as,

$$\begin{aligned}\chi^{(1)}(\mathbf{q}+\mathbf{G},\mathbf{q}+\mathbf{G}',\omega) &= \chi_0^{(1)}(\mathbf{q}+\mathbf{G},\mathbf{q}+\mathbf{G}',\omega) + \\ +\sum_{\mathbf{G}''}\chi_0^{(1)}(\mathbf{q}+\mathbf{G},\mathbf{q}+\mathbf{G}'',\omega)&v(\mathbf{q}+\mathbf{G}'')\chi^{(1)}(\mathbf{q}+\mathbf{G}'',\mathbf{q}+\mathbf{G}',\omega)\end{aligned} \tag{8.6}$$

where the summation over G” runs over the reciprocal space can be written as,

$$\chi_0^{(1)(\uparrow)}(\mathbf{q}+\mathbf{G},\mathbf{q}+\mathbf{G}^{'},\omega) \neq \chi_0^{(1)(\downarrow)}(\mathbf{q}+\mathbf{G},\mathbf{q}+\mathbf{G}^{'},\omega) \tag{8.7}$$

for $\mathbf{G} \neq 0$ and $\mathbf{G}' \neq 0$, one expects

$$\chi^{(1)}(\mathbf{q},\mathbf{q},\omega) \neq \chi^{(1)\uparrow}(\mathbf{q},\mathbf{q},\omega) \tag{8.8}$$

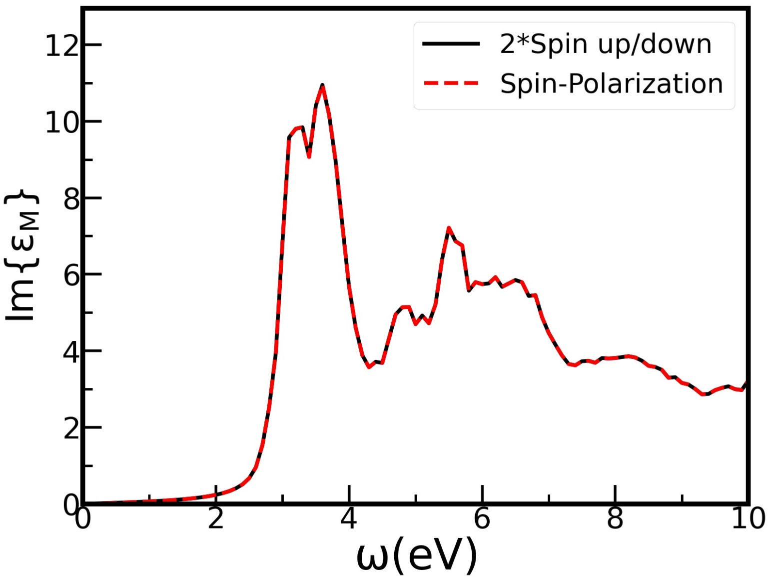

Figure 8.4: Effect of spin-polarization in the spectra calculated using IPA

In the following, **2*Spin up/down** means that we show the results of the calculation where we use only one spin component, and we multiply at the end by a factor to account for the spin

$$\chi_0^{(1)} = 2\chi_0^{(1)(\uparrow)}(\mathbf{q},\mathbf{q},\omega) = 2\chi_0^{(1)(\downarrow)}(\mathbf{q},\mathbf{q},\omega) \tag{8.9}$$

Spin-Polarization means that the dyson equation has been solved taking explicitly into account the 2 spin-components

$$\chi_0^{(1)} = \chi_0^{(1)(\uparrow)}(\mathbf{q}+\mathbf{G},\mathbf{q}+\mathbf{G}',\omega) + \chi_0^{(1)(\downarrow)}(\mathbf{q}+\mathbf{G},\mathbf{q}+\mathbf{G}',\omega) \tag{8.10}$$

One sees in the RPA spectrum (8.5) that the difference between the two graphs is very small.

8.1.4 Effect of the exchange-correlation kernel in TDDFT

In TDDFT, the exact linear-response function may be formally connected to the noninteracting Kohn-Sham linear-response function via the exchange-correlation kernel f_{xc}, which is the functional derivative of the exchange-correlation potential with respect to the density. Thus, the knowledge of the exchange-correlation kernel is critical for determining the system's exact response function. As with the static case, the Kohn-Sham formulation of TDDFT simplifies the many body problem by reducing it to finding a suitable estimate for the exchange-correlation kernel.

Many distinct kernels have previously been designed, which are briefly listed below. The objective of the present section is to provide some insight into the nature of the exchange-correlation kernel for Cr_2O_3.

TDLDA is one of the simplest xc kernels, and it requires less computational effort and is hence suitable for the larger system [59]. However, this approximation fails to produce satisfying results in some circumstances due to the lack of long-range contribution.

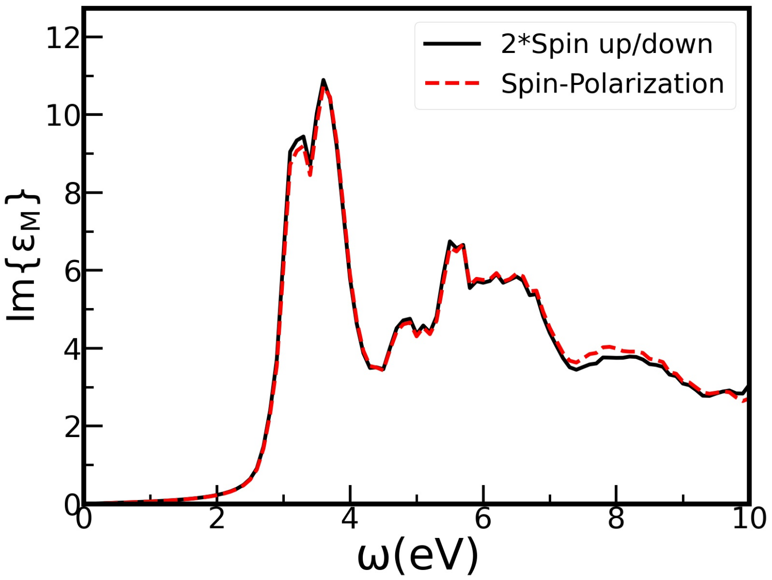

Figure 8.5: Effect of spin-polarization in the spectra calculated using RPA

Although the long-range component of the exchange-correlation kernel f_{xc} is not present in local density or generalized gradient approximations, it is assumed to exist in the precise f_{xc}.

Additionally, a static long-range contribution is insufficient to generate a good total f_{xc} to be used on top of the KS-LDA bandstructure rather than the GW bandstructure previously used in this work. Such a f_{xc} should simultaneously push the spectrum to higher energies while also enhancing the low-energy structures. This difficult task cannot be accomplished through a single effective LRC contribution.

For several xc kernels proposed in the literature, including the long-range xc kernel [60], Bootstrap , RPA-Bootstrap [61], and Jellium-with-gap model(JGM) kernels [62] it is reported that the long-range part contributes the most to the results for optical spectra in solids.

In this section, the influence of exchange-correlation effects beyond the RPA are studied in detail for optical spectra of Cr_2O_3.

As stated above, the quasiparticle corrections have been included at the level of a scissor operator.

Linear response calculated using the LDA kernel in TDDFT

The homogeneous electron gas (HEG) model [63], [64] has been used in the construction of xc kernels since the very beginning of DFT, and one of the most widely used approach is time-dependent local density approximation (TDLDA), which is derived from the local-density approximation (LDA) xc potential v_{xc} in the static regime, i.e. the adiabatic LDA (ALDA) [63], and can be written as

$$f_{xc}^{\mathrm{ALDA}}(\mathbf{r},\mathbf{r}') = \left.\frac{\delta v_{xc}^{\mathrm{LDA}}(\mathbf{r},\omega)}{\delta n(\mathbf{r}',\omega)}\right|_{\omega=0} = \delta(\mathbf{r}-\mathbf{r}')\frac{dv_{xc}^{\mathrm{LDA}}[n(\mathbf{r})]}{dn(\mathbf{r})} \tag{8.11}$$

ALDA is responsible for redistributing oscillator strength and modifying exci-

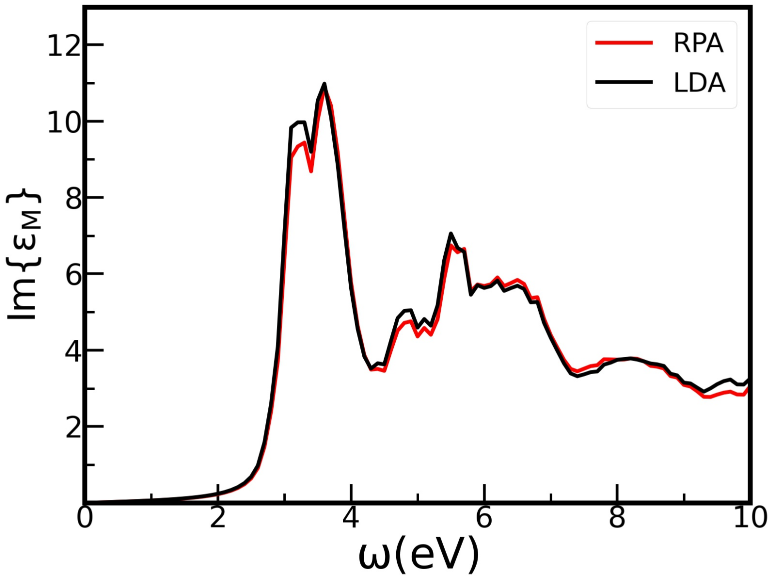

Figure 8.6: Linear response of Cr_2O_3 calculated using LDA and RPA in TDDFT

tation energies. It has been effectively used for atoms and clusters [65], [63], but it has been shown to be inefficient in many cases in condensed matter, where the gain over the random-phase approximation (RPA, with trivial $f_{xc} = 0$) is small [66]. We see that for Cr_2O_3, Fig.(8.6), we have also such a behavior, as the spectra obtained in RPA and in ALDA are almost identical.

As seen in Fig.(8.2), the local-field effects, introduced in the Hartree contribution, are already weak and so including f_{xc} within TDLDA does not result in a significant improvement in this scenario. Consequently, we need to go beyond TDLDA.

Linear response calculated using long-range kernel in TDDFT

The long-range contribution (LRC) to the xc kernel can be written as,

$$f_{xc}^{LRC}(r, r') = -\frac{\alpha}{4\pi|r - r'|} \tag{8.12}$$

(where α is a material dependent parameter). It has been shown to significantly improve the optical absorption spectra for solids with continuum excitons as compared to computations using the adiabatic local-density approximation [60].

The Fourier transform of the equation (8.12) is given as,

$$f_{xc}(\mathbf{q}, \mathbf{G}, \mathbf{G}') = -\alpha\delta_{\mathbf{G},\mathbf{G}'}/|\mathbf{q} + \mathbf{G}|^2 \tag{8.13}$$

In the report [60] it is shown that the crucial part of the electron-hole interaction (8.13) comes from its $\mathbf{G} = 0, \mathbf{G}'$ contribution (which diverges for $q \to 0$): the results obtained with only the head of the kernel ($\mathbf{G} = 0, \mathbf{G}' = 0$) were indistinguishable from those obtained for $\mathbf{G} \neq 0$ for the same value of α. Hence, in the following we will use the kernel f_{xc} neglecting all $\mathbf{G} \neq 0$ terms which then has the form of $\frac{\alpha}{q^2}$.

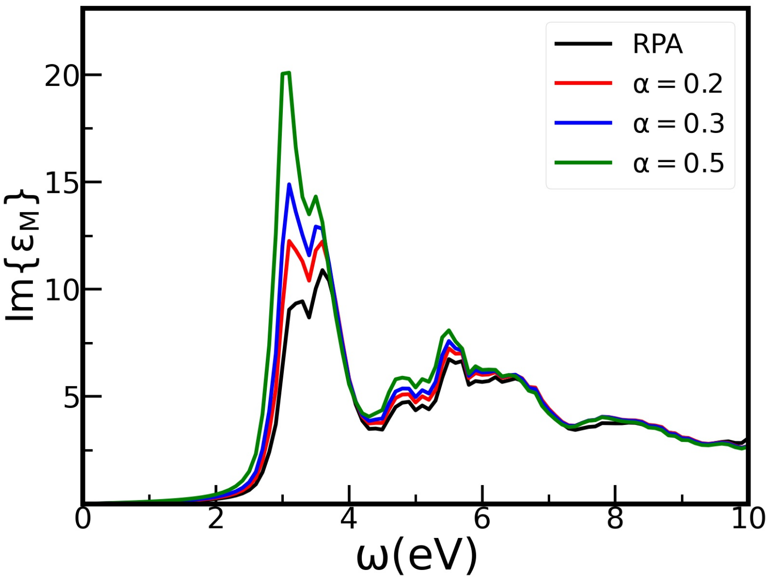

Figure 8.7: Linear response of Cr_2O_3 calculated using RPA and alpha-kernel in TDDFT

In [60] the implications of a static long-range contribution $-\frac{\alpha}{q^2}$ to the time-dependent density functional theory exchange-correlation kernel $f_{xc}(q)$ is examined for a variety of semiconductors. The linear response of several semiconductors has been computed in the TDDFT framework using the static long-range kernel and by solving the Bethe-Salpeter Equation. Comparing these two approaches made it possible to find a "good" value for the α parameter. It was shown that α varies linearly with ϵ_∞^{-1} for semiconductors with a high value of the dielectric constant. As a result, they illustrate the values of α in relation to the inverse of the dielectric constant which is given as,

$$\alpha = 4.615\epsilon_\infty^{-1} - 0.213 \tag{8.14}$$

where, ϵ_∞ is the static dielectric constant. This approximation produces very good agreement with the experimental results for a wide range of semiconductors [60].

With the help of the fit given by the equation (8.14), the estimated value of α is 0.5 for Cr_2O_3.

After witnessing this kernel's remarkable success with a variety of semiconductors, we wanted to investigate whether similar good results could be obtained for Cr_2O_3 by using the LRC kernel with a workload equivalent to that of a basic RPA calculation.

We began by calculating the spectra using arbitrary values for α. As we can see in figure (8.7), increasing α increased the amplitude of the main peak. And for all value of α we observed that the amplitude of the peak is larger than the peak in RPA. We also note that, as the value of α increases, the absorption edge shifts to the left (redshift). If we increase the value of α to 1.0, we see a dramatic change in the spectrum (8.8). For example, for $\alpha = 1$ peak is redshifted by 0.29 eV relative to the $\alpha = 0.5$ peak, and by approximately 0.35 eV relative to GW-RPA. In fact, there is a non-uniform shift in peak positions.

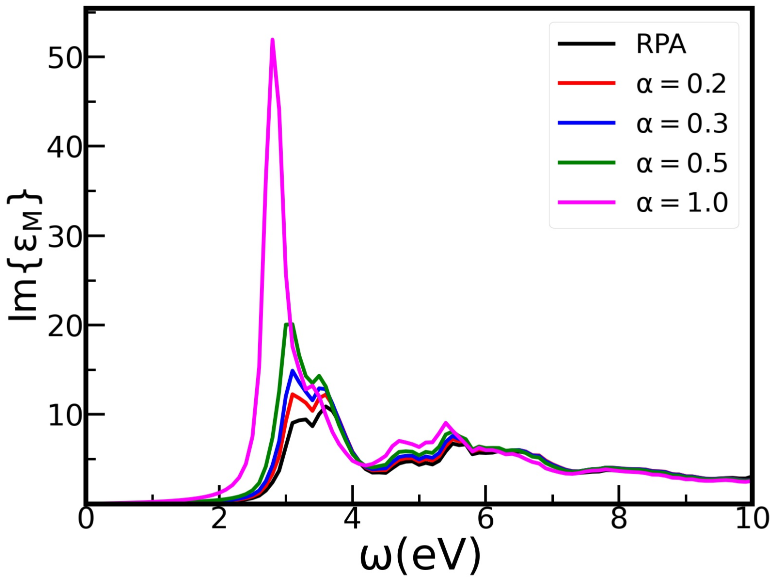

Figure 8.8: Linear response of Cr_2O_3 calculated using RPA and alpha-kernel in TDDFT

Note that the shape of the absorption peak remains quite similar for all the values of α, and the second peak shape and height are the same for all values of α.

We do not know a priori which is the best value for the α parameter for Cr_2O_3. However, we see that the spectra are different for various values of α, and it is essential to have an appropriate value of alpha for Cr_2O_3 in order to get accurate spectra.

Several kernels can provide α for a given material. We further extended the spectra calculation by using these kernels in the TDDFT framework.

Linear response calculated using Jellium Gap Model kernel

Another static approximation to the exchange-correlation kernel, based on the Jellium-with-gap (JGM) model, is presented within the TDDFT framework. This kernel has been designed to account for electron-hole interactions at low computational cost and should be able for accounting for both strongly bound and weak excitonic effects in some materials, as shown in [62]. The JGM kernel is based on a well-known physical model system, the Homogeneous Electron Gas (HEG). It provides a straightforward and analytical formula for the α coefficient, which is described below.

As described in [62], the JGM kernel can be expressed in terms of density(n) and band gap (E_g) as,

$$f_{xc}^{\mathrm{JGM}}(q;n,E_g) = \frac{4\pi}{q^2} B'(n,E_g)\left[e^{-k'_{n,E_g} q^2} - 1\right] - \frac{4\pi}{k_F^2}\frac{C'(n,E_g)}{1+1/q^2} \tag{8.15}$$

where k'_n, $B^{'}(n,E_g)$ and $C'(n,E_g)$ are defined in reference [67]. k'_n and $C'(n,E_g)$ are constructed from the HEG constraint and $B'(n,E_g)$ is constructed from HEG diffusion Monte Carlo data.

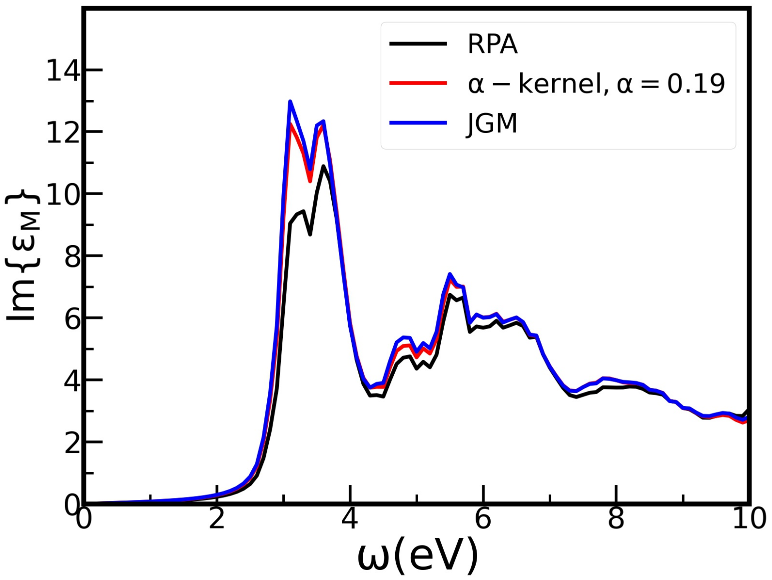

Figure 8.9: Linear response of Cr_2O_3 calculated using JGM, alpha and RPA

In the article [62] the limit for $q \to 0$ is presented: the second term of the equation (8.15) vanishes and the f_{xc} becomes,

$$\lim_{q\to 0} f_{xc}^{\mathrm{JGM}}(q; n, E_g) \approx -\alpha^{\mathrm{JGM}}(n, E_g)/q^2 \tag{8.16}$$

where,

$$\alpha^{\mathrm{JGM}}(n, E_g) = 4\pi B'(n, E_g)\left[1 - e^{-E_g^2/4\pi n B'(n,E8)}\right] \tag{8.17}$$

Thus, an explicit value for the LRC α parameter is provided as the mean value of (α^{JGM}).

$$\langle\alpha\rangle \equiv \int \alpha^{\mathrm{JGM}}(n(\mathbf{r}), E_g)d\mathbf{r} \tag{8.18}$$

This section will examine the results obtained using the nonempirical static xc kernel based on the JGM and compare them to those previously obtained using RPA and the long-range kernel.

The value of α, as determined from the JGM kernel, is close to 0.2. In comparison to the α-kernel, the advantage of this kernel is that it provides the value of alpha thus we do not have to specify it beforehand.

We show in figure (8.9) the absorption spectra obtained using a long-range approximation with $\alpha = 0.19$ and the JGM kernel. We can see that the spectra obtained using the two kernels exhibit only small differences. This minor variation is caused by the presence of the G-vector in JGM kernel, while only $G = 0$ is considered in the long-range kernel. The RPA and JGM kernels differ only in the amplitude of the first peak, the JGM kernel considerably amplifies the first peak, but the high energy parts of the spectra are comparable.

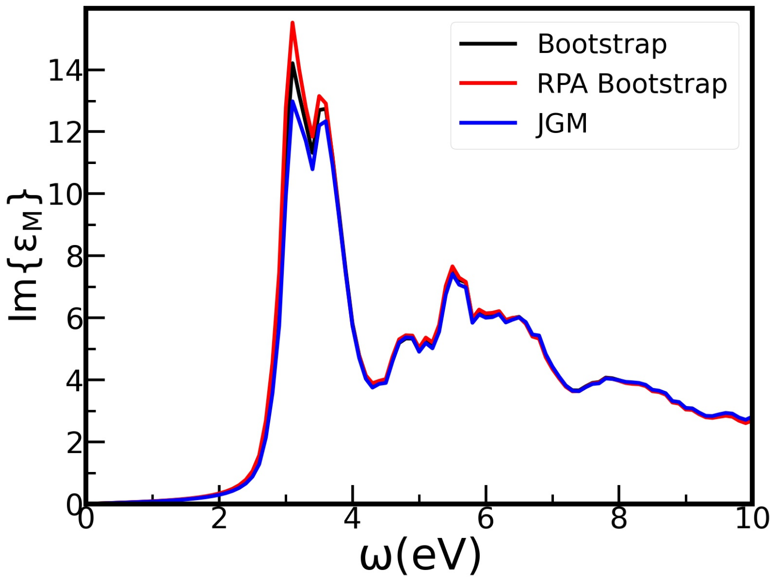

Figure 8.10: Linear response of Cr_2O_3 calculated using Bootstrap, Bootstrap RPA and Jellium Gap Model kernel in TDDFT

Linear response calculated using Bootstrap and Bootstrap RPA kernels in TDDFT

Recently, a new family of exchange-correlation kernels has been developed based on a "bootstrap" approach [68]. In this approach, a heuristic form is derived based on the screening that must be calculated self-consistently.

$$f_{xc}^{Boot} = \epsilon^{-1}/\chi_0 \tag{8.19}$$

Where ϵ^{-1} denotes the microscopic inverse dielectric function, and χ_0 is the Kohn-Sham response function. It has been used successfully to calculate optical spectra for a wide variety of bulk materials.

Another approach is the Bootstrap-RPA kernel [61] which can be written as,

$$f_{xc}^{RPA-Boot} = \epsilon_{RPA}^{-1}/\tilde{\chi}_{RPA} \tag{8.20}$$

where, $\tilde{\chi}_{RPA}$ is the solution of the Dyson equation in which only the short range part of the Coulomb potential $\bar{v}$ is considered.

It is a parameter-free kernel for exciton binding energies of semiconductors and insulators.

Using the Bootstrap XC kernels to calculate optical spectra has been shown to capture some features of the absorption peaks that correspond to excitonic effects.

Note that, in some cases, the exciton binding energies can be calculated using the Bootstrap kernel, as demonstrated [68] [69].

The report [69] demonstrates that the exciton binding energy computed using the Bootstrap xc kernel is significantly underestimated for transition metal dichalcogenides.

We used these two kernels to compute the Cr_2O_3 optical spectra. To begin, we compared the spectra obtained with these two kernels to the spectrum calculated

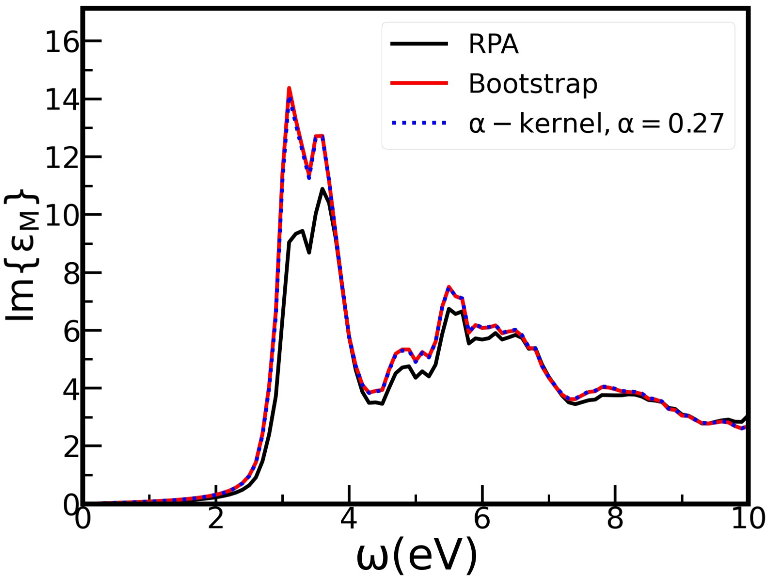

Figure 8.11: Linear response of Cr_2O_3 calculated using RPA, Bootstrap and alpha kernel in TDDFT

with the JGM kernel shown in figure (8.10). As illustrated in the graph, the computed spectra for the Bootstrap and RPA Bootstrap kernels are slightly different. The only difference is the amplitude of the first peak. At high frequencies, both peaks are directly above one another. The absorption edge is identical in both cases. This behaviour observed for Cr_2O_3 is identical to that observed in the study for silicon [61]. However, this behaviour is quite different from that reported [61] for LiF and Ar, where there is a blue shift in the Bootstrap peak as compared to the RPA Bootstrap peak.

In the same way, the difference between the spectra generated using the Bootstrap and JGM kernels is the strength of the first peak. Compared to the two Bootstrap spectra, the first peak amplitude for the JGM spectrum is less intense. By comparing these spectra to the one obtained in the framework of LRC, we can compute an effective value of α for these kernels, as shown in the table (8.2).

Approach	Bootstrap	RPA Bootstrap	JGM
α value	0.27	0.33	0.19

Table 8.2: Different alpha values extracted using three different approaches

Further, it is interesting to see the difference between the two spectra calculated using the RPA Bootstrap kernel and the long-range kernel using the alpha value calculated from the RPA Bootstrap kernel. We also compared these results with the RPA spectra, as shown in the figure (8.11).

Due to the small difference between the two spectra (Bootstrap and RPA Bootstrap), we chose Bootstrap for these comparisons. As illustrated in the figure (8.11), there is no difference between the spectra generated using the long-range and RPA Bootstrap kernels. Whereas, the distinction between RPA and Bootstrap is significant. Due to the excitonic effect, using the Bootstrap kernel improves the intensity of the peaks. However, at extremely high frequencies, the intensity of two peaks is identical. Whereas, the spectra estimated with the Bootstrap kernel exhibit a little redshift. The effect of using the Bootstrap kernel in linear spectra of Cr_2O_3 is comparable to the one observed for SiC and GaAs, except for the strength of the first peak. The Bootstrap kernel significantly strengthens the first peak in Cr_2O_3 when compared to SiC and GaAs (as shown in the reference [68]).

As a result, we may state that the excitonic effect present in the Bootstrap kernel contributes significantly to the Cr_2O_3 spectra.

8.1.5 Effect of including semicore electrons on the Linear Response

As discussed in section (7.3.3), considering the semicore electron pseudopotential has a significant impact on the GW band gap. This leads us to investigate the effect of incorporating semicore electrons on the Cr_2O_3 linear response.

As discussed in the previous section, we got the value of the GW band gap for both the cases, i.e. valence electron and semicore electron pseudopotential. We considered the GW band gap with semicore electron case to be the most accurate one. For both calculations of the linear response (valence and semicore electron), we will use the GW band gap calculated using semicore electron which is 2.63eV. As a result, the scissor value used for the linear spectra of semicore electron is 0.93eV, while the scissor value used for the linear response of valence electron is 0.78eV.

Effect of semicore electrons on the linear response of Cr_2O_3 structure in RPA and JGM kernel

We present the effect of including the semicore electrons in the calculation on the absorption spectra, calculated in the framework of RPA in the figure (8.12). The change in the spectra is quite important. Incorporating the semicore electrons of the Chromium atom strengthens the first peak in the Cr_2O_3 spectrum. Surprisingly, it also strengthens the second peak. This phenomenon has never been observed previously in any linear spectrum of Cr_2O_3.

Another interesting aspect visible in the figure is that the first peak of the semicore spectrum is redshifted, although the it does not come from a change in the band gap. On the contrary, the second peak is significantly blueshifted relative to the valence peak and another peak, which we might refer to as the third peak, can be seen in the higher energy plateau.

The frequency range across which we plotted the two peaks are clealy distinct. Additionally, spectra calculated using semicore electron have broader peak width.

Additionally, we compare the linear response of Cr_2O_3 the JGM kernel to determine the effect of the semicore electron pseudopotential when using a xc kernel. As can be shown in figure (8.13), introducing semicore electrons has the same qualitative effect on the RPA and JGM spectra. This shows that inserting the xc kernel has no additional effect on the semicore electron spectra.

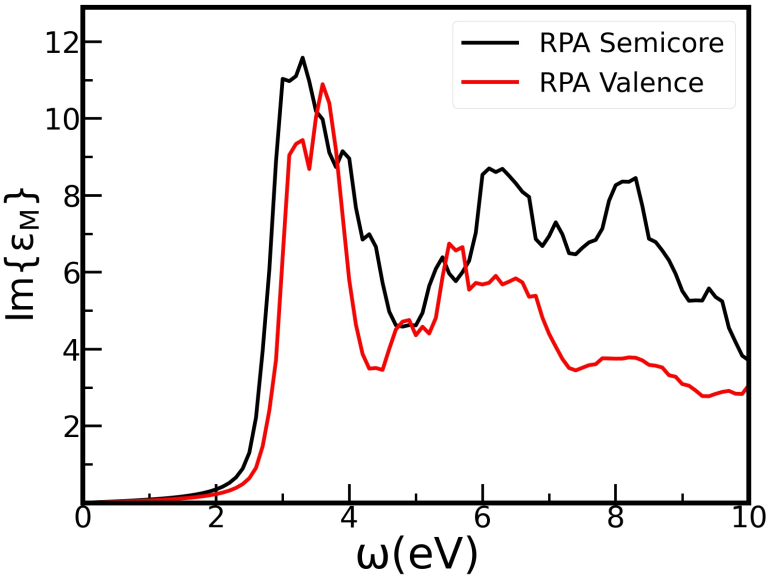

Figure 8.12: Effect of Semicore electron on Linear Response of Cr_2O_3 in RPA

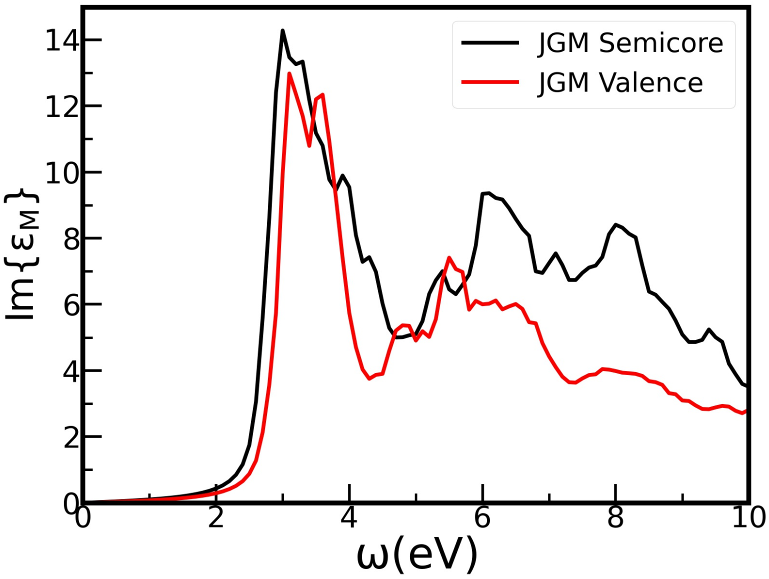

Figure 8.13: Effect of Semicore electron on Linear Response of Cr_2O_3 using JGM

8.2 Linear response using Bethe Salpeter Equation

Since new techniques and increased computer power make numerical simulations viable for real systems, the theoretical description of electronic excitations in the framework of MBPT discussed in the chapter (6) has advanced rapidly. This section is devoted to the calculation of the absorption spectra for Cr_2O_3 in the framework of BSE, which will be used as reference and compared to the results obtained in the framework of TDDFT.

8.2.1 Calculations details

No well-converged values are, to our knowledge, available yet from the BSE approach for these very simple materials, which stresses again the necessity to find an alternative strategy. A few parameters value need to be converged while doing the BSE calculations. Also, to do the accurate BSE calculations, we need to converge the screening parameters. The converged screening parameters are given in the table (8.3). The convergence in terms of the number of bands in the screening calculations is shown in the appendix (B.4.1). The BSE converged parameter value is shown in the table 8.4. The convergence in terms of the number of band in BSE is shown in the appendix (B.4.2).

nband	npwmat	npwwfn
200	113	1600

Table 8.3: Screening converged parameters value

nband	npwmat	npwwfn
60	113	3000

Table 8.4: BSE converged parameters value

Where npwwfn defines the number of planewave to describe wavefunctions, npwmat defines the G-vector needed to close the shell related to the local field. Calculations of BSE are performed using the exc code [70].

8.2.2 Comparison of RPA and BSE spectra

To begin with, we compared the BSE spectra to the RPA spectra in the figure (8.14). The first observation is that the BSE spectrum contains a bound excitonic peak absent from the RPA spectrum. The binding energy of the exciton is $E_B = 1.38eV$, indicating that it is a strongly bound exciton.

Second, there is a discernible variation between the two spectra's absorption edges. Due to the significant excitonic impact, the absorption edge of the BSE spectrum is redshifted. The final distinction is the peak amplitude. The first peak intensity is increased by 50% over the RPA. Even at high frequencies, the two spectra are distinct.

As we compared the RPA spectra in three different directions for Cr_2O_3 we also wanted to compare the BSE spectra in three directions. Therefore, using the BSE

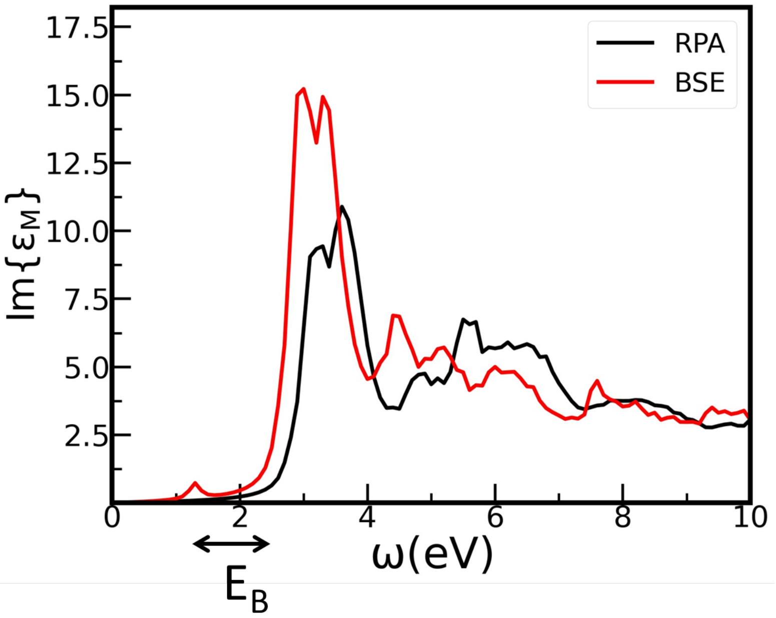

Figure 8.14: Linear response of Cr_2O_3 calculated using Bethe Salpeter Equation and RPA in TDDFT

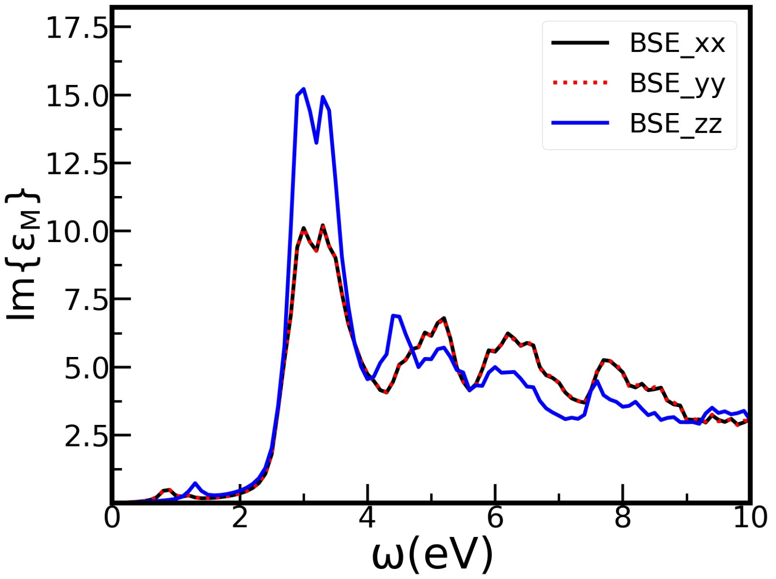

Figure 8.15: Linear response of different component of Cr_2O_3 calculated using BSE

technique, we also estimated the distinct components of linear spectra of Cr_2O_3. The outcome can be seen in figure (8.15), where the xx and yy components are stacked on top of each other due to the symmetry of material, but the zz component is visibly distinct. Another remarkable difference comes from the location of the excitonic peak for the xx(or yy) component, which is redshifted compared to the zz component. The amplitude of the main peak for the xx direction is also decreased as compared to the zz component. The excitonic binding energy for the xx and yy component is the $E_B = 1.83eV$

8.3 Comparison of BSE spectra with the spectra calculated using TDDFT approximations

Because the RPA spectrum does not contain excitonic interaction, the disparity in the spectra was expected. However, the contrast in these spectra reveals the excitonic effect's function in Cr_2O_3.

As far as we know, the BSE spectra is believed to be the most accurate technique thus so far, as it accurately accounts for the excitonic effect. Thus, we can compare the BSE spectrum to the TDDFT spectra derived using different exchange-correlation kernels. This can provide information about the correctness of the various kernels outlined in the preceding section (8.1.4).

This section will compare the spectra estimated using BSE and different xc kernels in TDDFT.

8.3.1 Comparison of alpha-kernel and BSE spectra

We first compared the α kernel result to the BSE spectra. Based on this comparison, we can compute the precise value of α for the Cr_2O_3 and determine if the fit described in section (8.1.4) to calculate the α works well for Cr_2O_3 or not.

We determined α by adjusting it until the BSE and TDDFT-LRC spectra are similar, which is trivial because the calculations are fast for TDDFT.

Based on the comparison with the first peak, we conclude that α=0.33 is the best match with the BSE spectra. However, the two spectra remain different at high energy in that case.

We calculated α to be 0.5 using the fit provided by the equation (8.14). The first conclusion we can draw from this is that the fit provided by the equation (8.14) does not work for the Cr_2O_3, probably because this fit has been proposed for materials with high dielectric constant.

Further, we compared the spectra calculated using α=0.33 with the BSE and RPA spectra in figure (8.17) to point out the difference of excitonic effect in the alpha kernel and BSE in the graph. We can see in figure (8.17) that one effect of the LRC kernel is an apparent shift of peak in the Cr_2O_3 spectra. This is in agreement with the behaviour of the Bethe-Salpeter approach in the case of materials dominated by continuum excitons, i.e. materials with a small to moderate electron-hole interaction.

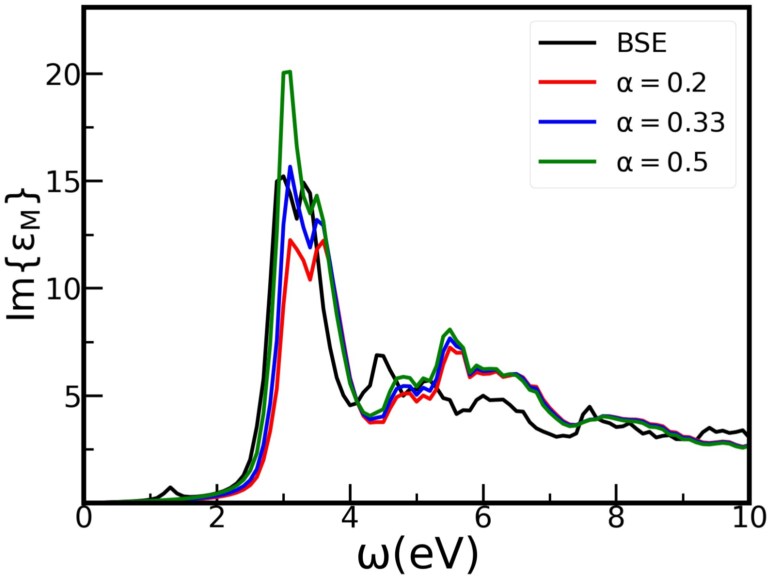

Figure 8.16: Linear response of Cr_2O_3 calculated using Bethe Salpeter Equation and alpha kernel in TDDFT

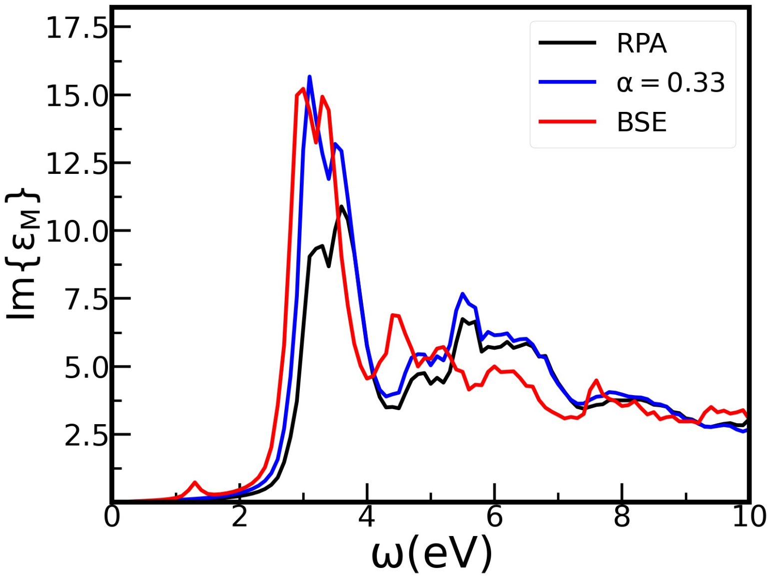

Figure 8.17: Linear response of Cr_2O_3 calculated using Bethe Salpeter Equation and alpha kernel and RPA in TDDFT

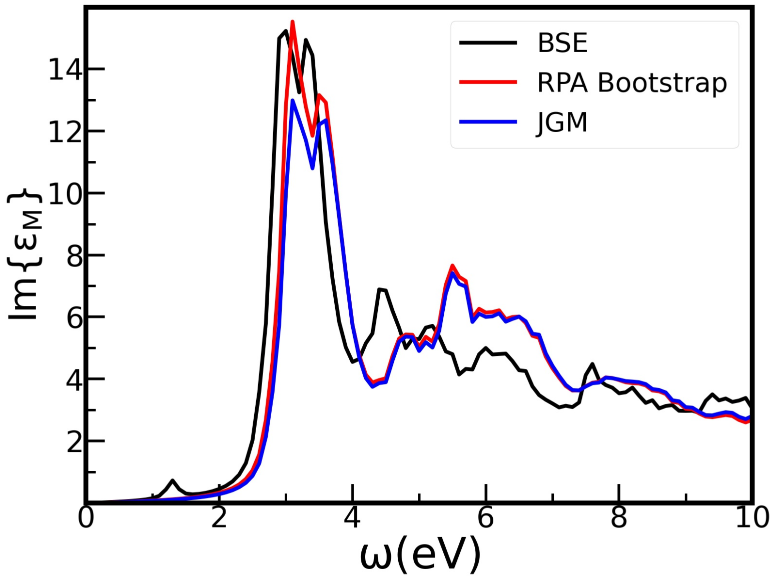

Figure 8.18: Linear response of Cr_2O_3 calculated using Bethe Salpeter Equation and RPA Bootstrap in TDDFT

However, the BSE and TDDFT-LRC approaches operate significantly differently in the case of materials with strongly bound excitons when absorption peaks are located within the band gap. Indeed, the Bethe-Salpeter technique generates new poles within the band gap that correspond to excitonic peaks observed in the experimental spectrum, assigning them the appropriate weight and simultaneously redistributing the oscillator strength appropriately at higher energies. On the other hand, this is not the case for the LRC kernel. This can already be determined by inspecting the Cr_2O_3 results, as illustrated in the figure (8.17).

8.3.2 BSE spectra compared to RPA Bootstrap kernel, JGM kernel

Likewise, we compared the BSE spectrum to the TDDFT spectrum generated using the other two kernels (RPA bootstrap and JGM)in the figure (8.18).

The first thing we noticed is that the RPA bootstrap gives results closer to BSE than JGM in terms of the intensity of the initial peak. Whereas the second peak in both cases is quite dissimilar to the second peak of BSE. Both kernel spectra' second peaks are blueshifted compared to the BSE spectra's second peak. There is a noticeable variation in the estimated spectra when using the kernel and the BSE at high frequencies. Finally, the spectra estimated using both the kernel in the TDDFT framework do not contain any bound exciton peak.

8.4 Bethe Salpeter Equation spectra including spin-polarization

As seen in the section (7.2) concerning ground state properties, it is mandatory to introduce the spin-polarization, as it radically alters the Cr_2O_3's properties. We

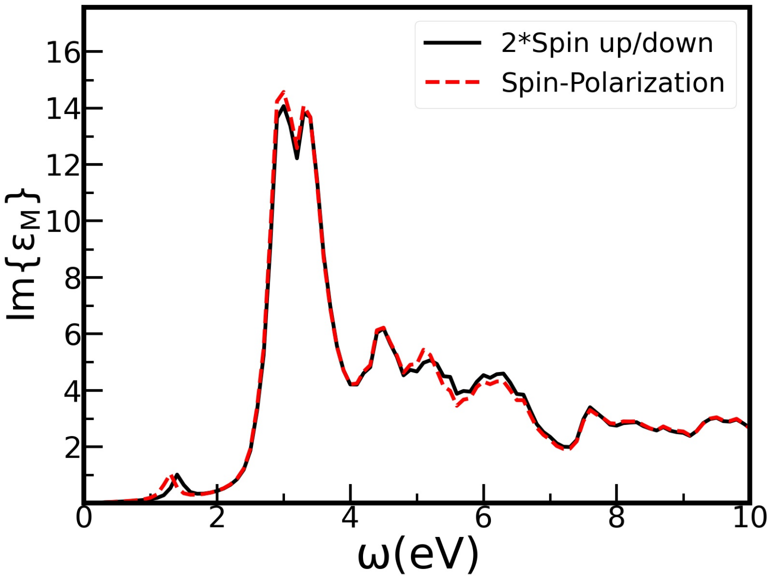

Figure 8.19: Effect of spin-polarization in the spectra calculated using BSE

have also seen that the optical properties are not dramatically modified, including or not the spin-polarization in TDDFT calculations. This section examines the influence of spin-polarization in the BSE spectra.

The figure (8.19) illustrates the effect of spin-polarization. As can be seen, incorporating spin-polarization at the BSE level has a minor effect, and the exciton peak is still present.

8.4.1 Calculation details

The BSE calculation is already computationally intensive; adding spin makes it even more complex to compute. To observe the influence of spin-polarization at the BSE level, the convergence parameter must be decreased.

As a result, the BSE spectra provided here may not exactly match the spectra shown in the preceding section (8.2).

The table (8.5) contains the value of the parameter that we utilized for these comparisons.

nband	npwmat	npwwfn	lomo
45	113	3000	15

Table 8.5: BSE converged parameters value

Where npwwfn defines the number of planewaves to describe wavefunctions, npwmat defines the G-vector needed to close the shell, related to the local field. Lomo denotes the number of the first band (lowest energy) to be included in the calculation.

Chapter 9

Exciton binding energy using Wannier-Mott model

In the previous chapter, we calculated the absorption spectra using the Bethe Salpeter equation (BSE). In the figure (8.14), we show that in the spectra calculated using BSE, there is a peak located at 1.3eV, which is absent from the spectra computed using RPA in TDDFT. We refer to this peak at 1.3eV as the excitonic peak. The difference between the excitonic and the GW band gap is referred to as the exciton's binding energy. This binding energy is equal to 1.38 eV, which is very large, indicating that the exciton present in the AFM Cr_2O_3 is a strongly bound exciton. To get more insight into the excitonic process and to interpret the results of the BSE calculation, we have used a simple analytical model, described in the reference [32]. This model, called the Wannier-Mott model, will be described in the section (9.1) and applied to the case of Cr_2O_3. We will also point out the difficulties we have encountered in the calculation of the binding energy.

9.1 Wannier-Mott model

The Wannier-Mott model is a simplification of the BSE in order to determine the excitonic binding energy. To begin with, we shall describe the creation of the exciton. When the light is incident on the material, a photon can be absorbed. The minimum energy absorbed by the material is equal to its band gap. An electron from the valence band is promoted into a conduction band and leaves a hole behind. The interaction between the electron and the hole strongly impacts the system, and we have to study the system taking into account the electron-hole pair as a particle. The electron-hole pair is referred to as an exciton, as seen in the diagram (9.1),

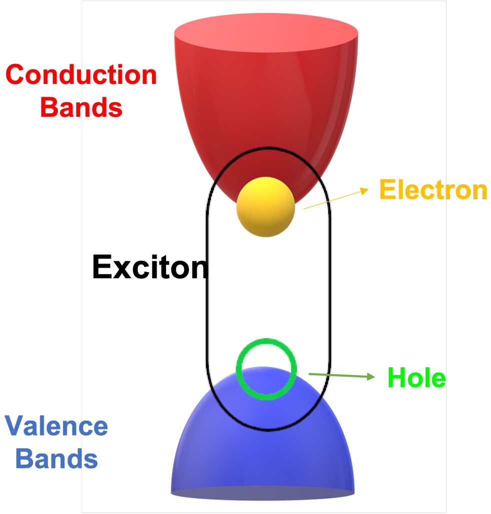

Figure 9.1: Exciton representation

The exciton is described by the Bethe Salpeter equation, which can be written as, [32],

$$\sum_{c^{'},v^{'}}\sum_{k^{'}} H(ck,vk|c^{'}k^{'},v^{'}k^{'})A_{\Lambda}(c^{'}k^{'},v^{'}k^{'}) = E_{\Lambda}A_{\Lambda}(ck,vk) \tag{9.1}$$

where, H denotes the electron-hole pair Hamiltonian, c denotes the conduction bands, v denotes the valence bands, k denotes the k-points. Equation (9.1) is an eigenvalue equation where A_{Λ} is the wave-function and E_{Λ} is the energy eigenvalue. To simplify this equation, we will consider only a two-band model, modelling a semiconductor, as described in the picture (9.2).

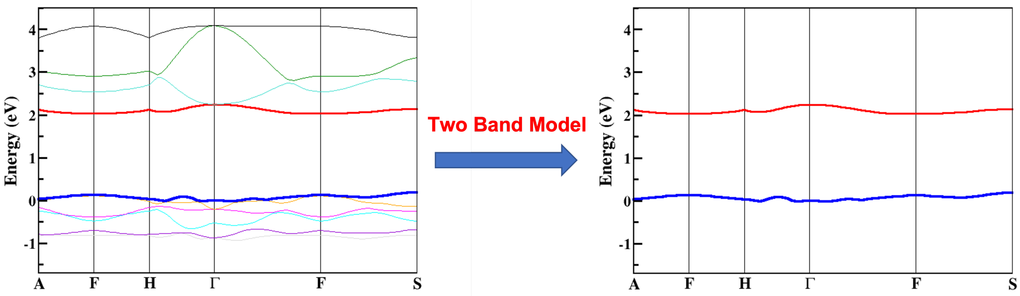

Figure 9.2: Two band model representation

In that case, the Hamiltonian in equation (9.1) can be written as,

$$H(ck,vk|ck',vk') = (E_{ck}-E_{vk})\delta_{kk'}\delta_{cc'}\delta_{vv'} - W(ck,vk|c'k',v'k') + 2\bar{v}(ck,vk|c'k',v'k') \tag{9.2}$$

Where W is the screened Coulomb potential and $\bar{v}$ is the bare Coulomb potential.

If the bands are isotropic and parabolic, they can be described within the effective mass approximation. Within this approximation, the electron-hole exchange vanish(i.e $\bar{v}$ =0) and,

$$E_c(k) = E_g + \frac{\hbar^2}{2m_c^*}k^2 \qquad E_v(k) = -\frac{\hbar^2}{2m_v^*}k^2 \tag{9.3}$$

If the band extrema are located at the same position (same k-point), then

$$E_c(k) - E_v(k) = E_g + \frac{\hbar^2}{2\mu_{ex}}k^2 \tag{9.4}$$

where the reduced effctive mass is defined as

$$\frac{1}{\mu_{ex}} = \frac{1}{m_c^*} + \frac{1}{m_v^*} \tag{9.5}$$

Hence we can write the Hamiltonian in the Wannier-Mott model as,

$$H^{WM}(k,k') = [E_g + \frac{\hbar^2}{2\mu_{ex}}k^2]\delta_{kk'} - \frac{1}{\Omega}\epsilon^{-1}(k-k',k-k',0)\tilde{v}(|k-k'|) \tag{9.6}$$

ϵ is the dielectric function, and Ω is the crystal volume. In the following, the wave-vector dispersion of the inverse dielectric constant will be neglected, and ϵ will be taken as the constant ϵ_∞.

The Hamiltonian (9.6) is,

$$H^{WM}(k,k') = [E_g + \frac{\hbar^2}{2\mu_{ex}}k^2]\delta_{kk'} - \frac{1}{\Omega\epsilon_\infty}\tilde{v}(|k-k'|) \tag{9.7}$$

and the eigenvalue equation becomes

$$\sum_{k'} H^{WM}(k,k')A_\Lambda(k') = E_\Lambda A_\Lambda(k) \tag{9.8}$$

Fourier transforms the eigenvalue equation; we get a Schrödinger-like equation,

$$\{E_g - \frac{\hbar^2}{2\mu_{ex}}\nabla_R^2 - \frac{1}{\epsilon_\infty}v(R)\}\Phi_\Lambda(R) = E_\Lambda\Phi_\Lambda(R) \tag{9.9}$$

which is similar to the hydrogen atom eigenvalue problem with the three modifications:

- a shift of the ionization energy by E_g.
- a reduced mass μ_{ex} of the particle instead of the free electron mass m.
- the fictitious proton charge is reduced to the value $1/\epsilon_\infty$ by the screening.

The eigenvalue equation can then be solved and the result is expressed in terms of the scaled Rydberg energy,

$$R_{ex} = \frac{R_{\infty}\mu_{ex}}{\epsilon_{\infty}^{2}} \tag{9.10}$$

The energy eigenvalues are given by,

$$E_{nlm} = E_g - \frac{R_{ex}}{n^2} \tag{9.11}$$

and

$$E_B = \frac{R_{ex}}{n^2} \tag{9.12}$$

is the exciton binding energy of the system.

9.2 Application of Wannier-Mott Model to calculate the excitonic binding energy

The flow chart (9.3) illustrates the procedure for calculating the exciton binding energy. The key quantity for the calculation of E_B are the effective masses of conduction and valence bands (i.e $E_c(k)$ and $E_v(k)$). Once they have been obtained, we can calculate the reduced mass described as the second step in the flow chart. This allows us to determine the R_{ex} value, which is required for the computation of the excitonic binding energy.

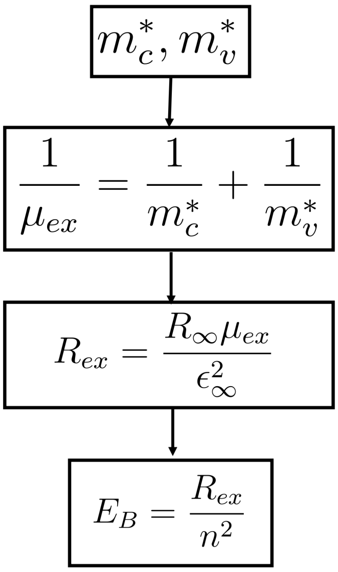

Figure 9.3: Flow chart for excitonic binding energy

9.3 Effective mass calculations

The energy of a band can be written at an extremum $\mathbf{k}_0$ as,

$$
\begin{aligned}
E(\mathbf{k}) &= E_(\mathbf{k}_0) + \frac{1}{2}\sum_{ij}\frac{\partial^2 E}{\partial k_i \partial k_j}\Delta k_i \Delta k_j \\
&= E(\mathbf{k}_0) + \frac{1}{2}\left[\frac{\partial^2 E}{\partial k_x^2}\Delta k_x^2 + \frac{\partial^2 E}{\partial k_y^2}\Delta k_y^2 + \frac{\partial^2 E}{\partial k_z^2}\Delta k_z^2\right. \\
&\left. +2\frac{\partial^2 E}{\partial k_x \partial k_y}\Delta k_x \Delta k_y + 2\frac{\partial^2 E}{\partial k_x \partial k_z}\Delta k_x \Delta k_z + 2\frac{\partial^2 E}{\partial k_y \partial k_z}\Delta k_y \Delta k_z\right]
\end{aligned}
\tag{9.13}
$$

The effective masses are defined as

$$
\frac{1}{m_{ij}} = \frac{\partial^2 E}{\partial k_i \partial k_j} \tag{9.14}
$$

and the effective mass tensor can be written as

$$
\frac{1}{M} = \begin{pmatrix} \frac{d^2E}{dk_x^2} & \frac{d^2E}{dk_x dk_y} & \frac{d^2E}{dk_x dk_z} \\ \frac{d^2E}{dk_x dk_y} & \frac{d^2E}{dk_y^2} & \frac{d^2E}{dk_y dk_z} \\ \frac{d^2E}{dk_x dk_z} & \frac{d^2E}{dk_y dk_z} & \frac{d^2E}{dk_z^2} \end{pmatrix} = \begin{pmatrix} \frac{1}{m_{xx}} & \frac{1}{m_{xy}} & \frac{1}{m_{xz}} \\ \frac{1}{m_{yx}} & \frac{1}{m_{yy}} & \frac{1}{m_{yz}} \\ \frac{1}{m_{zx}} & \frac{1}{m_{zy}} & \frac{1}{m_{zz}} \end{pmatrix} \tag{9.15}
$$

For isotropic material the tensor is diagonal, the effective masses $\frac{1}{m_{ii}}$ are the same in all directions, and only one calculation is needed. The bandstructure is accurately calculated around the point $\mathbf{k}_0$, and the effective mass is obtained using a parabolic fit.

In the general case the calculation of the effective mass tensor is more involved. $\mathrm{Cr_2O_3}$ is an anisotropic material, and several directions have to be considered for the fitting procedure.

9.4 Effective mass for the $\mathrm{Cr_2O_3}$

Effective mass: Conduction band First, we calculated the effective mass of the conduction band ($\frac{1}{m_c^*}$). In principle, for an anisotropic material, we need to calculate all the matrix elements in (9.15) and diagonalize it to determine the eigenvalues $\frac{1}{m_i}$ and the eigenvectors. To simplify further the calculation, we consider an average effective mass as,

$$
\frac{3}{\bar{m}} = \frac{1}{m_1} + \frac{1}{m_2} + \frac{1}{m_3} \tag{9.16}
$$

Using the invariance of the trace of the symmetric tensor M, only 3 directions are needed for the calculation, i.e

$$
\frac{3}{\bar{m}} = \frac{1}{m_{xx}} + \frac{1}{m_{yy}} + \frac{1}{m_{zz}} = \frac{1}{m_1} + \frac{1}{m_2} + \frac{1}{m_3} \tag{9.17}
$$

Fitting the conduction band along the cartesian coordinates x, y and z at point F, we get,

$$\begin{aligned} \frac{1}{m_{xx}} &= \frac{\partial^2 E}{\partial k_x^2} = 0.480 \\ \frac{1}{m_{yy}} &= \frac{\partial^2 E}{\partial k_y^2} = 0.374 \\ \frac{1}{m_{zz}} &= \frac{\partial^2 E}{\partial k_z^2} = 0.216 \end{aligned} \tag{9.18}$$

and the average effective mass is $\frac{1}{m_c^*} = 0.357$

Effective mass : Valence band We perform the same set of calculations for the F point for the valence band, and we get,

$$\frac{1}{m_x x} = \frac{1}{m_y y} = 0.262 \qquad \frac{1}{m_z z} = 0.522 \tag{9.19}$$

The average value is $\frac{1}{m_v^*} = 0.349$

9.5 Exciton binding energy

With the obtained values for m_c^* and m_v^* the reduced mass is

$$\frac{1}{\mu_{ex}} = \frac{1}{m_c^*} + \frac{1}{m_v^*} = 0.706 \tag{9.20}$$

and the binding energy for the exciton for Cr_2O_3 is approximated by

$$E_B = R_\infty \frac{\mu_{ex}}{m\epsilon_\infty^2} = 0.5eV \tag{9.21}$$

where we used, $\epsilon_\infty = 6.2$ [71].

The binding energy calculated using equation (9.21) is underestimated as compared to the binding energy calculated using BSE (E_B=1.38eV).

Although this model does not provide a precise estimation for the binding energy of Cr_2O_3, it indicates the presence of a bound exciton in the gap, as observed in the BSE calculation. Because this model is relatively simple in comparison to the whole BSE computation, we may still consider it as a suitable model for computing the binding energy despite the low accuracy in this case.

This model has been used for several semiconductors and has shown an excellent agreement with the BSE calculation for E_B when continuum excitons were involved., as shown in reference [32].

We considered several explanations for the observed discrepancy in the case of Cr_2O_3 :

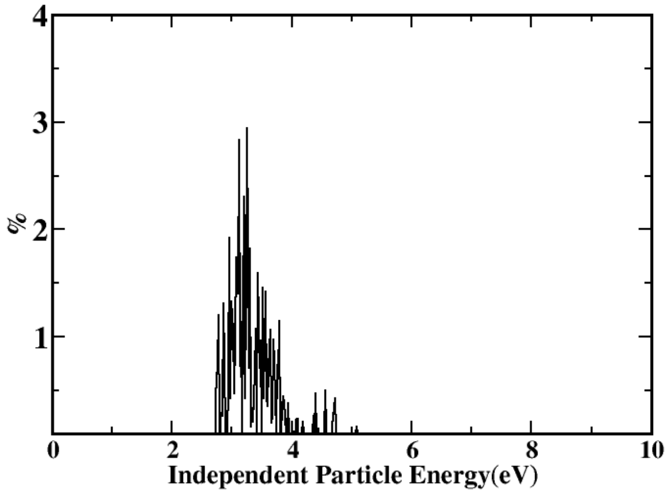

Figure 9.4: Transition plot for the excitonic peak

1. We considered a two-band model, but additional bands can contribute to the building of the exciton. To address this question, we determined the number of transitions contributing to the excitonic peak using equation (6.28), discussed in the chapter (6). As illustrated in the figure (9.4), the excitonic peak results from the contribution of several transitions in terms of band index. This suggests that a large number of bands contribute to the excitonic peak. As a result, we may speculate that the excitonic binding energy is not as high as it should be using this model.

2. In calculating the binding energy, we have used the static dielectric constant. This quantity comes from two contributions: the electronic and the ionic, but we have only evaluated the electronic contribution, which might lead to incorrect results. Note that the ionic contribution can be either positive or negative depending on the material.

3. The last argument we could come up with is linked to the bandstructure itself. The model has been derived for materials with a direct gap, which is not the case of Cr_2O_3. However, we have considered that this approximation could be satisfied due to the flatness of the bands.

Chapter 10

Second-order response function

In this chapter, we derive the second-order response function for Second Harmonic Generation (SHG), in terms of spin-polarization (10.1.1). SHG spectra are calculated and discussed using various approximations for the xc kernels. We also derive and discuss a new kernel for Cr_2O_3 based on the Bethe Salpeter equation. Finally, we analyze the effects of the semicore electrons pseudo-potential on the second-harmonic spectra.

10.1 Second-order response function

An ab-initio formalism for the calculation of macroscopic second-order responses within the framework of TDDFT has been presented in the article [25], and corresponds to the state of the art at the beginning of my work for second harmonic generation . In this chapter, we will show how it can be extended to include the spin-polarization.

10.1.1 Second-order response function including spin-polarization

While the second-order response function has already been calculated for a large set of non-magnetic materials, the effect of spin polarization on second harmonic generation is not widely documented. In particular, although it is known that SHG can occur in antiferromagnetic materials because the spin polarization breaks the centro-symmetry, few calculations have been performed in this case, see however ref [1] and references therein. In the following, we present our extension to the spin-polarised case for the second-order calculation. This extension has been implemented in the *2light* code.

For the sake of simplicity, all the quantities will be written explicitly with the spin variables; all the others, such as reciprocal space vectors and frequencies, are implicit. The two kernels f_{xc} and g_{xc} are defined by

$$f_{xc}^{\alpha\beta} = \frac{\delta V_{xc}^{\alpha}}{\delta n^{\beta}} \qquad g_{xc}^{\alpha\beta\gamma} = \frac{\delta^2 V_{xc}^{\alpha}}{\delta n^{\beta} \delta n^{\gamma}} \tag{10.1}$$

where α, β and γ denotes the spin (↑ or ↓).

The second-order contributions to the effective potential and to the induced density are given by

$$V^{(2)\alpha} = \sum_{\beta} f_{uxc}^{\alpha\beta} n^{(2)\beta} + \frac{1}{2} \sum_{\beta\gamma} g_{xc}^{\alpha\beta\gamma} n^{(1)\beta} n^{(1)\gamma} \tag{10.2}$$

$$n^{(2)\alpha} = \sum_{\alpha} \chi_0^{(1)\alpha\beta} V^{(2)\beta} + \frac{1}{2} \sum_{\beta\gamma} \chi_0^{(2)\alpha\beta\gamma} V^{(1)\beta} V^{(1)\gamma} \tag{10.3}$$

Taking equations (10.3) and (10.2) together, the induced density is

$$\begin{aligned} n^{(2)\alpha} = & \sum_{\beta\gamma} \chi_0^{(1)\alpha\beta} f_{uxc}^{\beta\gamma} n^{(2)\gamma} + \frac{1}{2} \sum_{\beta\gamma\delta} \chi_0^{(1)\alpha\beta} g_{xc}^{\beta\gamma\delta} n^{(1)\gamma} n^{(1)\delta} \\ & + \frac{1}{2} \sum_{\beta\gamma\delta\epsilon} \chi_0^{(2)\alpha\beta\gamma} \left[V_{ext}^{(1)\beta} + f_{uxc}^{\beta\delta} n^{(1)\delta} \right] \left[V_{ext}^{(1)\gamma} + f_{uxc}^{\gamma\epsilon} n^{(1)\epsilon} \right] \end{aligned} \tag{10.4}$$

Using the definition of $\chi^{(2)}$ and $\chi^{(1)}$ in terms of the external potential

$$n^{(2)\alpha} = \frac{1}{2} \sum_{\beta\gamma} \chi^{(2)\alpha\beta\gamma} V_{ext}^{(1)\beta} V_{ext}^{(1)\gamma} \qquad n^{(1)\alpha} = \sum_{\beta} \chi^{(1)\alpha\beta} V_{ext}^{(1)\beta} \tag{10.5}$$

and after some tedious calculations similar to the case presented in section (4.2.4) the relation between $\chi^{(2)}$, $\chi_0^{(2)}$ and $\chi^{(1)}$ is

$$\begin{aligned} \chi^{(2)\alpha\beta\gamma} = & \chi_0^{(2)\alpha\beta\gamma} + \sum_{\delta\epsilon} \chi_0^{(1)\alpha\delta} f_{uxc}^{\delta\epsilon} \chi^{(2)\epsilon\beta\gamma} + \sum_{\mu\nu\delta} \chi_0^{(1)\alpha\mu} g_{xc}^{\mu\nu\delta} \chi^{(1)\nu\beta} \chi^{(1)\delta\gamma} \\ & + \sum_{\epsilon\mu} \chi_0^{(2)\alpha\beta\mu} f_{uxc}^{\mu\epsilon} \chi^{(1)\epsilon\gamma} + \sum_{\delta\nu} \chi_0^{(2)\alpha\nu\gamma} f_{uxc}^{\nu\delta} \chi^{(1)\delta\beta} + \sum_{\delta\epsilon\mu\nu} \chi_0^{(2)\alpha\mu\nu} f_{uxc}^{\mu\delta} \chi^{(1)\delta\beta} f_{uxc}^{\nu\epsilon} \chi^{(1)\epsilon\gamma} \end{aligned} \tag{10.6}$$

Eight components can be defined, such as $\chi^{(2)\alpha\alpha\alpha}$, $\chi^{(2)\beta\alpha\alpha}$, $\chi^{(2)\alpha\beta\alpha}$, and considering first, the two equations satisfied by the components $\chi^{(2)\alpha\alpha\alpha}$ and , $\chi^{(2)\beta\alpha\alpha}$, we get the following matrix equation,

$$\begin{aligned} \begin{pmatrix} \chi^{(2)\alpha\alpha\alpha} \\ \chi^{(2)\beta\alpha\alpha} \end{pmatrix} - M \begin{pmatrix} \chi^{(2)\alpha\alpha\alpha} \\ \chi^{(2)\beta\alpha\alpha} \end{pmatrix} = & \\ \begin{pmatrix} \sum_{\mu\nu} \chi_0^{(2)\alpha\nu\mu} \left[\delta_{\alpha\nu} + \sum_{\delta} f_{uxc}^{\nu\delta} \chi^{(1)\delta\alpha}\right] \left[\delta_{\alpha\mu} + \sum_{\epsilon} f_{uxc}^{\mu\epsilon} \chi^{(1)\epsilon\alpha}\right] \\ \sum_{\mu\nu} \chi_0^{(2)\beta\nu\mu} \left[\delta_{\alpha\nu} + \sum_{\delta} f_{uxc}^{\nu\delta} \chi^{(1)\delta\alpha}\right] \left[\delta_{\mu\alpha} + \sum_{\epsilon} f_{uxc}^{\mu\epsilon} \chi^{(1)\epsilon\alpha}\right] \end{pmatrix} & \\ + \begin{pmatrix} \chi_0^{(1)\alpha\mu} g_{xc}^{\mu\nu\delta} \chi^{(1)\nu\alpha} \chi^{(1)\delta\alpha} \\ + \chi_0^{(1)\beta\mu} g_{xc}^{\mu\nu\delta} \chi^{(1)\nu\alpha} \chi^{(1)\delta\alpha} \end{pmatrix} & \end{aligned}$$

with

$$M = \begin{pmatrix} \chi_0^{(1)\alpha\delta} f_{uxc}^{\delta\alpha} & \chi_0^{(1)\alpha\delta} f_{uxc}^{\delta\beta} \\ \chi_0^{(1)\beta\delta} f_{uxc}^{\delta\alpha} & \chi_0^{(1)\beta\delta} f_{uxc}^{\delta\beta} \end{pmatrix}$$

where the summation over the repeated index δ is implicit.

We have also for the other components

$$\begin{pmatrix} \chi^{(2)\alpha\beta\alpha} \\ \chi^{(2)\beta\beta\alpha} \end{pmatrix} - M\begin{pmatrix} \chi^{(2)\alpha\beta\alpha} \\ \chi^{(2)\beta\beta\alpha} \end{pmatrix} =$$

$$\begin{pmatrix} \sum_{\mu\nu} \chi_0^{(2)\alpha\nu\mu} \left[\delta_{\beta\nu} + \sum_\delta f_{uxc}^{\nu\delta}\chi^{(1)\delta\beta}\right] \left[\delta_{\alpha\mu} + \sum_\epsilon f_{uxc}^{\mu\epsilon}\chi^{(1)\epsilon\alpha}\right] \\ \sum_{\mu\nu} \chi_0^{(2)\beta\nu\mu} \left[\delta_{\beta\nu} + \sum_\delta f_{uxc}^{\nu\delta}\chi^{(1)\delta\beta}\right] \left[\delta_{\alpha\mu} + \sum_\epsilon f_{uxc}^{\mu\epsilon}\chi^{(1)\epsilon\alpha}\right] \end{pmatrix}$$

$$+\begin{pmatrix} \chi_0^{(1)\alpha\mu} g_{xc}^{\mu\nu\delta}\chi^{(1)\nu\beta}\chi^{(1)\delta\alpha} \\ \chi_0^{(1)\beta\mu} g_{xc}^{\mu\nu\delta}\chi^{(1)\nu\beta}\chi^{(1)\delta\alpha} \end{pmatrix}$$

$$\begin{pmatrix} \chi^{(2)\alpha\alpha\beta} \\ \chi^{(2)\beta\alpha\beta} \end{pmatrix} - M\begin{pmatrix} \chi^{(2)\alpha\alpha\beta} \\ \chi^{(2)\beta\alpha\beta} \end{pmatrix} =$$

$$\begin{pmatrix} \sum_{\mu\nu} \chi_0^{(2)\alpha\nu\mu} \left[\delta_{\nu\alpha} + \sum_\delta f_{uxc}^{\nu\delta}\chi^{(1)\delta\alpha}\right] \left[\delta_{\mu\beta} + \sum_\epsilon f_{uxc}^{\mu\epsilon}\chi^{(1)\epsilon\beta}\right] \\ \sum_{\mu\nu} \chi_0^{(2)\beta\nu\mu} \left[\delta_{\nu\alpha} + + \sum_\delta f_{uxc}^{\nu\delta}\chi^{(1)\delta\alpha}\right] \left[\delta_{\mu\beta} + \sum_\epsilon f_{uxc}^{\mu\epsilon}\chi^{(1)\epsilon\beta}\right] \end{pmatrix}$$

$$+\begin{pmatrix} \chi_0^{(1)\alpha\mu} g_{xc}^{\mu\nu\delta}\chi^{(1)\nu\alpha}\chi^{(1)\delta\beta} \\ \chi_0^{(1)\beta\mu} g_{xc}^{\mu\nu\delta}\chi^{(1)\nu\alpha}\chi^{(1)\delta\beta} \end{pmatrix}$$

$$\begin{pmatrix} \chi^{(2)\alpha\beta\beta} \\ \chi^{(2)\beta\beta\beta} \end{pmatrix} - M\begin{pmatrix} \chi^{(2)\alpha\beta\beta} \\ \chi^{(2)\beta\beta\beta} \end{pmatrix} =$$

$$\begin{pmatrix} \sum_{\mu\nu} \chi_0^{(2)\alpha\nu\mu} \left[\delta_{\beta\nu} + \sum_\delta f_{uxc}^{\nu\delta}\chi^{(1)\delta\beta}\right] \left[\delta_{\beta\mu} + \sum_\epsilon f_{uxc}^{\mu\epsilon}\chi^{(1)\epsilon\beta}\right] \\ \sum_{\mu\nu} \chi_0^{(2)\beta\nu\mu} \left[\delta_{\beta\nu} + \sum_\delta f_{uxc}^{\nu\delta}\chi^{(1)\delta\beta}\right] \left[\delta_{\beta\mu} + \sum_\epsilon f_{uxc}^{\mu\epsilon}\chi^{(1)\epsilon\beta}\right] \end{pmatrix}$$

$$+\begin{pmatrix} \chi_0^{(1)\alpha\mu} g_{xc}^{\mu\nu\delta}\chi^{(1)\nu\beta}\chi^{(1)\delta\beta} \\ \chi_0^{(1)\beta\mu} g_{xc}^{\mu\nu\delta}\chi^{(1)\nu\beta}\chi^{(1)\delta\beta} \end{pmatrix}$$

Summing up the 4 matrix equations and using the definitions $\chi^{(1)\beta} = \sum_\nu \chi^{(1)\nu\beta}$, we have

$$\begin{pmatrix} \chi^{(2)\alpha\alpha\alpha} + \chi^{(2)\alpha\beta\alpha} + \chi^{(2)\alpha\alpha\beta} + \chi^{(2)\alpha\beta\beta} \\ \chi^{(2)\beta\alpha\alpha} + \chi^{(2)\beta\beta\alpha} + \chi^{(2)\beta\alpha\beta} + \chi^{(2)\beta\beta\beta} \end{pmatrix} - M\begin{pmatrix} \chi^{(2)\alpha\alpha\alpha} + \chi^{(2)\alpha\beta\alpha} + \chi^{(2)\alpha\alpha\beta} + \chi^{(2)\alpha\beta\beta} \\ \chi^{(2)\beta\alpha\alpha} + \chi^{(2)\beta\beta\alpha} + \chi^{(2)\beta\alpha\beta} + \chi^{(2)\beta\beta\beta} \end{pmatrix} =$$

$$\begin{pmatrix} \sum_{\mu\nu} \chi_0^{(2)\alpha\nu\mu} \left[\delta_{\alpha\nu} + \delta_{\beta\nu} + \sum_\delta f_{uxc}^{\nu\delta}\chi^{(1)\delta}\right] \left[\delta_{\alpha\mu} + \delta_{\mu\beta} + \sum_\epsilon f_{uxc}^{\mu\epsilon}\chi^{(1)\epsilon}\right] \\ \sum_{\mu\nu} \chi_0^{(2)\beta\nu\mu} \left[\delta_{\alpha\nu} + \delta_{\beta\nu} + \sum_\delta f_{uxc}^{\nu\delta}\chi^{(1)\delta}\right] \left[\delta_{\mu\alpha} + \delta_{\mu\beta} + \sum_\epsilon f_{uxc}^{\mu\epsilon}\chi^{(1)\epsilon}\right] \end{pmatrix}$$

$$+\begin{pmatrix} \sum_{\mu\nu\delta} \chi_0^{(1)\alpha\mu} g_{xc}^{\mu\nu\delta}\chi^{(1)\nu}\chi^{(1)\delta} \\ \sum_{\mu\nu\delta} \chi_0^{(1)\beta\mu} g_{xc}^{\mu\nu\delta}\chi^{(1)\nu}\chi^{(1)\delta} \end{pmatrix}$$

As $\chi_0^{(1)}$ and $\chi_0^{(2)}$ are spin-diagonal, we have finally

$$\begin{pmatrix} \chi^{(2)\alpha} \\ \chi^{(2)\beta} \end{pmatrix} - M\begin{pmatrix} \chi^{(2)\alpha} \\ \chi^{(2)\beta} \end{pmatrix} =$$

$$+\begin{pmatrix} \chi_0^{(2)\alpha\alpha\alpha} \left[1 + \sum_\delta f_{uxc}^{\alpha\delta}\chi^{(1)\delta}\right] \left[1 + \sum_\epsilon f_{uxc}^{\alpha\epsilon}\chi^{(1)\epsilon}\right] \\ \chi_0^{(2)\beta\beta\beta} \left[1 + \sum_\delta f_{uxc}^{\beta\delta}\chi^{(1)\delta}\right] \left[1 + \sum_\epsilon f_{uxc}^{\beta\epsilon}\chi^{(1)\epsilon}\right] \end{pmatrix} + \begin{pmatrix} \sum_{\nu\delta} \chi_0^{(1)\alpha\alpha} g_{xc}^{\alpha\nu\delta}\chi^{(1)\nu}\chi^{(1)\delta} \\ \sum_{\nu\delta} \chi_0^{(1)\beta\beta} g_{xc}^{\beta\nu\delta}\chi^{(1)\nu}\chi^{(1)\delta} \end{pmatrix}$$

where we have defined two new response functions,

$$\begin{aligned}\chi^{(2)\alpha} &= \chi^{(2)\alpha\alpha\alpha} + \chi^{(2)\alpha\beta\alpha} + \chi^{(2)\alpha\alpha\beta} + \chi^{(2)\alpha\beta\beta}\\ \chi^{(2)\beta} &= \chi^{(2)\beta\alpha\alpha} + \chi^{(2)\beta\beta\alpha} + \chi^{(2)\beta\alpha\beta} + \chi^{(2)\beta\beta\beta}\end{aligned} \tag{10.7}$$

Note also that, as $\chi_0^{(1)}$ is diagonal in spin, the matrix M defined in Eq.(10.7) is the same as the one defined for the linear spin-dependent case.

As for the linear case, the external potential does not depend on the spin $V_{ext}^{(1)\alpha} = V_{ext}^{(1)\beta} = V_{ext}^{(1)}$ and with $V_{ext}^{(2)} = 0$, we get

$$n^{(2)} = n^{(2)\uparrow} + n^{(2)\downarrow} = \frac{1}{2}\sum_{\alpha\beta\gamma} \chi^{(2)\alpha\beta\gamma} V_{ext}^{(1)} V_{ext}^{(1)} \tag{10.8}$$

The final result of this section is the definition of a total response function, defined as

$$\chi^{(2)} = \sum_{\alpha\beta\gamma} \chi^{(2)\alpha\beta\gamma} \tag{10.9}$$

where all intermediate spin-dependent components satisfy, two by two, a matrix Dyson equation.

10.1.2 Implementation

In this subsection, we present the main modifications done in the code *2light*.

- In the original version of *2light*, the response functions $\chi_0^{(1)}$, $\chi^{(1)}$, $\chi_0^{(2)}$ and $\chi^{(2)}$ depend on the frequency and on the vectors $\mathbf{q}+\mathbf{G}$. They no depend on the spin-component ↑ or ↓. New definitions for all the quantities related to spin have been implemented.

- The subroutine dedicated to the solution of the Dyson equation has been modified to account for the spin.

- Some of the exchange correlation kernels depend explicitly on the spin-component and have been adapted (ALDA for instance). In the case of scalar kernels, such as the alpha-kernel, they correspond to spatial average densities and for antiferromagnetic materials they are identical for ↑ or ↓.

Numerical checks have been performed. Concerning the implementation of the Dyson equation, we have compared our results for first-order quantities ($\chi_0^{(1)}$ and $\chi^{(1)}$) to the quantities obtained with the DP code.

10.2 Second-order response of Cr_2O_3

In the dipole approximation, SHG is a second-order nonlinear optical phenomenon that is forbidden in a material with inversion-symmetry. Because of sensitivity to the symmetry of the material, it is commonly used in the study of interfaces and surfaces, where inversion symmetry is inevitably broken. Despite the fact that Cr_2O_3 is centrosymmetric, its symmetry has been disrupted by the spin structure. As a result, SHG occurs. In this chapter, we study the SHG of Cr_2O_3.

A second-order response function describes the SHG process, which is detailed in the section (4.2.5).

The TDDFT calculations of linear optical properties with LRC kernel produce satisfactory results [60]. Similarly, it has been observed that the ab-initio approach is quite successful in describing nonlinear optical processes for simple materials, e.g. SiC, AlAs [25, 72].

In the subsequent sections, we will discuss the relevance of the two effects (crystal local-field and excitonic effects) on the second-order response function of Cr_2O_3, when spin-polarization is taken into account. We will first discuss the second-harmonic generation spectra for the Cr_2O_3, starting with the independent-particle approximation for $\chi^{(2)}$. We will discuss the crystal local field effects (RPA), and finally, we will discuss the excitonic effect by using different xc kernels in the calculations. We will show how the different levels of approximation affect the result of second harmonic spectra of Cr_2O_3. As for the linear case, all these studies will be performed in the quasiparticle framework, where we will use a scissor correction derived from the GW calculation presented in section (5.7).

10.2.1 Calculations details

To calculate the second-order spectra we first have to perform the ground state DFT calculations. We determine the electronic structure of the material in the ground state with DFT in the LDA, using norm-conserving pseudopotential [73] and plane-wave basis set with the ABINIT code [43]. The kpoint grid 4 4 4 is used in this case.

For the calculation of the nonlinear optical spectra, we use the nonlinear-response code named *2light*. The values for the parameters used in the second-order calculations of Cr_2O_3 are given in the table 10.1. The convergence in terms of the number of bands is described in the appendix (C).

nbands	npwmat	npwwfn
200	59	2500

Table 10.1: Converged parameters value in second-order response function calculations

The significance of these parameters has been described in the section (8.1.1). The scissor value is 0.73eV. Despite recent advances in computational resources, the ab-initio calculation of Second-Harmonic Generation (SHG) in solids remains a significant technical challenge. Convergence calculation requires a significant amount of time and computational resources.

The convergence parameter's value remains constant throughout the chapter unless otherwise specified. Also, all calculations are performed using the valence electrons pseudopotentials unless otherwise specified. We have studied two components of the second-order response function (xxx and zzz), which are non-zero for Cr_2O_3. Unless otherwise specified, we address the xxx component.

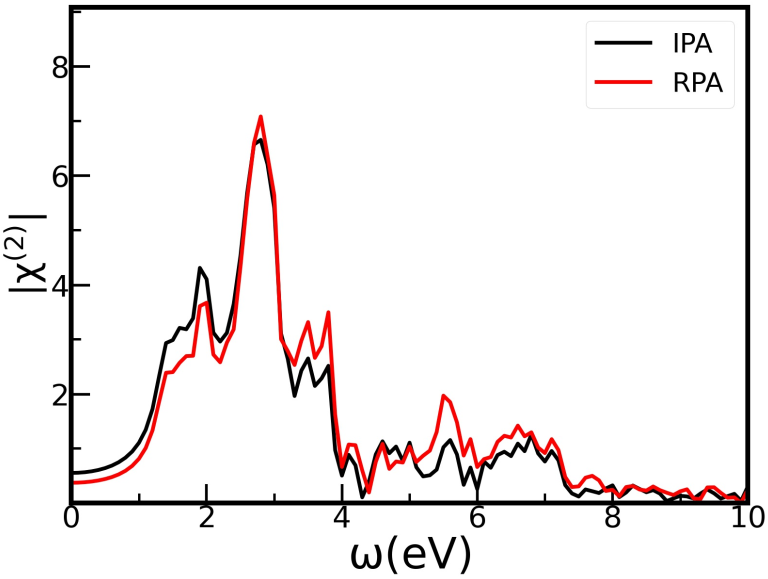

Figure 10.1: Second-order response function using IPA and RPA

10.2.2 Second-order response using IPA and RPA

The IPA is the simplest approximation for computing the second-order response from a computational standpoint. However, it has been observed that within this approximation, the second-order susceptibility deviates significantly from experimental data, [74] and we have to consider alternatives to the IPA.

In order to go beyond the independent particle description, we will consider the inhomogeneity of the electron density, which causes a variation of the screening fields on the microscopic scale, i.e. the local field effects [75]. In the RPA, we solve the Dyson equation presented in the previous section with the kernels $f_{xc} = 0$ and $g_{xc} = 0$.

In figure (10.1), we present the results of the IPA and RPA calculations, including quasiparticle corrections via the scissors operator. The local fields have an overall effect of decreasing the low frequency range amplitude of the second-order susceptibility spectra relative to IPA without strongly altering the spectra' shape. This is general feature, that has already been evidenced in article [25], for the case of several semiconductors GaAs, AlAs, and SiC. In the present case, the spectrum is only slightly changed compared to IPA.

We conclude here that, whereas local-field effects are required for a rigorous description, in theory, they contribute only to a modest amount to the spectrum.

10.2.3 Effect of spin-polarization in second-order response using RPA approximation

The independent particle response function $\chi_0^{(2)}$ can be written as the sum of two terms

$$\chi_0^{(2)} = \chi_0^{(2)\uparrow} + \chi_0^{(2)\downarrow} \tag{10.10}$$

A simple way to consider the effect of spin-polarization on the second-order response function is to solve the Dyson equation using either $\chi_0^{(2)}$ defined by the

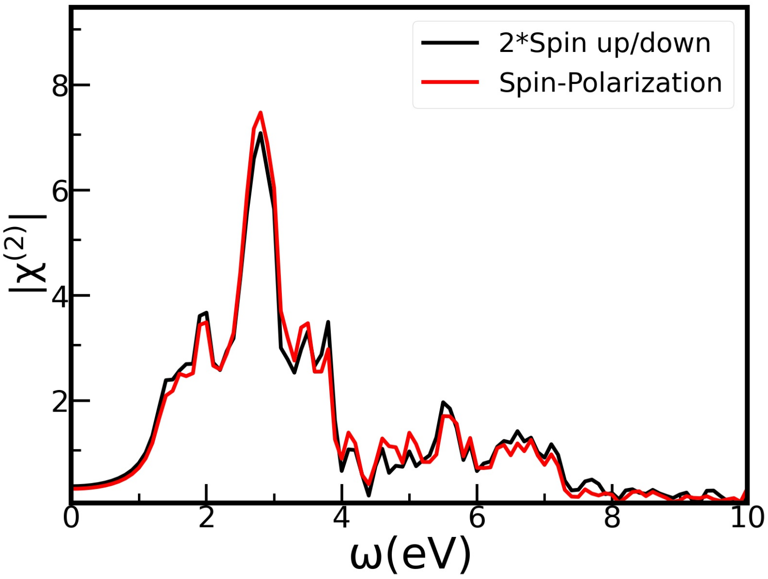

Figure 10.2: Effect of spin-polarization in second-order response using RPA approximation

previous equation or by $\chi_0^{(2)} = 2\chi_0^{(2)\uparrow}$. The result of these two calculations is shown in figure (10.2). It is clear that the effect is small, even smaller than the local fields. Note that this result can be used in a certain case, as the amount of computer time needed for the evaluation of the $\chi^{(2)}$ is strongly reduced (a factor 2) when neglecting the spin-polarization.

10.2.4 Second-order response function derived from the standard kernel

We investigated the local field impact within the RPA approximation solely. Additionally, because the SHG process generates virtual excitation states, the electron-hole interaction [38] must be included in $\chi^{(2)}$

Chang et al. [76] demonstrated that the combined influence of crystal local fields and excitonic effects increases the amount of second-order polarization in comparison to an independent-particle calculation, resulting in a satisfactory agreement with experimental evidence in the static limit. This was also evidenced in [75].

As previously stated in the section (8.1.4), the excitonic effect is incorporated into the TDDFT via the xc kernel and finding the appropriate exchange-correlation kernel is a critical issue.

Numerous kernels currently exist to describe the excitonic effect; some of them provide good results for the linear response of a wide variety of semiconductors, and their effect on Cr_2O_3 is discussed in section 8.1.4.

We present in the following the influence of the xc kernels on the second-order Cr_2O_3 spectra. Note that in the following, we will study only the influence of f_{xc}, the kernel g_{xc} is being kept to 0.

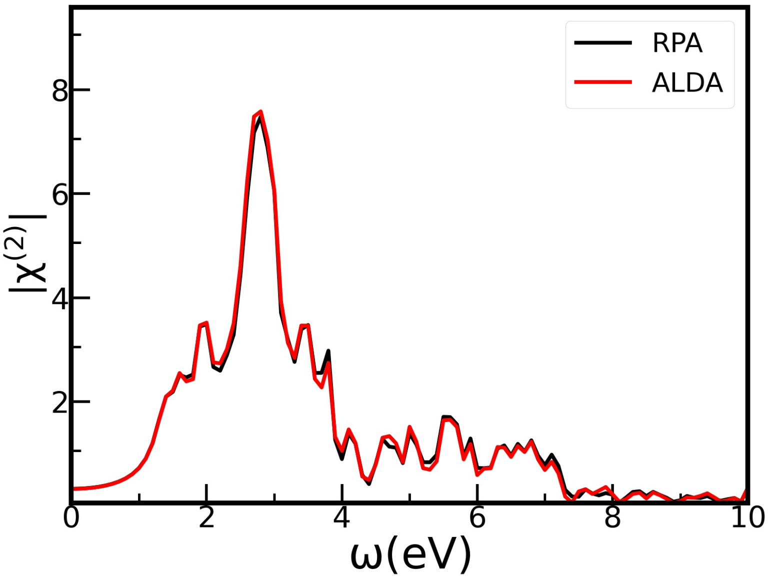

Figure 10.3: Second-order response function using LDA and RPA

Second-order response function calculated using ALDA

In the linear processes, the adiabatic local density approximation (ALDA) fails to describe the optical absorption due to the long-range aspect of the electron-hole interaction coming from the excitons, which are important in optical processes. Despite this fact, we have examined the influence of ALDA on the second-order spectra of Cr_2O_3.

The comparison of ALDA with the RPA is shown in the figure (10.3). We observe that the output is remarkably similar to that of RPA. This effect is even smaller than what has been obtained for the absorption spectra in Cr_2O_3 shown in figure 8.6.

Second-order response function calculated using long-range kernels

We first study the excitonic effect on the second harmonic generation of Cr_2O_3 using the α-kernel described in section (8.1.4). This kernel depends on a parameter, which is material-dependent and has to be determined. In the following, we use the value obtained in section (8.3.1) by comparing it with BSE results for the linear case. This comparison yields $\alpha = 0.33$.

The comparison between results obtained in RPA (where the exchange-correlation kernel is set to zero) and with the α-kernel is presented in figure (10.4). This comparison shows that excitonic effects have a significant influence on the second harmonic spectrum for Cr_2O_3. Compared to RPA, the α- kernel increased the peak amplitude by a factor of two at $\omega = 2.85$ eV. Note that this effect disappears at high frequencies, where the two calculations yield the same results.

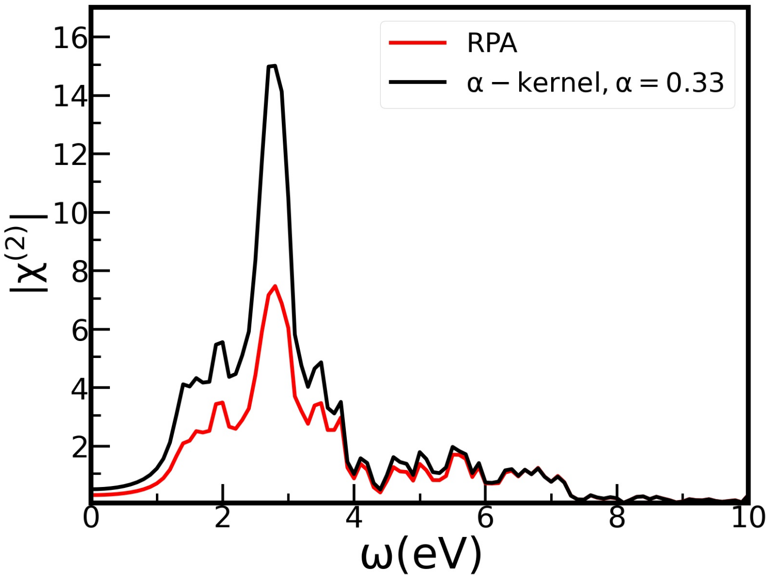

Figure 10.4: Second-order response function using RPA and alpha-kernel

10.2.5 Comparison of different component of second-order response function of Cr_2O_3

We have already pointed out that two components of the second-order response functions of Cr_2O_3 are non-zero. Here we compare these two components in the figure (10.5). As can be seen, the two components are quite different. The two second-order peaks are distinct for the component zzz, as shown in the figure (10.5). Also, the first peak of the zzz component has a very high amplitude compared to the first peak of the xxx component.

10.3 Development of a frequency dependent xc kernel for second-order processes

As shown in the preceding section and throughout the chapter (8), each kernel we have employed so far has its limitations owing to non-locality, frequency dependence, and memory effects.

To account for the electron–hole interaction, one has to solve the Bethe-Salpeter equation with an effective two-particle Hamiltonian. Then, highly satisfactory results are obtained when compared to experimental data for linear response [38].

A generalization of the Bethe-Salpeter equation to second-order processes has been published in [32] but the results obtained for GaAs did not show the same improvement as the one obtained in the case of absorption spectra. Moreover, the complexity and numerical cost of such an approach for second-order processes prevent us for the moment from considering it for a material such as Cr_2O_3.

The "Nanoquanta" kernel has been derived analytically by comparing the Bethe-Salpeter, and the TDDFT equations [77] [34] and can reproduce, within the TDDFT framework, the spectra obtained with BSE with great accuracy. However,

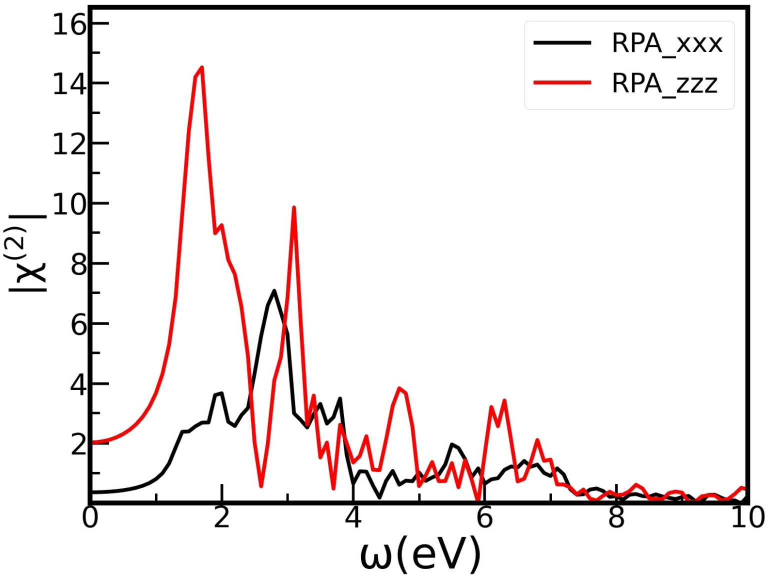

Figure 10.5: Two component (xxx and zzz) of Second-order response function of Cr_2O_3 using RPA

for the same reasons of complexity and computational cost, such a kernel has not been used in this work.

To go beyond the static long-range kernels, we proposed a simple approach based on the fact that i) the first-order and second-order Dyson equations contain the same f_{xc} kernels. ii) The Dyson equation can be split into two equations, one corresponding to the inclusion of v and a second one corresponding to the inclusion of f_{xc}. iii) If f_{xc} is scalar, i.e. only the component corresponding to $\mathbf{G} = \mathbf{G}' = 0$ is nonzero, the second Dyson equation can then be solved analytically. The procedure is detailed below.

The first-order dyson equation, written in condensed notations as,

$$\chi = \chi_0 + \chi_0(v + f_{xc})\chi \tag{10.11}$$

can be split as,

$$\chi^{RPA} = \chi_0 + \chi_0\, v\, \chi^{RPA} \qquad \chi = \chi^{RPA} + \chi^{RPA}\, f_{xc}\, \chi \tag{10.12}$$

For a scalar kernel, we have $\chi_{00} = \chi_{00}^{RPA} + \chi_{00}^{RPA}\, f_{xc}\, \chi_{00}$, which leads to,

$$f_{xc} = \frac{1}{\chi_{00}^{RPA}} - \frac{1}{\chi_{00}} \tag{10.13}$$

where χ_{00} is evaluated in terms of the macroscopic dielectric function $\epsilon_M = 1/\epsilon_{00}^{-1}$

$$\frac{1}{\chi_{00}} = \frac{v\epsilon_M}{1 - \epsilon_M} \tag{10.14}$$

Inserting in equation (10.14) the macroscopic dielectric function obtained from the solution of the Bethe-Salpeter equation $\epsilon_M^{BSE}(\omega)$ and $\epsilon_M^{RPA}(\omega)$, we are able to construct numerically a frequency-dependent long-range kernel.

In a second step, this kernel $f_{xc}(\omega)$ is introduced in the scalar second-order Dyson equation.

10.3.1 Second-order spectra of Cr_2O_3 using frequency dependent kernel

The second-order spectra calculated using this frequency-dependent kernel described above are shown in the figures (10.6) and (10.7). We compared the spectra obtained with this derived kernel to those obtained using RPA and the alpha-kernel method. As this kernel is derived from BSE, it is anisotropic. For this reason, we compared both the xxx and zzz components of the second-order response functions, as shown in the figures (10.6) and (10.7) respectively. As we can see in the figure (10.6), the spectra calculated using this BSE-kernel (represented by fxc_BSE) is very close to the one calculated using the alpha-kernel method. However, we may see a slight red-shift in the spectra predicted using the BSE kernel. This slight difference may be attributed to the frequency dependence of the kernel. Similarly, we also compared the zzz component of the second-order response function. As we can see in the figure (10.7) there is a visible difference in the zzz component of the spectra calculated using the alpha-kernel method and the one calculated using the BSE-kernel. We can notice a small peak at low energy (around 0.7eV) in the spectrum calculated with the BSE-kernel which is absent from the alpha-kernel spectra. This peak is the signature of the bound exciton. Thus, we may conclude that using this frequency-dependent kernel, we can capture a bound excitonic feature absent from the spectra obtained using the alpha-kernel approach. Additionally, we found a difference between the second peak position calculated using this derived kernel and the alpha-kernel approach.

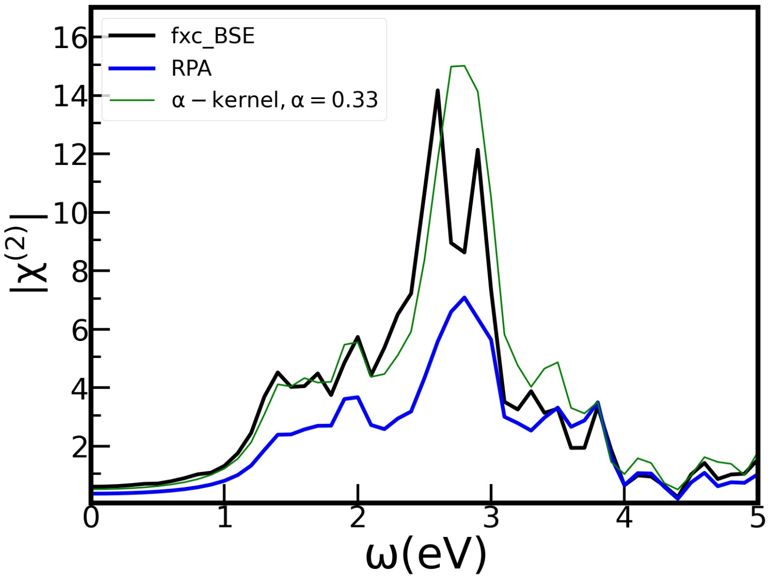

Figure 10.6: Second-order response function (xxx component)using xc kernel derived from BSE

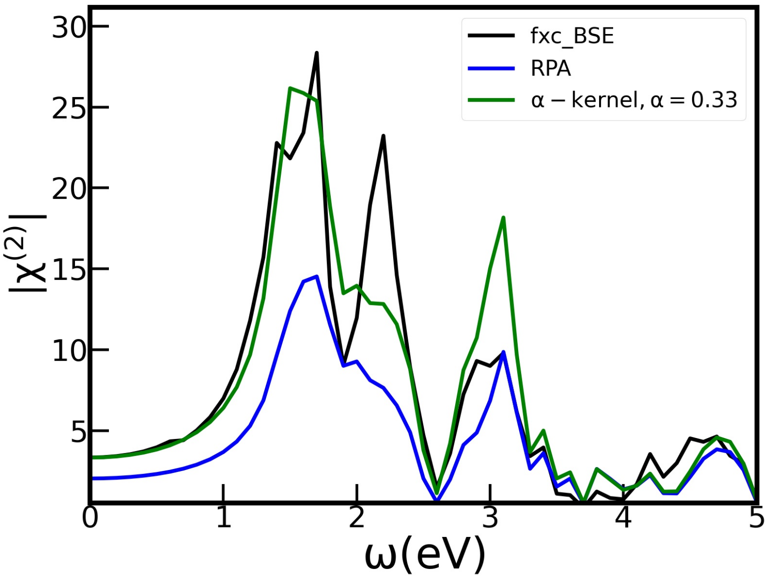

Figure 10.7: Second-order response function (zzz component) using xc kernel derived from BSE

10.4 Effect of the semicore electrons on second-order response of $\mathrm{Cr_2O_3}$ structure in IPA

As previously stated, the semicore electrons effect on the ground state and linear response is significant. As a result, we are interested in seeing what influence the semicore electrons has on the second-order spectra. We have calculated and compared the second-order spectra in the figure (10.8) using the valence electrons pseudopotential and the semicore electrons pseudopotential. In terms of calculation details for the semicore electrons pseudopotential, we changed the scissor value, which is 0.92 eV in this case.

As seen in the figure (10.8), the second-order spectra obtained with the two pseudopotentials are quite different. Two main structures are present in the semicore electrons case at around 1 eV and 2.5 eV, clearly separated but not in the valence electrons pseudopotential case. A remarkable difference is a static value obtained in the two noticeably different calculations. However, at high frequency, the two spectra are quite similar.

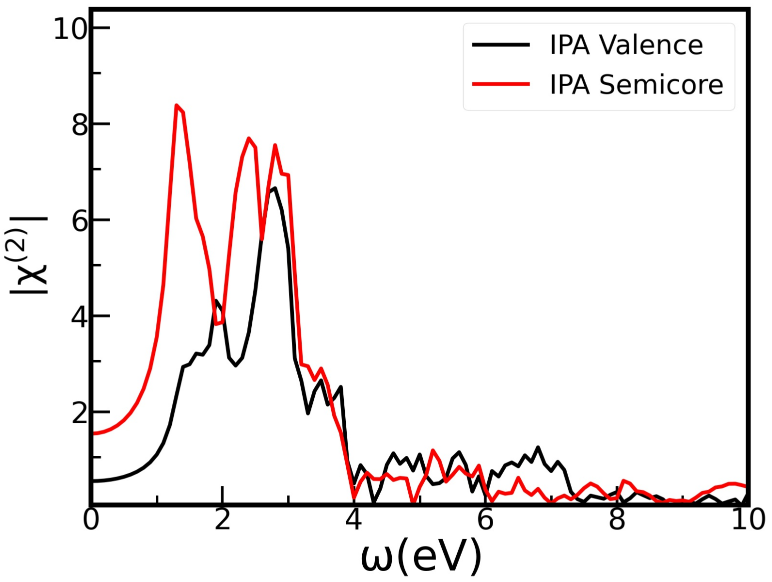

Figure 10.8: Effect of semicore electrons on second-order Response of AF1 structure in IPA

Chapter 11

Study of different AFM structures of Cr_2O_3

There are three distinct AFM structures for Cr_2O_3, which are discussed in the section (7.1), also shown in the figure (11.1)

AF1, the most stable of these three structures, has been studied in the preceding chapters. In this chapter, we will examine and analyze the remaining two structures. Then we will attempt to decipher the differences between the electronic and the optical properties of the three distinct AFM structures.

11.1 Electronic ground state properties of three different AFM Cr_2O_3

As previously stated in the ab-initio framework, the first step is to compute the ground state properties. This section calculates and compares the ground state properties of three AFM structures.

11.1.1 Structure relaxation

We have calculated the relaxed structure geometry using DFT. While performing these calculations, we noticed that changing the spin structure significantly alters the lattice constant and angle, despite the fact that the atomic coordinates remain relatively constant.

Lattice constant

The relaxed lattice constants for the three distinct AFM structures are given in the table (11.1).

Type of structure	Lattice constant(Bohr)
AF1 $(+-+-)$	10.18
AF2 $(++--)$	10.28
AF3 $(+--+)$	10.09

Table 11.1: Lattice constant for three different AFM Cr_2O_3

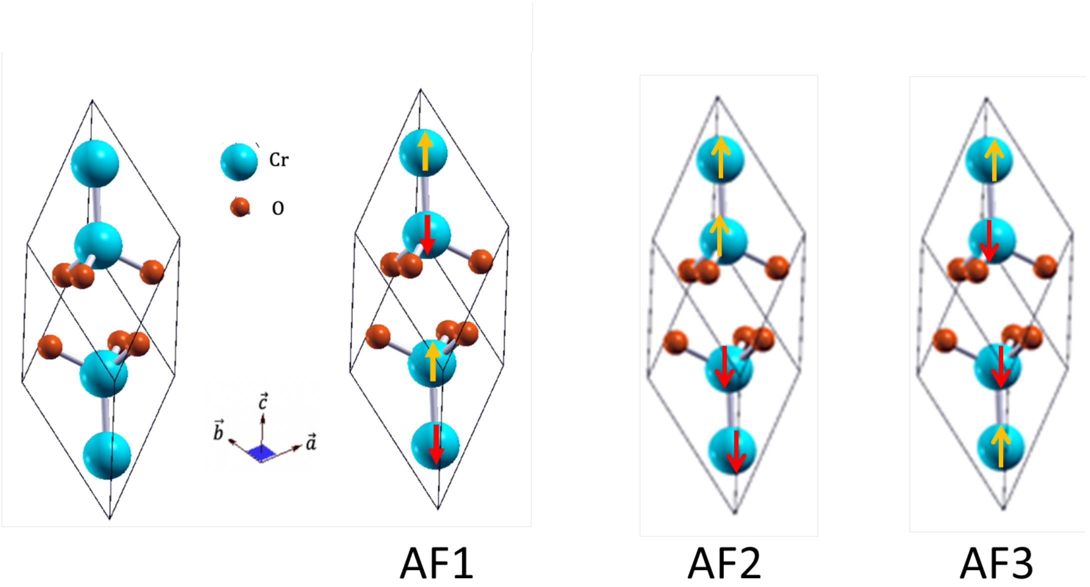

Figure 11.1: Three AFM Cr_2O_3 structures

We see that the lattice constant varies substantially when the spin structure of the AFM Cr_2O_3 is changed.

Angle

We also determined the angle for each of the three distinct AFM structures as shown in table (11.2).

Type of structure	Angle
AF1 $(+-+-)$	55.23°
AF2 $(++--)$	54.19°
AF3 $(+--+)$	56.44°

Table 11.2: Angle for three different AFM Cr_2O_3

Similarly, we found that the angle varies significantly when the spin structure is changed.

11.1.2 Total energy

The total energy of Cr_2O_3 was calculated using DFT calculations for the three AFM structures and compared in the table (11.3). This demonstrates that the AF1 structure has the lowest energy, and hence the AF1 is the most stable structure of Cr_2O_3. The calculations details are identical to those given in the section (7.2.1)

11.1.3 Band gap of three different AFM Cr_2O_3

We have computed the DFT band gap for the three AFM Cr_2O_3. The results are given in table (11.4). As seen in the table (11.4), changing the spin structure

Type of structure	Total Energy(eV)
AF1	-3.670947E+03
AF2	-3.670752E+03
AF3	-3.670445E+03

Table 11.3: Total energy of three different AFM Cr_2O_3

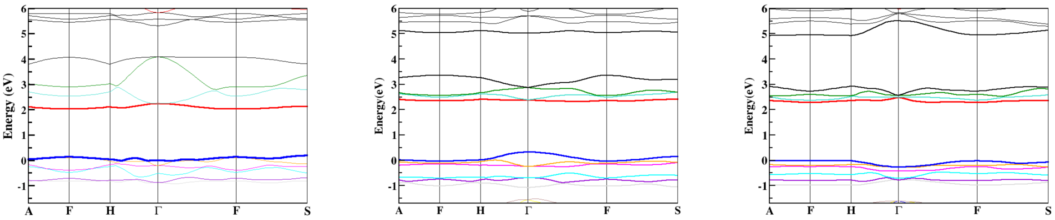

(a) AF1

(b) AF2

(c) AF3

Figure 11.2: Comparison of three AFM Cr_2O_3 bandstructures

substantially alters the gap. AF1 and AF2 are non-centrosymmetric structures, and their band gap is nearly the same as the AF3, a centrosymmetric structure.

Then, we compared the bandstructures of three AFM Cr_2O_3 in figure (11.2). The first significant difference is related to the band gap which is located at the F point for the AF1 and AF3 structures, while it is located at the Γ point for AF2.

The curvature of the bands at AF2 becomes the opposite of the AF1 and AF3 at the high symmetric point, which is the second major difference between these structures.

Type of structure	DFT band gap(eV)	Location
AF1	1.90	F
AF2	2.05	Γ
AF3	2.30	F

Table 11.4: DFT band gap of three AFM structures

11.2 GW band gap of three different structures

Type of structure	GW band gap (eV)
AF1	3.46
AF2	3.35
AF3	3.72

Table 11.5: GW band gap of three AFM structures

11.3 Linear response of three AFM Cr_2O_3 structures

Additionally, we also compared the linear response of three AFM Cr_2O_3. We were interested in determining if changing the spin structures impacted the linear spectra.

We calculated the linear response of the remaining two structures using TDDFT, as we did before. We performed the computations using RPA and the JGM kernel and compared them with the BSE spectra. The results are presented in the following section.

11.3.1 Calculation details

For the TDDFT calculation of the linear spectra, we used the same calculation parameters as we described in the section (8.1.1). However, the scissor value is different for the three structures. The linear calculations are done using the valence electrons pseudopotential. But we calculated the scissor for the three structures using the GW band gap calculated using semicore electrons pseudopotential (as we described in the section (8.1)). The effect of the semicore electrons on the GW bandgap will be discussed in more detail in the next chapter (12). The scissor value which we used here is given in the table (11.6).

Type of structure	Scissor correction(eV)
AF1	0.92
AF2	1.05
AF3	1.10

Table 11.6: Scissor value obtained for three AFM structures

11.3.2 Linea response using RPA approximation

A comparison of Linear Response using RPA for three AFM Cr_2O_3 is shown in the figure (11.3). It shows a substantial difference in the linear spectra for the three structures.

As, we can observe that the AF1 has a first peak of high intensity and the second peak of lower intensity. For AF2 and AF3, on the other hand, the first peak has a modest intensity, while the second peak has a higher intensity. We also found that the intensity of the first peak is lowest in AF3 than in the other two. This difference could be attributed either to the fact that AF3 has a centrosymmetric structure, while AF1 and AF2 are non-centrosymmetric or due to the changes observed in the bandstructures. However, it is not easy to disentangle these two effects. The first peak intensity of AF2 is in the centre of the other two structures. Thereafter we observed that the intensity of the second peak of the AF2 and AF3 structures are the same, while it is significantly different from the AF1 structure. Finally, we see that the AF2 and AF3 peaks moved to lower frequencies.

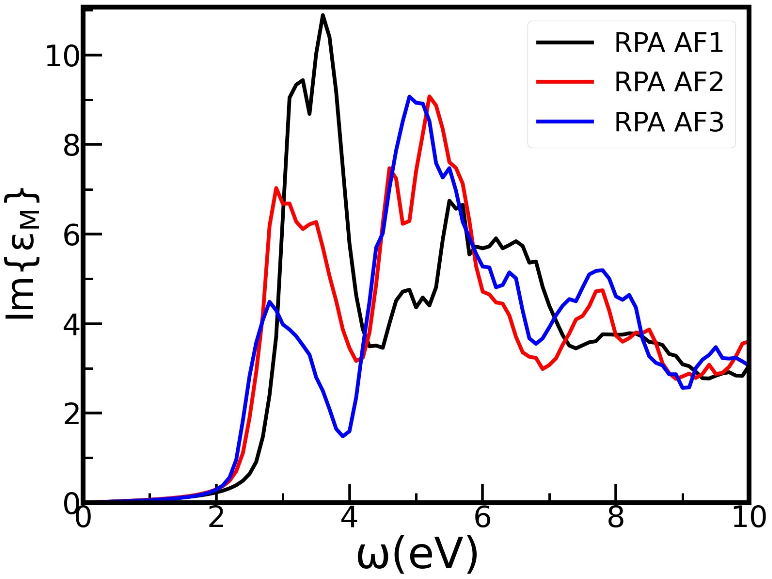

Figure 11.3: Linear response of three magnetic structures of Cr_2O_3 in RPA

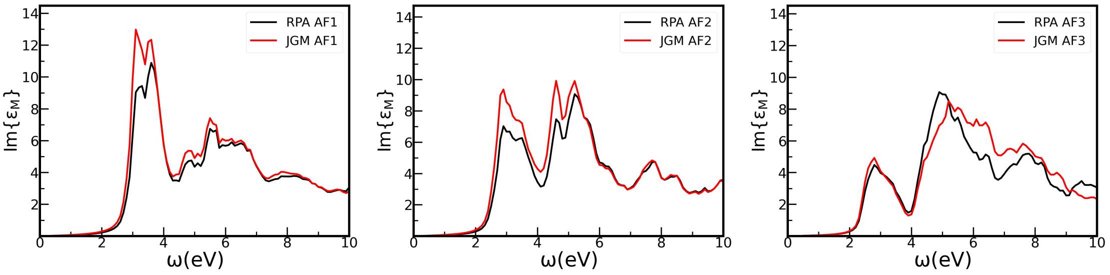

(a) AF1

(b) AF2

(c) AF3

Figure 11.4: Linear response calculated using RPA and JGM kernel for three AFM structures of Cr_2O_3

11.3.3 Linear response using JGM kernel

Furthermore, we have studied the effect of the JGM kernel on the linear spectra of the two structures, AF2 and AF3, as we did on the AF1 structure.

First, we compared the RPA and JGM spectra for all three structures. As shown in graph (11.4), the excitonic effect has a different influence on each Cr_2O_3 structure. For the AF1, adding the excitonic peak through the JGM kernel significantly enhances the strength of the first peak, but a slight increase in the intensity of the second peak is observed as shown in figure (11.4a). However, for AF2, the effect of the JGM kernel strengthens both peaks, as shown in the graph (11.4b). The impact of the JGM kernel on the third case is bit unexpected; it does not enhance the strength of any peak and only changes the shape of the second peak slightly.

Then, we compared the linear spectra computed using the JGM kernel for three different structures types as indicated in the graph (11.5). The differences between the three structures with the JGM kernel follow the same trend observed with RPA for the first peak. However, the second peak of the AF2 and AF3 structures were superimposed in the RPA case, whereas in the case of JGM, they are distinct.

This implies that the excitonic effect has a different impact on Cr_2O_3 depending on how the spins are arranged.

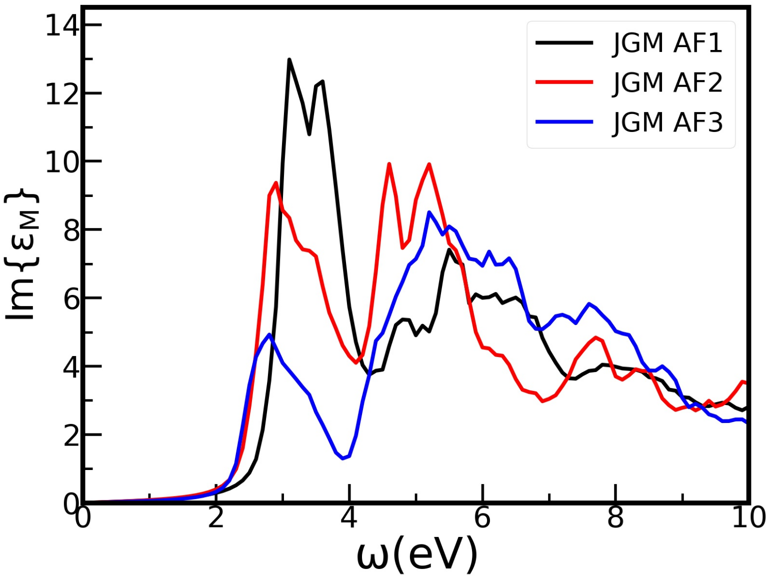

Figure 11.5: Linear response of three different magnetic structures of Cr_2O_3 using the JGM kernel

11.3.4 Linear response using BSE

As shown in the preceding section, the excitonic kernel has a different influence on the various AFM structures. As stated in the section (8.2), the excitonic effect is more appropriately incorporated in the BSE. We conducted BSE calculations on all three structures, using the same parameters described in the previous section (8.2.1).

First of all, we compared the BSE results to those of the RPA and JGM kernels for all three AFM structures in graph (11.6).

By performing BSE calculations on the AF1 structure, the intensity of the first peak is increased while the second peak is redshifted. Additionally, we see an excitonic peak in the gap.

We found a similar trend for the AF2 structure on both peaks. However, we now observe two small peaks in the gap, which can be referred as the bound-excitonic peaks and have very low intensity.

The effect of BSE calculations on the AF3 is different: the excitonic effect through BSE has a negligible influence on the spectra. There is a peak in the gap with an even lower intensity than AF1 and AF2. This is comparable to the effect of the JGM kernel for this structure.

Further, we compared the BSE spectra for three different AFM Cr_2O_3. We can see that they all have different intensities for the first and second peaks and varied positions.

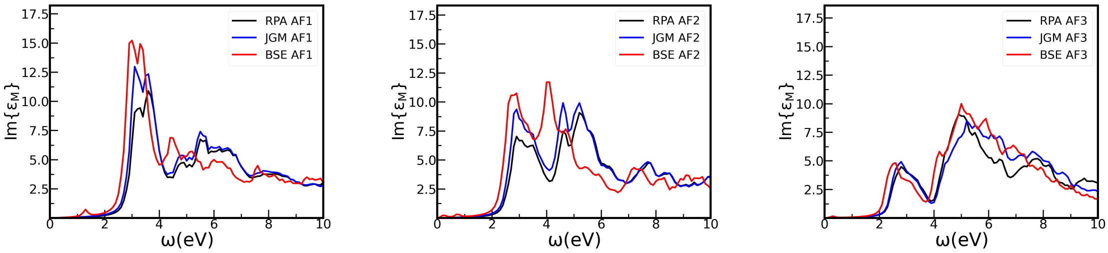

(a) AF1 (b) AF2 (c) AF3

Figure 11.6: Linear response calculated using RPA, JGM kernel and BSE for three different AFM structures of Cr_2O_3

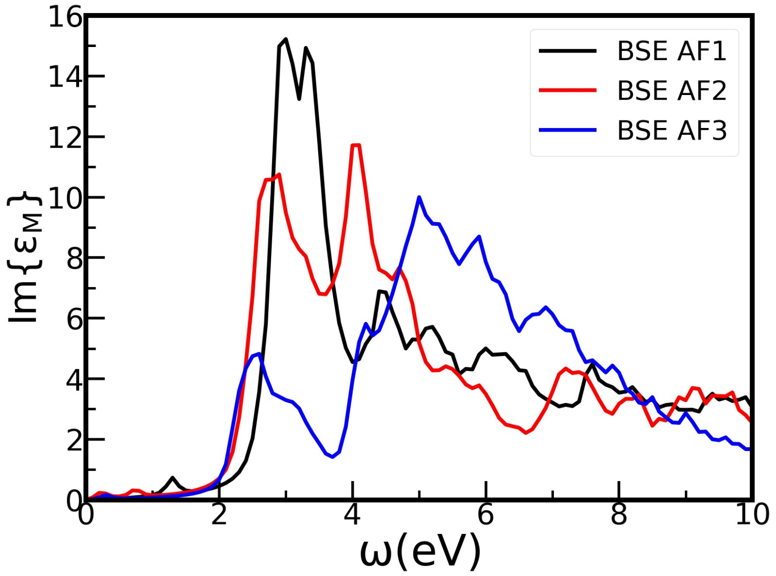

Figure 11.7: Linear response of three different magnetic structures of Cr_2O_3 using BSE

Concerning the peaks observed in the gap, for the AF1 structure, and position and amplitude have been obtained with good accuracy, despite the small amplitude of the peak. The situation is different with AF2 and AF3, the amplitude of the peaks is not enough to provide fully converged results. As a matter of fact, due to memory problems, we could not increase the parameters of the computation to higher values, and we cannot say with certainty that the energy and the amplitude are fully converged.

To summarize, we can say that the altering spin structure has a significant impact on the Cr_2O_3 linear optical properties.

11.4 Second-order response of two different non-centrosymmetric structures of Cr_2O_3

The AF1 and AF2 are non-centrosymmetric structures, whereas the AF3 is centrosymmetric. Hence the second-order response function for AF1 and AF2 is

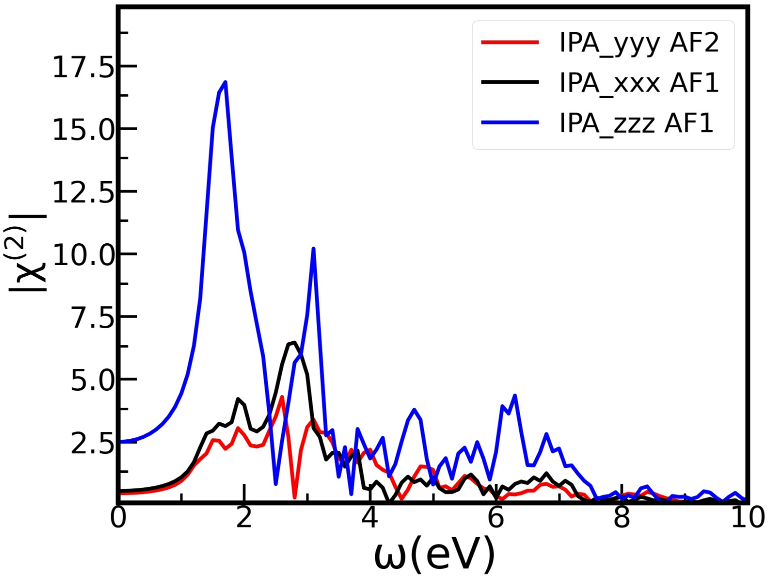

Figure 11.8: Comparison of second-order response function of two different spin non-centrosymmetric structures of Cr_2O_3 using RPA

non-zero, whereas, for AF3, it is zero. The xxx and zzz components for the AF1 structure are non-zero, while it zero for the AF2 structure. On the contrary, the yyy component is not vanishing in AF2 as observed in AF1. These components are plotted in the figure (11.8). As we can see in the figure (11.8), the yyy component of AF2 structure contains the features of both xxx and zzz component of the AF1 structure.

Chapter 12

Effect of semicore electrons on electronic and optical properties of all AFM Cr_2O_3

The impact of adding semicore electrons in the pseudopotential at each level of the theoretical computation for AF1 Cr_2O_3 has previously been addressed in the chapters (7), (8), and (10). Since it has a significant effect on the AF1 structure properties, our goal is to examine the influence of the pseudopotential on the other structures. This study will be done on the GW bandgap and on the absorption spectra.

12.1 Effect of semicore electrons on ground state properties of the three different AFM Cr_2O_3

We used a similar pattern of calculations to those used in the last chapters. We first calculated the ground state of all three configurations with semicore electrons using DFT, and we compared them with the one calculated in the previous chapter i.e. the valence electrons case.

12.1.1 Structure relaxation

In this case, we conducted complete geometry optimizations on the lattice parameters, angle and atomic positions for all structures. All structural optimizations are carried out using Brillouin zone meshes 444.

The relaxed lattice constant and angle are shown below. The atomic position remained relatively constant.

Lattice constant

The values of relaxed lattice constant with and without semicore for each of three structures are listed in table (12.1) given below,

As seen in the table (12.1), the lattice constant changes similarly for the three AFM structures with and without semicore electrons.

Lattice constant(Bohr)	With semicore	Without semicore
AF1	10.22	10.18
AF2	10.32	10.28
AF3.	10.07	10.09

Table 12.1: Effect of semicore electrons Lattice constant for three different AFM Cr_2O_3

Angle

The values of relaxed angles with and without semicore for each of the three structures are listed in the table (12.2) given below,

Structures	With semicore	Without semicore
AF1	54.42°	55.23 °
AF2	53.43°	54.19°
AF3	56.36°	56.44°

Table 12.2: Effect of semicore electrons angle for three different AFM Cr_2O_3

12.1.2 Effect of semicore electrons on DFT band gap of three different AFM Cr_2O_3

We investigated the effect of including a semicore electrons in the DFT band gap for three AFM Cr_2O_3 structures. The results are shown in the table (12.3).

We see that using semicore electrons pseudopotential decreases the DFT band gap for all three structures.

However, the degree of decrease varies according to the structure. The band gap of the AF1 structure, calculated using semicore electrons pseudopotential, decreases by 0.2eV, whereas the band gap of the AF2 structure calculated using semicore electrons pseudopotential decreases by 0.78eV, and the band gap of the AF3 structure calculated using semicore electrons pseudopotential decreases by 0.86eV. It is reasonable to deduce from this pattern of behaviour that the inclusion of semicore states has different effects on different AFM structures.

The AF1 has the largest band gap out of the three structures if the calculations are done with semicore electrons. However, the AF3 structure has the largest gap in the valence electrons case.

DFT band gap(eV)	With semicore	Without semicore	Location
AF1	1.71	1.90	F
AF2	1.27	2.05	Γ
AF3	1.44	2.30	F

Table 12.3: Effect of semicore electrons on DFT band gap of three different AFM structures

Effect of semicore electrons has been studied for many semiconductors for various properties; for example, it has been studied for Si, Ge and GaAs in the

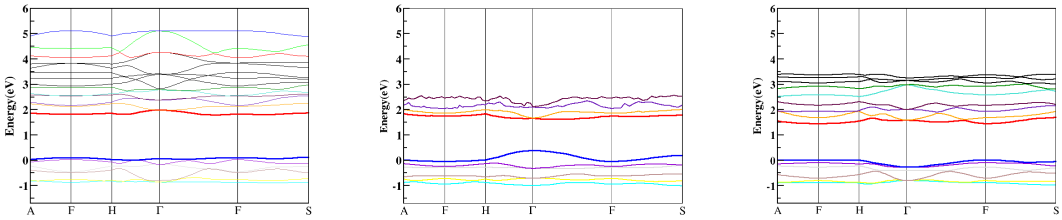

(a) AF1 (b) AF2 (c) AF3

Figure 12.1: Comparison of bandstructure of Cr_2O_3 using semicore electrons pseudopotential for three different AFM structures

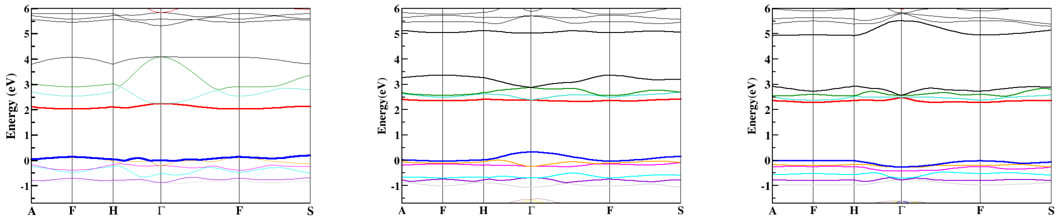

(a) AF1 (b) AF2 (c) AF3

Figure 12.2: Comparison of bandstructure of different AFM structures of Cr_2O_3 using valence electrons pseudopotential

reference [78]. The semicore effects are negligible in Si; they are important if one aims at a good quantitative agreement with experiments in Ge and GaAs. [78]. Similarly, we may deduce from the result shown in the table (12.3) that using semicore electrons in ground state DFT calculations of Cr_2O_3 has a considerable effect on the DFT band gap.

We have also compared the bandstructure calculated using pseudopotential with and without semicore electrons for the three different AFM structures in the figure (12.1).

We again plotted the valence electrons pseudopotential bandstructure in order to compare it to the semicore electrons pseudopotential bandstructure of three distinct AFM structures in graph (12.2).

As seen in the band gap case, the inclusion of semicore electrons has a unique effect on each AFM structure.

The difference in the bandstructure of AF1 structure with and without semicore electrons is plotted in the figures (12.1a) and (12.2a) and has already been discussed in the section (7.2.2).

The two plots (12.1b) and (12.2b) represent the bandstructure of the AF2 structure with and without semicore electrons, respectively. We see the band gap for the AF2 structure is at the Γ point for both with and without semicore calculations. In both cases, the bands in the AF2 bandstructure are nearly identical.

We compare finally the bandstructure of AF3 in the two different situations (12.1c) and (12.2c). We noticed that the highest bands of the VBM are identical in both situations; however, in the first set of conduction bands, the semicore electrons case has a substantially larger number of conduction bands than the valence electrons case.

12.2 Effect of semicore electrons on the GW band gap

We investigate the impact of using semicore electrons pseudopotential in the GW calculations for three different structures in this section, and we provide the values of the GW band gap for the three distinct structures, both with and without semicore electrons in the table (12.4).

As seen in the table (12.4), using semicore electrons pseudopotential decreases the band gap of all three AFM structures when compared to the results obtained using valence electrons. However, this decrease varies according to the kind of structure we used. When the semicore electrons is used on the AF1 structure, the GW band gap is reduced by 0.82eV. It decreases by 1.03eV for AF2 and 1.17eV for AF3. This demonstrates that the semicore electrons used in the GW computations has a varied impact on the AFM structures of Cr_2O_3.

GW band gap(eV)	With semicore	Without semicore
AF1	2.63	3.46
AF2	2.32	3.35
AF3	2.54	3.72

Table 12.4: Effect of semicore electrons on GW band gap of three different AFM structures

The impact of the semicore electrons pseudopotential on the GW band gap Cr_2O_3 is significant. This point has been already discussed in the literature and our present result was expected. For instance, in ref [78], even if the effect of the semicore electrons included in the pseudopotential for Silicon is negligible, the results obtained for Ge and GaAs show that semicore electrons are important for a good quantitative agreement with experiment in Ge and GaAs.

12.3 Effect of semicore electrons on linear response of three different AFM Cr_2O_3

The purpose of this section is to compare the impact of employing a semicore electrons pseudopotential on the linear response spectrum for the three structures of Cr_2O_3. This is done in the Random Phase Approximation. On the other hand, impact of semicore electrons on the GW band gap Cr_2O_3 is very large as we discussed above.

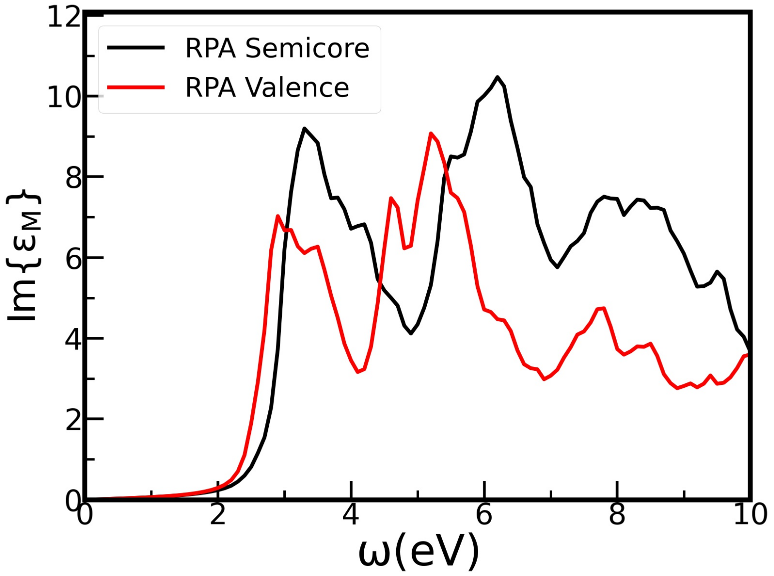

Figure 12.3: Effect of semicore electrons on linear response of AF2 structure in RPA

12.3.1 Effect of semicore electrons on linear response of AF2 and AF3 structures in RPA

The graph (12.3) compares the RPA spectra obtained using the semicore electrons pseudopotential to those obtained using the valence electrons pseudopotential for the AF2 structure.

When semicore electrons are used, the strength of both peaks increases. Additionally, there is an increase in the intensity of the high-frequency region. We may infer from this comparison that adding semicore electrons has a significant effect on the spectra. Furthermore, when we used semicore electrons, the peak width widened, and the peaks became more distinct.

The graph (12.4) compares the RPA spectra for the AF3 structure produced using the semicore electrons pseudopotential and those obtained using the valence electrons pseudopotential.

As can be seen in graph, the use of semicore electrons pseudopotential enhances the intensity of both peaks, and there is also a blue shift of both peaks.

Our main conclusion is that the impact of employing the semicore electrons pseudopotential on the linear spectra of the three structures is the same. It contrasts with the band gap characteristics, where we have shown that the influence of using semicore electrons varies depending on the structure.

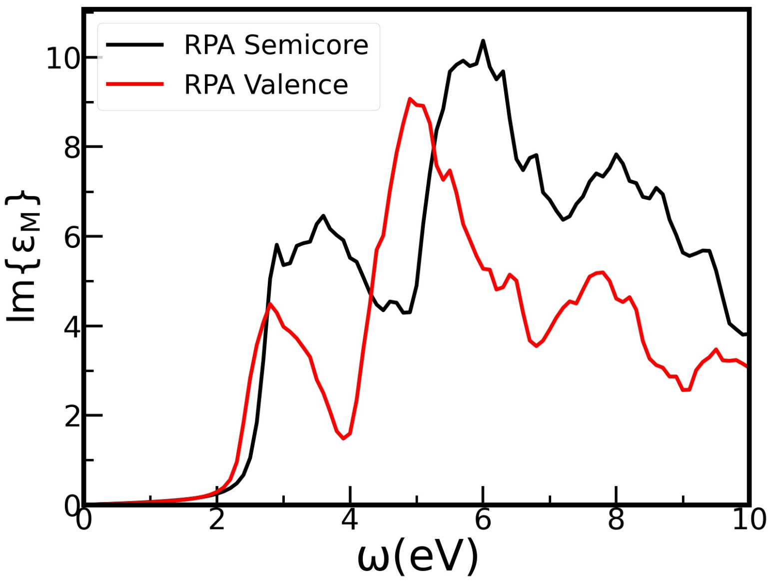

Figure 12.4: Effect of semicore electrons on linear response of AF3 structure in RPA

Chapter 13

Concluding Remarks

Second harmonic generation is widely used to study materials without inversion symmetry as additional information can be obtained compared to traditional linear spectroscopies. It can also be used to probe the spin dynamics in antiferromagnetic materials as SHG reveals the spin arrangement inside the materials. The purpose of this thesis was to describe this second-order process in magnetic material, include the spin-polarization in the time-dependent density functional theory framework, and apply this formalism to chromia (Cr_2O_3), a prototypical antiferromagnetic material.

The ground state properties have been calculated for Cr_2O_3 in the framework of DFT. We have checked that, as already pointed out, it is mandatory to use spin-DFT to get a correct description of the electronic properties: a metallic structure is obtained while a semiconductor material is expected. We have studied the bandstructure of the material and evaluated the quasiparticle corrections in the GW approximation.

The influence of the pseudopotential has also been analyzed in the bandgap calculation. We have shown that incorporating the Cr semicore electrons (as a valence) has a considerable impact on the quasiparticle energies of Cr_2O_3 and lead to a value in good agreement with the experimental band gap.

In a second step, we have calculated the linear response of the Cr_2O_3, and we have studied in detail the optical absorption spectra. We have shown that incorporating the spin-polarization and the local field effects has a negligible contribution to the linear response of the material. However, accounting for the excitonic effects is particularly important. Long-range kernels, such as the α-kernel, the bootstrap, or the JGM kernel, lead to a systematic increase of the absorption and to a redshift of the absorption edge. For comparison, we have solved the Bethe-Salpeter equation and determined the "best" parameter for the α-kernel. Moreover, we have evidenced a strongly bound exciton, which manifests itself by a peak in the gap of the material. To get further insight, we have computed the binding energy of the exciton using the Wannier-Mott model, but the energy obtained within this model is underestimated. Several reasons have been proposed to explain this discrepancy.

While the codes available for calculating the ground state properties and the linear response already accounted for the spin-polarization, we had to derive the second-order Dyson equations for antiferromagnetic materials. These equations have been implemented in the *2light* code [26]. As for the absorption spectra, we have demonstrated the influence of the spin-polarization and of the crystal local-fields on the second-order spectra for Cr_2O_3 is weak. We have used the α kernel for the calculation of the excitonic effects in the second-harmonic spectra of Cr_2O_3, with the α value obtained from the linear response function. Incorporating excitonic effects significantly influences the second-order spectra as the amplitude of the peaks is strongly enhanced.

Solving the Bethe-Salpeter for second-order processes in antiferromagnetic materials cannot be considered at the moment. To go further than the α-kernel, we have derived a frequency-dependent long-range kernel based on the linear spectra obtained with BSE. This simple approximation for Cr_2O_3 shows some deviations from the spectrum obtained with a static kernel, but these results have to be further investigated.

Several structures can be obtained for Cr_2O_3. These structures are identical in terms of crystallographic structure; the only variation is in terms of spin. Two of them, including the one we have studied corresponding to the ground state, are non-centrosymmetric, and one is centrosymmetric. We have found that the three distinct AFM structures exhibit a wide range of different properties. We have found that the band gaps and the bandstructures for the three structures are significantly different. Similarly, the difference between the GW band gaps for the three structures is important. We have computed the linear response and the Second Harmonic Generation and analyzed the differences. We have noticed that the effect of the xc-kernel depends strongly on the structure. Moreover, the amplitude of the excitonic peak is much higher in the ground state structure.

The most striking difference in the Second Harmonic spectra comes from the change of symmetry between the two non-centrosymmetric structures. We demonstrate that the xxx and zzz components of the ground state structure are non-zero, while only the yyy component for the other structure is non-zero. This has significant consequences for future experimental work, as it can help to discriminate easily between several possible structures.

Appendix A

Relation of absorption coefficient and dielectric function

By studying the propagation of plane electromagnetic waves through a medium with a complex refractive index, the connection between absorption coefficient (α) and extinction coefficient (κ) can be deduced. If the wave propagates in the z direction, the electric field's spatial and temporal dependency is given by

$$E(z,t) = E_0 \mathrm{e}^{\mathrm{i}(kz-\omega t)} \tag{A.1}$$

where k is the wave vector of the light, ω is the angular frequency and E_0 is the amplitude at $z = 0$. In a non-absorbing medium of refractive index n, the wavelength of the light is reduced by a factor n compared to the free-space wavelength λ. Therefore the k and ω are therefore related to each other through

$$k = \frac{2\pi}{(\lambda/n)} = \frac{n\omega}{c} \tag{A.2}$$

This can be generalized to the case of an absorbing medium by allowing the refractive index to be complex

$$k = \tilde{n}\frac{\omega}{c} = (n + \mathrm{i}\kappa)\frac{\omega}{c} \tag{A.3}$$

On substituting eqn (A.3) into eqn (A.1), we obtain

$$\begin{aligned} E(z,t) &= E_0 \mathrm{e}^{\mathrm{i}(\omega \tilde{n} z/c-\omega t)} \\ &= E_0 \mathrm{e}^{-\kappa\omega z/c} \mathrm{e}^{\mathrm{i}(\omega n z/c-\omega t)} \end{aligned} \tag{A.4}$$

This shows that a non-zero extinction coefficient leads to an exponential decay of the wave in the medium. whereas the refractive index n still determines the phase velocity of the wave front.

The optical intensity of a light wave is proportional to the square of the electric field, namely $I \propto EE^*$. We can therefore deduce from eqn (A.4) that the intensity falls off exponentially in the medium with a decay constant equal to $2 \times (\kappa\omega/c)$. On comparing this to Beer's law given in eqn (2.2) we conclude that

$$\alpha = \frac{2\kappa\omega}{c} = \frac{4\pi\kappa}{\lambda} \tag{A.5}$$

where λ is the vacuum wavelength of the light. This shows that κ is directly proportional to the absorption coefficient.

We can relate the refractive index of a medium to its relative dielectric constant ϵ_{r} by using the standard result derived from Maxwell's equations.

In the presence of Matter the Maxwell's equations are written as this

$$\begin{aligned} &\nabla \times \mathbf{H} = \tfrac{1}{c}\tfrac{\partial \mathbf{D}}{\partial t} + \tfrac{4\pi}{c}\mathbf{j}_{ext} \\ &\nabla \times \mathbf{E} = -\tfrac{1}{c}\tfrac{\partial \mathbf{B}}{\partial t} \\ &\nabla \cdot \mathbf{D} = 4\pi n_{ext} \\ &\nabla \cdot \mathbf{B} = 0 \end{aligned} \tag{A.6}$$

where E and H are the electric and magnetic fields, D is the electric displacement, B is the magnetic induction, n_{ext} is the external charge (or free charge) density and j_{ext} the external current density. By combining the first and the third of the Eq. A.6 we have the continuity equation

$$\frac{\partial n_{ext}}{\partial t} + \nabla \cdot \mathbf{j}_{ext} = 0 \tag{A.7}$$

which takes into account the conservation of the charge. The complex dielectric function and complex conductivity are introduced once the constitutive equations

$$\mathbf{D} = \mathbf{D}[\mathbf{E}, \mathbf{H}] \tag{A.8}$$

are specified.

When non-linear effects are neglected we can write linear relations for the constitutive equations. So let's define the complex tensors ϵ through

$$\mathbf{D}(r,t) = \int dr' \int dt' \epsilon(r, r', t-t')\mathbf{E}(r', t') \tag{A.9}$$

This equations define the complex quantities ϵ. The latter are in general tensors, but from now on, this fact will be ignored. In frequency domain the equations read

$$\mathbf{D}(\omega) = \epsilon(\omega)\mathbf{E}(\omega) \tag{A.10}$$

where ϵ is the dielectric tensor. we also have the important relations

$$\epsilon(-\omega) = \epsilon^{*}(\omega) \tag{A.11}$$

We can also relate the electric field E with their derived fields D , by the polarisation P via

$$\mathbf{D} = \mathbf{E} + 4\pi\mathbf{P} \tag{A.12}$$

The quantities P can be (linearly) related to the macroscopic fields via the

$$\mathbf{P} = \chi_e \mathbf{E} \tag{A.13}$$

where χ_e is the electric susceptibility. and Hence,

$$\epsilon = 1 + 4\pi\chi_e \tag{A.14}$$

Without external sources, Maxwell's equations yield

$$\nabla \times \nabla \times \mathbf{E} = -\frac{1}{c}\frac{\partial}{\partial t}(\nabla \times \mathbf{B}) \tag{A.15}$$

$$\nabla(\nabla \cdot \mathbf{E}) - \nabla^2\mathbf{E} = -\frac{1}{c}\frac{\partial}{\partial t}(\frac{\mu}{c}\frac{\partial \mathbf{D}}{\partial t}) \tag{A.16}$$

$$\nabla^2\mathbf{E} = \frac{\mu\epsilon}{c^2}\frac{\partial^2\mathbf{E}}{\partial t^2} \tag{A.17}$$

$$\mathbf{E} = \mathbf{E}_0 \exp^{\iota(k.r-\omega t)} \tag{A.18}$$

with

$$k^2 = \frac{\omega^2}{c^2}\mu\epsilon \tag{A.19}$$

If we suppose that the propagation vector is in x direction,

$$k = \frac{\omega}{c}\sqrt{\mu\epsilon} \tag{A.20}$$

and

$$\mathbf{E}(x,t) = \mathbf{E}_0 e^{\iota\frac{\omega}{c}\sqrt{\mu\epsilon}x} e^{-i\omega t} \tag{A.21}$$

The solution of inside a medium of finite conductivity is the damped wave.

$$\mathbf{E}(x,t) = E_0 e^{\iota\frac{\omega}{c}\tilde{n}x} e^{-i\omega t} \tag{A.22}$$

where the complex refractive index

$$\tilde{n} = \sqrt{\epsilon} = n + \iota k \tag{A.23}$$

The real and the imaginary part of $\tilde{n}$ are the refraction index and the extinction coefficient, respectively, and they are related to the real ϵ_1 and the imaginary part ϵ_2

$$\epsilon_1 = n^2 - \kappa^2 \tag{A.24}$$

$$\epsilon_2 = 2n\kappa \tag{A.25}$$

the absorption coefficient α

$$\alpha = \frac{2\omega\kappa}{c} = \frac{\omega\epsilon_2}{nc} \tag{A.26}$$

the latter giving a linear relation between the absorption coefficient and the imaginary part of the dielectric function.

$$n = \sqrt{\epsilon_{\mathrm{r}}} \tag{A.27}$$

This shows us that if n is complex, then ϵ_r must also be complex. We therefore define the complex relative dielectric constant $\tilde{\epsilon}_\mathrm{r}$ according to

$$\tilde{\epsilon}_\mathrm{r} = \epsilon_1 + \mathrm{i}\epsilon_2 \tag{A.28}$$

By analogy with eqn A.27, we see that $\tilde{n}$ and $\tilde{\epsilon}_\mathrm{r}$ are related to each other through

$$\tilde{n}^2 = \tilde{\epsilon}_\mathrm{r} \tag{A.29}$$

We can now work out explicit relationships between the real and imaginary parts of $\tilde{n}$ and $\tilde{\epsilon}_\mathrm{r}$ by combining eqns A.28 A.29 A.23 . These are

$$\begin{aligned} \epsilon_1 &= n^2 - \kappa^2 \\ \epsilon_2 &= 2n\kappa \end{aligned} \tag{A.30}$$

and

$$n = \frac{1}{\sqrt{2}}\left(\epsilon_1 + \left(\epsilon_1^2 + \epsilon_2^2\right)^{1/2}\right)^{1/2} \tag{A.31}$$

$$\kappa = \frac{1}{\sqrt{2}}\left(-\epsilon_1 + \left(\epsilon_1^2 + \epsilon_2^2\right)^{1/2}\right)^{1/2} \tag{A.32}$$

This analysis shows us that $\tilde{n}$ and $\tilde{\epsilon}_\mathrm{r}$ are not independent variables: if we know ϵ_1 and ϵ_2 we can calculate n and κ, and vice versa. Note that if the medium is only weakly absorbing, then we can assume that κ is very small, so that eqns A.31 and A.32 simplify to

$$\begin{aligned} n &= \sqrt{\epsilon_1} \\ \kappa &= \tfrac{\epsilon_2}{2n}. \end{aligned} \tag{A.33}$$

These equations show us that the refractive index is basically determined by the real part of the dielectric constant, while the absorption is mainly determined by the imaginary part. This generalization is obviously not valid if the medium has a very large absorption coefficient.

Appendix B

Convergence study in linear response calculations

Several convergence tests have been performed in the Linear response calculation of Cr_2O_3, and some of them are detailed below.

B.1 Convergence in terms of number of bands in IPA

This section discusses convergence in terms of number of bands(nbands) for the linear response of Cr_2O_3 in the IPA approximation.

The figure (B.2 and (B.1) describes the convergence in terms of number of band for the real and imaginary part of dielectric function respectively.

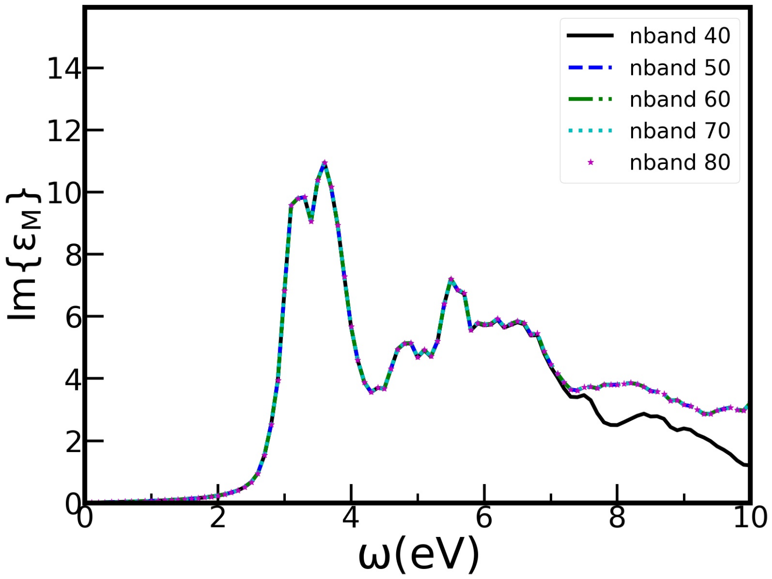

Figure B.1: Convergence in terms of number of bands for linear response of Cr_2O_3 using IPA

The imaginary part of the dielectric function is converged at nband=40, whereas the real component is converged at nband=70. As a result, we chose nband=70 as

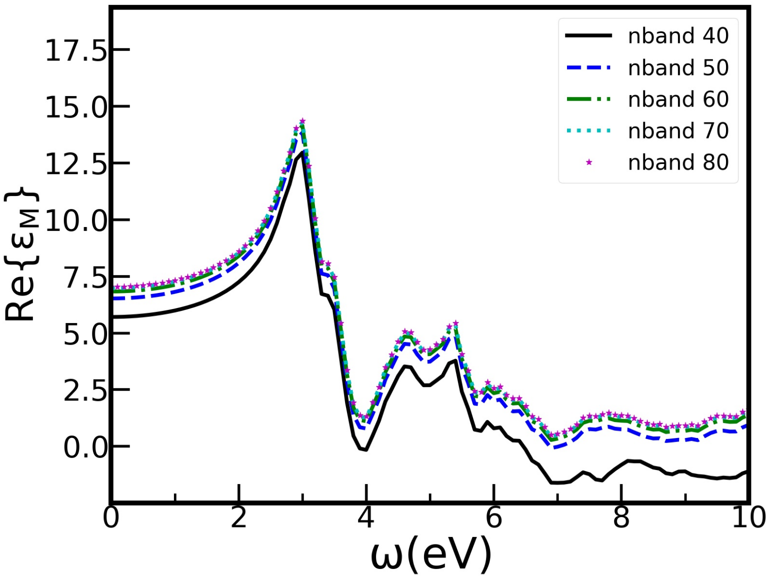

Figure B.2: Convergence in terms of number of bands for linear response of Cr_2O_3 using IPA

the converged value for the rest of the calculations with the valence electrons pseudopotential. In the case of semicore electrons pseudopotential, we have checked that 70 bands was also enough for the imaginary part of the dielectric function.

We have tested the convergence for the RPA calculations and we have seen that 70 bands was enough in both cases. This was expected because the local field effects are very weak for Cr_2O_3.

B.1.1 Other convergence parameters value

The other convergence parameters value used in these tests is shown below.

1. npwwfn 3000
2. kpoint grid 666

B.2 Convergence in terms of number of planewaves (npwwfn) in IPA

B.2.1 Convergence in terms of number of planewaves (npwwfn) in IPA for valence electrons pseudopotential

This section discuss the convergence in terms of number of planewaves (npwwfn) to describes the wave function for the linear response of Cr_2O_3 in the IPA approximation for the valence electrons pseudopotential.

The figure (B.3 and (B.4) describes the convergence in terms of npwwfn .

The imaginary part of the dielectric function is converged at npwwfn 3000 completely. As a result, we chose npwwfn 3000 as the converged value for the rest of the calculations.

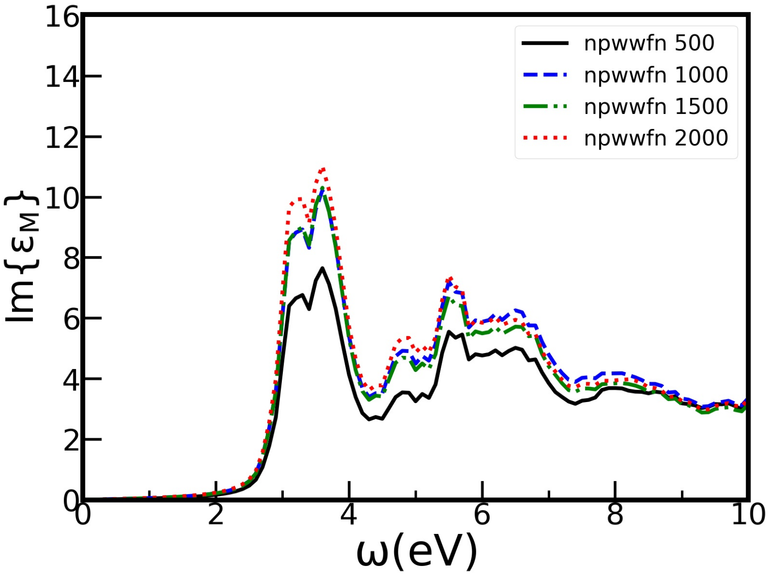

Figure B.3: Convergence in terms of npwwfn for linear response of Cr_2O_3 using IPA

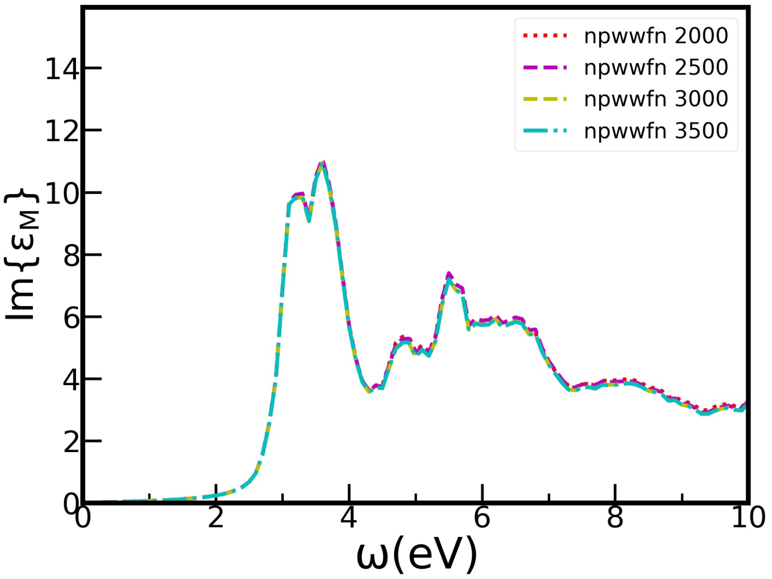

Figure B.4: Convergence in terms of npwwfn for linear response of Cr_2O_3 using IPA

Other convergence parameters value

The other convergence parameters value used in these tests is shown below.

1. nband 70

2. kpoint grid 666

B.2.2 Convergence in terms of number of planewaves (npwwfn) in IPA for semicore electrons pseudopotential

This section discuss the convergence in terms of number of planewaves (npwwfn) to describes the wave function for the linear response of Cr_2O_3 in the IPA approximation for the semicore electrons pseudopotential.

The figure (B.5 and (B.6) describes the convergence in terms of npwwfn .

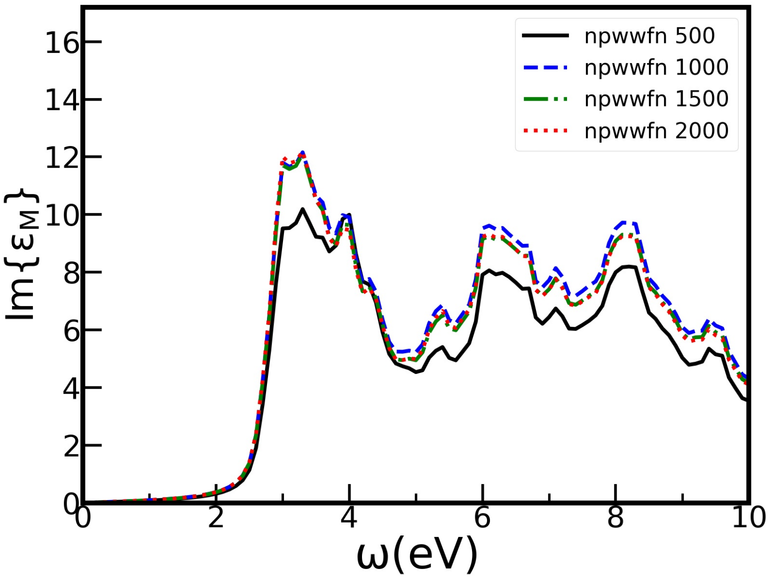

Figure B.5: Convergence in terms of npwwfn for linear response of Cr_2O_3 using IPA

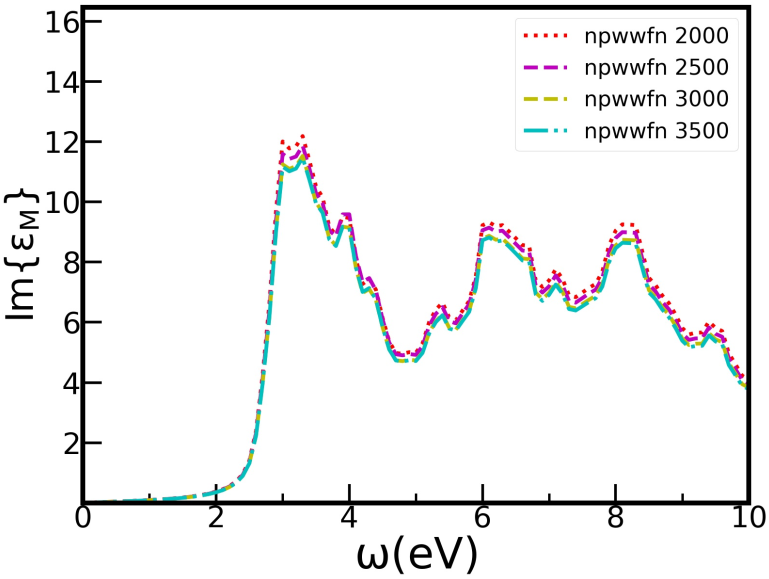

Figure B.6: Convergence in terms of npwwfn for linear response of Cr_2O_3 using IPA

The imaginary part of the dielectric function is converged at npwwfn 3000 completely. As a result, we chose npwwfn 3000 as the converged value for the rest of the calculations.

Other convergence parameters value

The other convergence parameters value used in these tests is shown below.

1. nband 70
2. kpoint grid 666

B.3 Convergence in terms of kpoints in IPA

This section discusses convergence in terms of number of kpoints used for the linear response of Cr_2O_3 in the IPA approximation.

The figure (B.7 describes the convergence in terms of kpoint grid for imaginary part of dielectric function.

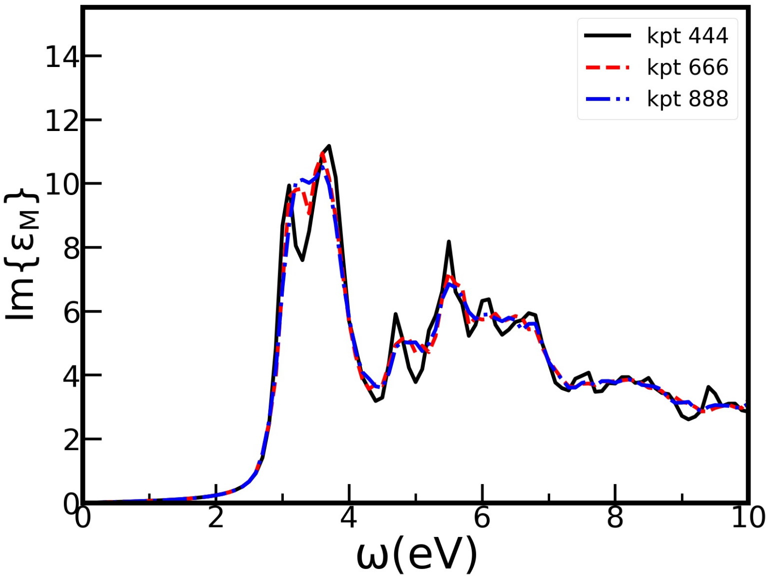

Figure B.7: Convergence in terms of kpoints for linear response of Cr_2O_3 using IPA

As we can see in the figure that the imaginary part of the dielectric function is converged for the kpoint grid 666.

B.3.1 Other convergence parameters value

The other convergence parameters value used in these tests is shown below.

1. npwmat 1
2. npwwfn 3000
3. nband 70

B.4 Convergence in BSE calculations

Their are various input parameters that has to be converged in the BSE calculations. To compute BSE, one must first perform convergence on the screening parameters and then on the BSE parameters.

In both screening and BSE computations, there are various parameters that must be converged. Convergence in terms of a few parameters in both screening and BSE calculations is discussed below.

B.4.1 Convergence in terms of number of band in screening

The convergence in terms of number of bands in the screening is shown in the figure (B.8. As we can see in the figure that the value of nband 200 is the converged value for screening.

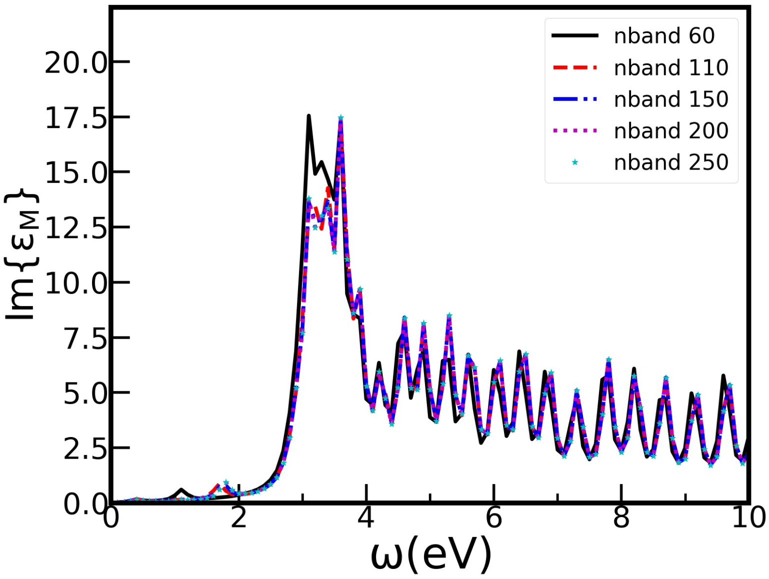

Figure B.8: Convergence in terms of number of bands in screening for linear response of Cr_2O_3 in BSE

Other convergence parameters value

Other parameters value used in this convergence test is given below.

Screening parameters

1. npwmat 113
2. npwwfn 1600
3. lomo 1

BSE parameters

1. npwmat 113

2. npwwfn 3000
3. nbands 60
4. lomo 1

B.4.2 Convergence in terms of number of band in BSE

The convergence in the BSE calculations are given in the figure (B.9) and (B.10). Because the BSE calculations are computationally intensive, we were only able to go up to nband 60 for Cr_2O_3.

To ensure that the calculations were converged, we suppressed some bands in the valence bands using the parameter lomo. lomo describes the lowest occupied band.

In the figure (B.9) and (B.10) we used two different value of lomo to check the convergence for higher bands. As we can see in both the figure that the effect of higher bands in less on the spectra which say that number of bands 60 are converged value.

Hence in our calculations we considered number of bands 60 with lomo 1.

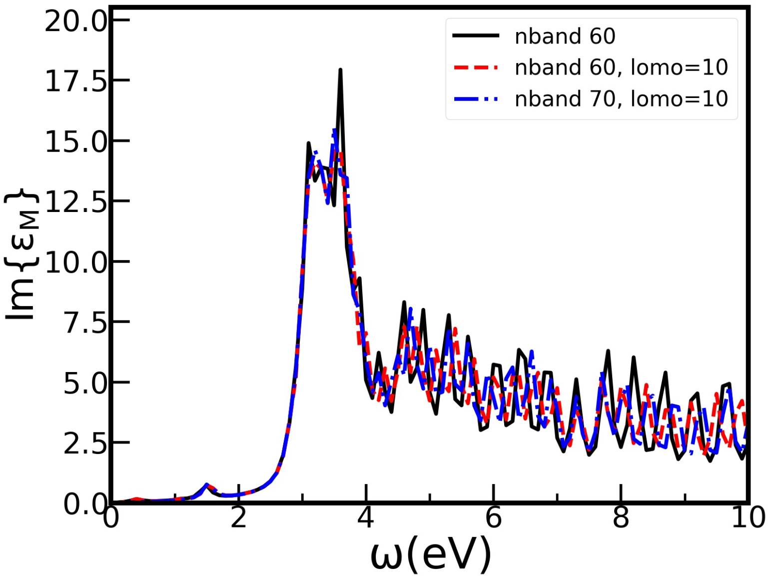

Figure B.9: Convergence in terms of number of bands in BSE for linear response of Cr_2O_3 in BSE

Other convergence parameters value

The other parameters value used in this convergence test is given below.

Screening parameters

1. npwmat 113

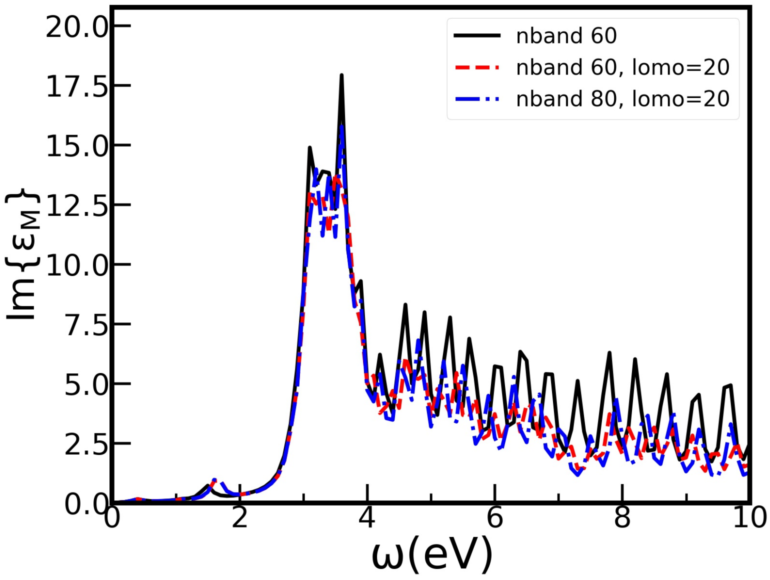

Figure B.10: Convergence in terms of number of bands in BSE parameters for linear response of Cr_2O_3 in BSE

2. npwwfn 1600
3. nbands 200
4. lomo 1

BSE parameters

1. npwmat 113
2. npwwfn 3000
3. lomo 1

Appendix C

Convergence study in case of Second-order response function

Several convergence tests have been performed in the Second-order response calculation of Cr_2O_3, and one of them are detailed below.

C.1 Convergence in terms of number of bands

The figure (C.1) and (C.2) shows that the convergence in terms of number of band in the second-order response. The nband converged value is 200 for the second-order response of Cr_2O_3.

Other convergence parameters value

The other parameters value used in the convergence study is given below,

1. npwwfn 3000
2. lomo 1

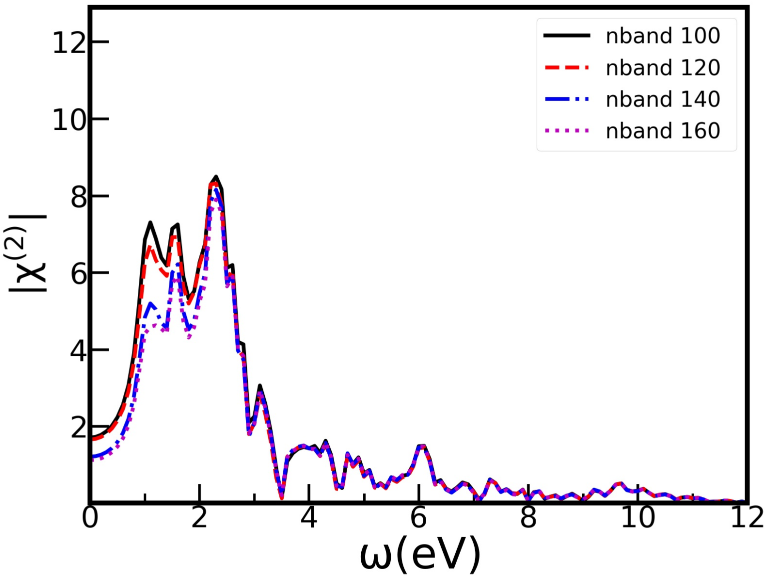

Figure C.1: Convergence in terms of number of band for second-order response of Cr_2O_3 in IPA

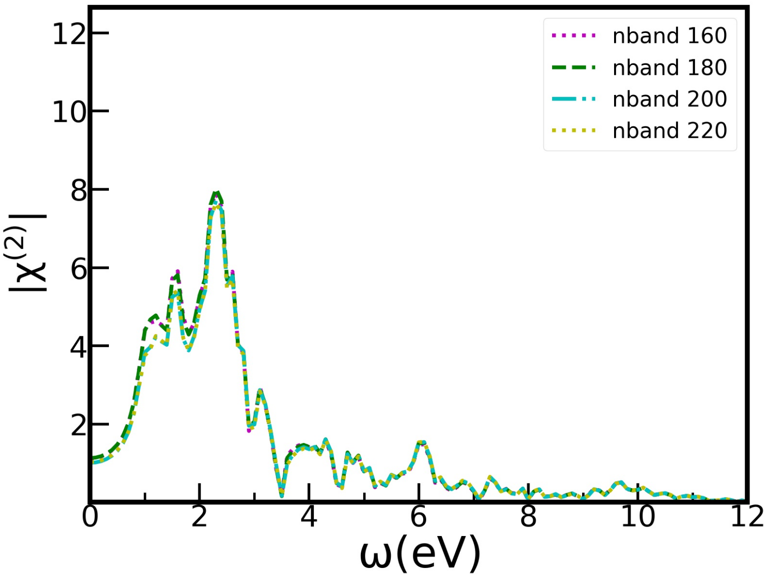

Figure C.2: Convergence in terms of number of band for second-order response of Cr_2O_3 in IPA

Appendix D

Convergence study in the GW band gap calculations

To get the accurate GW band gap various parameters in the screening, and also in the self energy, has to be converged. The convergence test is done at the Γ points. We did the convergence study in GW calculations using both pseudopotentials (valence and semicore electrons pseudopotentials). Many convergence test has been performed while doing the calculations. A few of the many tests for convergence are shown in this appendix.

D.1 Convergence study of GW calculations using valence electrons pseudopotential

We started our calculations with the valence electrons pseudopotential. In this section, the convergence test using valence electrons pseudopotential has been shown.

D.1.1 Convergence in terms of number of bands in the self energy calculations

The convergence test in terms of number of bands for the self energy calculations is given in the table (D.1). The nband value 800 is the converged value within 0.01eV as shown in the table (D.1).

Other convergence parameters value

Parameters in screening calculations
ecuteps 17
ecutwfn 8
nband 240

Parameters in self-energy calculations
ecutsigx 30.0

ecutwfn 16

Number of band	E^0(eV)	E^{GW} (eV)	ΔE^{GW} (eV)
600	2.254	3.754	1.5
650	2.254	3.744	1.49
700	2.254	3.739	1.485
750	2.254	3.739	1.48
800	2.254	3.729	1.475
850	2.254	3.729	1.475

Table D.1: Convergence in terms of number of band in self energy

In the table (D.1), E^0 is the KS band gap, E^{GW} is the GW band gap and ΔE^{GW} is the difference between the GW band gap and KS band gap.

D.1.2 Convergence in terms of number of planewave for wavefunction (ecutwfn) in the self-energy calculations

The convergence in terms of number of planewave for wavefunction (ecutwfn) is shown in the table (D.2). As we can see in the table (D.2) that ecutwfn 20 is converged within 0.01eV.

Other convergence parameters value

Parameters in screening calculations
ecuteps 17
ecutwfn 8
nband3 240

Parameters in self energy calculation
ecutsigx 30.0
nband 800

ecutwfn	E^0(eV)	E^{GW} (eV)	ΔE^{GW}(eV)
16	2.254	3.729	1.475
20	2.254	3.750	1.496
24	2.254	3.752	1.499
28	2.254	3.752	1.499

Table D.2: Convergence in terms of ecutwfn in self-energy

D.1.3 Convergence in terms of number of planewave for exchange part (ecutsigx) in the self-energy calculations

The convergence in terms of number of planewave for exchange part (ecutsigx) is shown in the table (D.3). As we can see in the table (D.3), that ecutsigx 28 is consider as converged within 0.01eV.

Other convergence parameters value

Parameter in screening calculations
ecuteps 17
ecutwfn 8
nband 240

Parameter in self energy calculations
ecutwfn 16
nband 800

ecutsigx	E^0 (eV)	E^{GW}(eV)	ΔE^{GW}(eV)
20	2.254	3.814	1.56
24	2.254	3.744	1.49
28	2.254	3.728	1.475
32	2.254	3.728	1.475

Table D.3: Convergence in terms of number of planewave for exchange part (ecutsigx) in self-energy

D.1.4 Convergence in terms of number of bands in screening parameters

The convergence in terms of number of band in screening is shown in the table (D.4). The nband value 390 is converged within 0.01eV.

Other convergence parameters value

Parameters in screening calculations
ecuteps 17
ecutwfn 8

Parameters in self energy calculations
ecutsigx 28
ecutwfn 20
nband 800

D.1.5 Convergence in terms of ecuteps in screening parameters

ecuteps determines the cut-off energy of the planewave set used to represent the independent-particle susceptibility $\chi^{(0)}$, the dielectric matrix , and its inverse.

Number of bands	E^0 (eV)	E^{GW}(eV)	ΔE^{GW}(eV)
240	2.254	3.804	1.55
290	2.254	3.714	1.53
340	2.254	3.754	1.5
390	2.254	3.749	1.496
440	2.254	3.749	1.496

Table D.4: Convergence in terms of number of bands in screening

The Convergence in terms of ecuteps is shown in table (D.5). As can be seen in the table that ecuteps 17 is converged within 0.01eV.

Other convergence parameters value

Parameters in screening calculations
ecutwfn 8
nband 390

Parameters in self energy calculations
ecutsigx 28
ecutwfn 20
nband 800

ecuteps	E^0(eV)	E^{GW}(eV)	$\Delta E^{GW}(eV)$
17	2.254	3.749	1.496
21	2.254	3.751	1.497
25	2.254	3.752	1.498
29	2.254	3.752	1.498

Table D.5: Convergence in terms of ecuteps in screening

D.1.6 Convergence in terms of number of planewave for wave-function (ecutwfn) in screening parameters

The Convergence in terms of number of planewave for wave-function (ecutwfn) is shown in the table (D.6). The ecutwfn value 20 is converged within 0.01eV.

Other convergence parameters value

Parameters in screening calculations
ecuteps 17
nband 390

Parameters in self energy calculations
ecutsigx 28
ecutwfn 20

nband 800

ecutwfn	E^0(eV)	E^{GW} (eV)	ΔE^{GW}(eV)
8	2.254	3.749	1.496
10	2.254	3.536	1.283
12	2.254	3.440	1.187
14	2.254	3.384	1.130
16	2.254	3.429	1.176
20	2.254	3.440	1.187
24	2.254	3.441	1.188

Table D.6: Convergence in terms of number of planewave for wave-function (ecutwfn) in screening

D.2 Convergence study of GW calculations using semicore electrons pseudopotential

The convergence study using semicore electron pseudopotential is started with the converged value calculated using valence electrons pseudopotential.

D.2.1 Convergence in terms of number of bands in the self energy calculations

The convergence test in terms of number of bands for the self energy calculations is given in the table (D.7). The nband value 1000 is the converged value within 0.01eV as shown in the table (D.7).

Other convergence parameters value

Parameters in screening calculations
ecuteps 23
ecutwfn 20
nband 450

Parameters in self energy calculations
ecutsigx 30
ecutwfn 25

In the table (D.7), E^0 is the KS band gap, E^{GW} is the GW band gap and ΔE^{GW} is the difference between the GW band gap and KS band gap.

Number of bands	E^0(eV)	E^{GW} (eV)	ΔE^{GW} (eV)
800	1.975	3.025	1.05
850	1.975	3.025	1.05
900	1.975	2.975	1.0
1000	1.975	2.968	0.993
1050	1.975	2.968	0.993

Table D.7: Convergence in terms of number of bands in self-energy calculations

D.2.2 Convergence in terms of number of planewave for wavefunction (ecutwfn)

The Convergence in terms of number of planewave for wavefunction (ecutwfn) is shown in the table (D.8). As we can see in the table (D.8) that ecutwfn 24 is converged within 0.01eV.

Other convergence parameters value

Parameters in screening calculations
ecuteps 23
ecutwfn 20
nband 450

Parameters in self energy calculations
ecutsigx 30
nband 800

ecutwfn	E^0(eV)	E^{GW} (eV)	ΔE^{GW}(eV)
20	1.975	3.045	1.07
24	1.975	2.965	0.99
28	1.975	2.965	0.99

Table D.8: Convergence in terms of ecutwfn in self-energy

D.2.3 Convergence in terms of number of planewave for exchange part (ecutsigx) in the self-energy calculations

The convergence n terms of number of planewave for exchange part (ecutsigx) is shown in the table (D.9). As we can see in the table (D.9), that ecutsigx 30 is consider as converged within 0.01eV.

Other convergence parameters value

Parameter in screening calculations
ecuteps 23
ecutwfn 20

nband 450

Parameter in self-energy calculations
ecutwfn 25
nband 800

ecutsigx	E^0 (eV)	E^{GW}(eV)	ΔE^{GW}(eV)
28	1.975	2.985	1.01
30	1.975	2.965	0.99
34	1.975	2.965	0.99

Table D.9: Convergence in terms of number of planewave for exchange part (ecutsigx) in self-energy

D.2.4 Convergence in terms of number of planewave for wave-function (ecutwfn) in screening parameters

The Convergence in terms of number of planewave for wave-function (ecutwfn) in the screening calculations is shown in the table (D.10). The ecutwfn value 26 is converged within 0.01eV.

Other convergence parameters value

Parameters in screening calculations
ecuteps 23
nband 390

Parameters in self-energy calculations
ecutsigx 30
ecutwfn 24
nband 1000

ecutwfn	E^0(eV)	E^{GW} (eV)	ΔE^{GW}(eV)
20	1.975	2.966	0.991
23	1.975	2.955	0.98
26	1.975	2.941	0.966
30	1.975	2.941	0.966

Table D.10: Convergence in terms of number of planewaves for wave-function (ecutwfn) in screening

Bibliography

[1] V. G. Sala, S. Dal Conte, T. A. Miller, D. Viola, E. Luppi, V. Véniard, G. Cerullo, and S. Wall, "Resonant optical control of the structural distortions that drive ultrafast demagnetization in Cr_2O_3," Phys. Rev. B, vol. 94, p. 014430, Jul 2016.

[2] Y. R. Shen, The principles of nonlinear optics, ser. Wiley classics library. Hoboken, N.J: Wiley-Interscience, 2003.

[3] P. A. Franken, A. E. Hill, C. W. Peters, and G. Weinreich, "Generation of optical harmonics," Phys. Rev. Lett., vol. 7, pp. 118–119, Aug 1961.

[4] F. X. Wang, F. J. Rodríguez, W. M. Albers, R. Ahorinta, J. E. Sipe, and M. Kauranen, "Surface and bulk contributions to the second-order nonlinear optical response of a gold film," Phys. Rev. B, vol. 80, p. 233402, Dec 2009.

[5] S. A. Yang, X. Li, A. D. Bristow, and J. E. Sipe, "Second harmonic generation from tetragonal centrosymmetric crystals," Phys. Rev. B, vol. 80, p. 165306, Oct 2009.

[6] B. Fluegel, A. Mascarenhas, J. F. Geisz, and J. M. Olson, "Second harmonic generation in ordered $Ga_{1-x}In_xP$," Phys. Rev. B, vol. 57, pp. R6787–R6790, Mar 1998.

[7] S. Sharma, J. K. Dewhurst, and C. Ambrosch-Draxl, "Linear and second-order optical response of III-V monolayer superlattices," Phys. Rev. B, vol. 67, p. 165332, Apr 2003.

[8] M. Kauranen, T. Verbiest, J. J. Maki, and A. Persoons, "Second-harmonic generation from chiral surfaces," The Journal of Chemical Physics, vol. 101, no. 9, pp. 8193–8199, 1994.

[9] Y. R. Shen, "Optical second harmonic generation at interfaces," Annual Review of Physical Chemistry, vol. 40, no. 1, pp. 327–350, 1989.

[10] P. Figliozzi, L. Sun, Y. Jiang, N. Matlis, B. Mattern, M. C. Downer, S. P. Withrow, C. W. White, W. L. Mochán, and B. S. Mendoza, "Single-beam and enhanced two-beam second-harmonic generation from silicon nanocrystals by use of spatially inhomogeneous femtosecond pulses," Phys. Rev. Lett., vol. 94, p. 047401, Jan 2005.

[11] M. Oh e, H. Yokoyama, S. Yorozuya, K. Akagi, M. A. Belkin, and Y. R. Shen, “Sum-frequency vibrational spectroscopy of a helically structured conjugated polymer,” Phys. Rev. Lett., vol. 93, p. 267402, Dec 2004.

[12] S. A. Mitchell, R. A. McAloney, D. Moffatt, N. Mora-Diez, and M. Z. Zgierski, “Second-harmonic generation optical activity of a polypeptide -helix at the airwater interface,” The Journal of Chemical Physics, vol. 122, no. 11, p. 114707, 2005.

[13] H. M. Su, J. T. Ye, Z. K. Tang, and K. S. Wong, “Resonant second-harmonic generation in monosized and aligned single-walled carbon nanotubes,” Phys. Rev. B, vol. 77, p. 125428, Mar 2008.

[14] A. Lupei, E. Antic-Fidancev, G. Aka, D. Vivien, P. Aschehoug, P. Goldner, F. Pellé, and L. Gheorghe, “Spectroscopic and crystal field studies of Nd^{3+} in $GdCa_4O(BO_3)_3$ and $YCa_4O(BO_3)_3$,” Phys. Rev. B, vol. 65, p. 224518, Jun 2002.

[15] V. Fock, “Näherungsmethode zur lösung des quantenmechanischen mehrkörperproblems,” Zeitschrift für Physik, vol. 61, no. 1, pp. 126–148, 1930.

[16] P. Hohenberg and W. Kohn, “Inhomogeneous electron gas,” Phys. Rev., vol. 136, pp. B864–B871, Nov 1964.

[17] W. Kohn and L. J. Sham, “Self-consistent equations including exchange and correlation effects,” Phys. Rev., vol. 140, pp. A1133–A1138, Nov 1965.

[18] D. M. Ceperley and B. J. Alder, “Ground state of the electron gas by a stochastic method,” Phys. Rev. Lett., vol. 45, pp. 566–569, Aug 1980.

[19] S. Moroni, D. M. Ceperley, and G. Senatore, “Static response and local field factor of the electron gas,” Phys. Rev. Lett., vol. 75, pp. 689–692, Jul 1995.

[20] G. Ortiz, M. Harris, and P. Ballone, “Zero temperature phases of the electron gas,” Phys. Rev. Lett., vol. 82, pp. 5317–5320, Jun 1999.

[21] S. H. Vosko, L. Wilk, and M. Nusair, “Accurate spin-dependent electron liquid correlation energies for local spin density calculations: a critical analysis,” Canadian Journal of Physics, vol. 58, no. 8, pp. 1200–1211, Aug. 1980.

[22] E. Runge and E. K. U. Gross, “Density-functional theory for time-dependent systems,” Phys. Rev. Lett., vol. 52, pp. 997–1000, Mar 1984.

[23] E. K. U. Gross, J. F. Dobson, and M. Petersilka, Density functional theory of time-dependent phenomena. Berlin, Heidelberg: Springer Berlin Heidelberg, 1996, pp. 81–172.

[24] C. Rödl, F. Fuchs, J. Furthmüller, and F. Bechstedt, “Ab initio theory of excitons and optical properties for spin-polarized systems: Application to antiferromagnetic mno,” Phys. Rev. B, vol. 77, p. 184408, May 2008.

[25] E. Luppi, H. Hübener, and V. Véniard, “Ab initio second-order nonlinear optics in solids: Second-harmonic generation spectroscopy from time-dependent density-functional theory,” Phys. Rev. B, vol. 82, p. 235201, Dec 2010.

[26] E. Luppi, N.Tancogne-Dejean, H. Hübener, and V. Véniard, “2light: Ab initio calculations of nonlinear optical properties of materials,” unpublished.

[27] R. M. Martin, L. Reining, and D. M. Ceperley, Interacting Electrons: Theory and Computational Approaches. Cambridge University Press, 2016.

[28] F. J. Dyson, “The radiation theories of tomonaga, schwinger, and feynman,” Phys. Rev., vol. 75, pp. 486–502, Feb 1949.

[29] F. Dyson, “The s matrix in quantum electrodynamics,” Phys. Rev., vol. 75, pp. 1736–1755, Jun 1949.

[30] L. Hedin, “New method for calculating the one-particle green’s function with application to the electron-gas problem,” Phys. Rev., vol. 139, pp. A796–A823, Aug 1965.

[31] L. Hedin and S. Lundqvist, “Effects of electron-electron and electron-phonon interactions on the one-electron states of solids,” ser. Solid State Physics, F. Seitz, D. Turnbull, and H. Ehrenreich, Eds. Academic Press, 1970, vol. 23, pp. 1–181.

[32] F. Bechstedt, Many-Body Approach to Electronic Excitations, ser. Springer Series in Solid-State Sciences. Berlin, Heidelberg: Springer Berlin Heidelberg, 2015, vol. 181.

[33] M. Gatti, “Correlation effects in valence electron spectroscopy of transition metal oxides: many-body perturbation theory and alternative approaches,” Ph.D. dissertation, École POLYTECHNIQUE, Palaiseau, France, December 2007.

[34] F. Sottile, “Response functions of semiconductors and insulators: from the bethe-salpeter equation to time-dependent density functional theory,” Ph.D. dissertation, École POLYTECHNIQUE, Palaiseau, France, September 2003.

[35] W. Hanke and L. J. Sham, “Many-particle effects in the optical excitations of a semiconductor,” Phys. Rev. Lett., vol. 43, pp. 387–390, Jul 1979.

[36] S. Albrecht, L. Reining, R. Del Sole, and G. Onida, “Ab initio calculation of excitonic effects in the optical spectra of semiconductors,” Phys. Rev. Lett., vol. 80, pp. 4510–4513, May 1998.

[37] M. Rohlfing and S. G. Louie, “Electron-hole excitations and optical spectra from first principles,” Phys. Rev. B, vol. 62, pp. 4927–4944, Aug 2000.

[38] G. Onida, L. Reining, and A. Rubio, “Electronic excitations: density-functional versus many-body green’s-function approaches,” Rev. Mod. Phys., vol. 74, pp. 601–659, Jun 2002.

[39] I. Tamm, Relativistic Interaction of Elementary Particles. Berlin, Heidelberg: Springer Berlin Heidelberg, 1991, pp. 157–174.

[40] S. M. Dancoff, "Non-adiabatic meson theory of nuclear forces," Phys. Rev., vol. 78, pp. 382–385, May 1950.

[41] N. Popovici, M. Paramês, R. Da Silva, O. Monnereau, P. Sousa, A. Silvestre, and O. Conde, "KrF pulsed laser deposition of chromium oxide thin films from Cr_8O_{21} targets," Applied Physics A, vol. 79, no. 4-6, pp. 1409–1411, Sep. 2004.

[42] S. Foner, "High-field antiferromagnetic resonance in Cr_2O_3," Phys. Rev., vol. 130, pp. 183–197, Apr 1963.

[43] [Online]. Available: https://www.abinit.org/

[44] J. P. Perdew, R. G. Parr, M. Levy, and J. L. Balduz, "Density-functional theory for fractional particle number: Derivative discontinuities of the energy," Phys. Rev. Lett., vol. 49, pp. 1691–1694, Dec 1982.

[45] L. J. Sham and M. Schlüter, "Density-functional theory of the band gap," Phys. Rev. B, vol. 32, pp. 3883–3889, Sep 1985.

[46] R. W. Godby, M. Schlüter, and L. J. Sham, "Self-energy operators and exchange-correlation potentials in semiconductors," Phys. Rev. B, vol. 37, pp. 10 159–10 175, Jun 1988.

[47] D. Cociorva, W. G. Aulbur, and J. W. Wilkins, "Quasiparticle calculations of band offsets at AlN-GaN interfaces," Solid State Communications, vol. 124, no. 1, pp. 63–66, 2002.

[48] M. S. Hybertsen and S. G. Louie, "Electron correlation in semiconductors and insulators: Band gaps and quasiparticle energies," Phys. Rev. B, vol. 34, pp. 5390–5413, Oct 1986.

[49] S. G. Louie and M. L. Cohen, Conceptual Foundations of Materials: A standard model for ground and excited-state properties. San Diego, CA: Elsevier, 2006.

[50] A. Marini, G. Onida, and R. Del Sole, "Quasiparticle Electronic Structure of Copper in the GW Approximation," Physical Review Letters, vol. 88, no. 1, p. 016403, Dec. 2001.

[51] C.-S. Cheng, H. Gomi, and H. Sakata, "Electrical and optical properties of Cr_2O_3 films prepared by chemical vapour deposition," physica status solidi (a), vol. 155, no. 2, pp. 417–425.

[52] M. M. Abdullah, F. M. Rajab, and S. M. Al-Abbas, "Structural and optical characterization of Cr_2O_3 nanostructures: Evaluation of its dielectric properties," AIP Advances, vol. 4, no. 2, p. 027121, 2014.

[53] J. Sackey, R. Morad, A. Bashir, L.Kotsedi, C.Kaonga, and M. Maaza, "Biosynthesised black α -Cr_2O_3 nanoparticles; experimental analysis and density function theory calculations," Journal of Alloys and Compounds, vol. 850, p. 156671, 2021.

[54] N. J. Mosey, P. Liao, and E. A. Carter, "Rotationally invariant ab initio evaluation of coulomb and exchange parameters for DFT+U calculations," The Journal of Chemical Physics, vol. 129, no. 1, p. 014103, 2008.

[55] Y. Guo, S. J. Clark, and J. Robertson, "Electronic and magnetic properties of Ti_2O_3, Cr_2O_3, and Fe_2O_3 calculated by the screened exchange hybrid density functional," Journal of Physics: Condensed Matter, vol. 24, no. 32, p. 325504, jul 2012.

[56] E. A. Moore, "First-principles study of the mixed oxide $\alpha-$FeCro$_3$," Phys. Rev. B, vol. 76, p. 195107, Nov 2007.

[57] S. Lany, "Band-structure calculations for the $3d$ transition metal oxides in gw," Phys. Rev. B, vol. 87, p. 085112, Feb 2013.

[58] [Online]. Available: http://www.dp-code.org/

[59] I. Vasiliev, S. Öğüt, and J. R. Chelikowsky, "First-principles density-functional calculations for optical spectra of clusters and nanocrystals," Phys. Rev. B, vol. 65, p. 115416, Mar 2002.

[60] S. Botti, F. Sottile, N. Vast, V. Olevano, L. Reining, H. C. Weissker, A. Rubio, G. Onida, R. Del Sole, and R. W. Godby, "Long-range contribution to the exchange-correlation kernel of time-dependent density functional theory," Phys. Rev. B, vol. 69, p. 155112, Apr 2004.

[61] S. Rigamonti, S. Botti, V. Veniard, C. Draxl, L. Reining, and F. Sottile, "Estimating excitonic effects in the absorption spectra of solids: Problems and insight from a guided iteration scheme," Phys. Rev. Lett., vol. 114, p. 146402, Apr 2015.

[62] P. E. Trevisanutto, A. Terentjevs, L. A. Constantin, V. Olevano, and F. D. Sala, "Optical spectra of solids obtained by time-dependent density functional theory with the jellium-with-gap-model exchange-correlation kernel," Phys. Rev. B, vol. 87, p. 205143, May 2013.

[63] A. Zangwill and P. Soven, "Density-functional approach to local-field effects in finite systems: Photoabsorption in the rare gases," Phys. Rev. A, vol. 21, pp. 1561–1572, May 1980.

[64] E. K. U. Gross and W. Kohn, "Local density-functional theory of frequency-dependent linear response," Phys. Rev. Lett., vol. 55, pp. 2850–2852, Dec 1985.

[65] I. Vasiliev, S. Öğüt, and J. R. Chelikowsky, "Ab initio excitation spectra and collective electronic response in atoms and clusters," Phys. Rev. Lett., vol. 82, pp. 1919–1922, Mar 1999.

[66] V. I. Gavrilenko and F. Bechstedt, “Optical functions of semiconductors beyond density-functional theory and random-phase approximation,” Phys. Rev. B, vol. 55, pp. 4343–4352, Feb 1997.

[67] L. A. Constantin and J. M. Pitarke, “Simple dynamic exchange-correlation kernel of a uniform electron gas,” Phys. Rev. B, vol. 75, p. 245127, Jun 2007.

[68] S. Sharma, J. K. Dewhurst, A. Sanna, and E. K. U. Gross, “Bootstrap approximation for the exchange-correlation kernel of time-dependent density-functional theory,” Phys. Rev. Lett., vol. 107, p. 186401, Oct 2011.

[69] Y. Suzuki and K. Watanabe, “Excitons in two-dimensional atomic layer materials from time-dependent density functional theory: mono-layer and bi-layer hexagonal boron nitride and transition-metal dichalcogenides,” Phys. Chem. Chem. Phys., vol. 22, pp. 2908–2916, 2020.

[70] [Online]. Available: https://etsf.polytechnique.fr/exc/Manual/Use_EXC/

[71] [Online]. Available: https://materialsproject.org/materials/mp-19399/

[72] E. Luppi, H. Hübener, M. Bertocchi, E. Degoli, S. Ossicini, and V. Véniard, “Second-harmonic generation spectroscopy from time-dependent density-functional theory,” MRS Proceedings, vol. 1370, pp. mrss11–1370–yy02–08, 2011.

[73] E. Luppi, H. C. Weissker, S. Bottaro, F. Sottile, V. Veniard, L. Reining, and G. Onida, “Accuracy of the pseudopotential approximation in ab initio theoretical spectroscopies,” Phys. Rev. B, vol. 78, p. 245124, Dec 2008.

[74] S. Bergfeld and W. Daum, “Second-harmonic generation in gaas: Experiment versus theoretical predictions of $\chi^{(2)}_{xyz}$,” Phys. Rev. Lett., vol. 90, p. 036801, Jan 2003.

[75] M. S. Hybertsen and S. G. Louie, “Ab initio static dielectric matrices from the density-functional approach. i. formulation and application to semiconductors and insulators,” Phys. Rev. B, vol. 35, pp. 5585–5601, Apr 1987.

[76] E. K. Chang, E. L. Shirley, and Z. H. Levine, “Excitonic effects on optical second-harmonic polarizabilities of semiconductors,” Phys. Rev. B, vol. 65, p. 035205, Dec 2001.

[77] S. Botti, A. Fourreau, F. m. c. Nguyen, Y. O. Renault, F. Sottile, and L. Reining, “Energy dependence of the exchange-correlation kernel of time-dependent density functional theory: A simple model for solids,” Phys. Rev. B, vol. 72, p. 125203, Sep 2005.

[78] M. L. Tiago, S. Ismail-Beigi, and S. G. Louie, “Effect of semicore orbitals on the electronic band gaps of Si, Ge, and GaAs within the GW approximation,” Phys. Rev. B, vol. 69, p. 125212, Mar 2004.

ECOLE
DOCTORALE

Titre : Description théorique des processus non-linéaires dans les matériaux magnétiques

Mots clés : SHG, TDDFT, $\mathrm{Cr_2O_3}$

Résumé : La génération de seconde harmonique (SHG) est un processus au cours duquel deux photons d'énergie sont absorbés par un matériau et un photon d'énergie 2ω est émis. Ce processus est décrit par la susceptibilité macroscopique du second ordre $\chi^{(2)}$. Cette spectroscopie est utilisée pour étudier les propriétés optiques des matériaux et elle révèle des informations inaccessibles aux spectroscopies optiques linéaires. En effet, les règles de sélection dipolaire interdisent la SHG dans les matériaux centrosymétriques et il est possible d'obtenir une caractérisation structurale et électronique de systèmes complexes. L'absence de symétrie d'inversion du temps, due à un ordre magnétique, fait apparaître de nouvelles contributions dans la génération de seconde harmonique. Dans le cas de matériaux antiferromagnétiques, la symétrie magnétique détermine la polarisation du matériau et SHG révèle alors l'arrangement des spins dans le solide.Elle peut ainsi être utilisée pour l'étude de processus ultrarapides dans les matériaux magnétiques, tels que les phénomènes de démagnétisation. Il existe peu de descriptions théoriques ab initio satisfaisantes pour les processus non-linéaires dans les matériaux magnétiques. Ces approches théoriques doivent être capables de traiter sur le même pied les interactions électron-électron, les effets de champs locaux et la distribution en spin des électrons. Le but de ma thèse était de calculer numériquement les réponses optiques, linéaires et du second ordre, pour des matériaux antiferromagnétiques. J'ai calcule ces deux reponses pour un oxide de chrome(Cr$_2$O$_3$) dans le cadre d'un formalisme ab-initio, reposant sur la TDDFT. Dans cette approche, la distribution en spin a été prise en compte explicitement et cette extension a été implémentée dans le code 2light. Je me suis finalement intéressée à différentes structures possibles pour Cr$_2$O$_3$, ne différant entre elles que par la distribution des spins, et j'ai montré que mes résultats permettaient de discriminer de façon caractéristique entre ces structures.

Title : Theoretical description of non-linear processes in magnetic materials.

Keywords : SHG, TDDFT, $\mathrm{Cr_2O_3}$

Abstract : Second harmonic generation (SHG) is a process in which two photons of energy are absorbed by a material and a photon of energy 2ω is emitted. This process is theoretically described by the second order macroscopic susceptibility $\chi^{(2)}$. This spectroscopy is used to study the optical properties of materials and it reveals additional information which cannot be accessed with linear optical spectroscopies. Indeed, as the dipolar selection rules prohibit SHG in centro-symmetric materials, it is possible to obtain a structural and electronic characterization of complex systems. In particular, the absence of time inversion symmetry, due to a magnetic order, reveals new contributions in second harmonic generation. For the specific case of antiferromagnetic materials, magnetic symmetry determines the polarization of the material and SHG then reveals the arrangement of spins in the solid. It was shown that it can be used to study ultrafast processes in magnetic materials, such as demagnetization. There are few satisfactory ab initio theoretical descriptions for nonlinear processes in magnetic materials. These theoretical approaches must be able to treat the electron-electron interactions, the effects of local fields and the spin distribution of the electrons on the same footing. The aim of my thesis was to numerically calculate the optical, linear and second order responses for antiferromagnetic materials. I calculated these two response functions for a chromium oxide (Cr$_2$O$_3$) as part of an ab-initio formalism, based on TDDFT. In this approach, the spin distribution was taken into account explicitly and this extension was implemented in the 2light code. I was finally interested in different possible structures for Cr$_2$O$_3$, differing from each other only in the spin distribution, and I showed that my results can discriminate between these structures.

Institut Polytechnique de Paris
91120 Palaiseau, France